Exploring the magnetism of the $4f$-based intermetallic compounds on geometrically frustrated lattices

by

Jeonghun Lee

M.Sc., Simon Fraser University, 2018
B.A.Sc., University of Waterloo, 2016

Thesis Submitted in Partial Fulfillment of the
Requirements for the Degree of
Doctor of Philosophy

in the
Department of Physics
Faculty of Science

© Jeonghun Lee 2023
SIMON FRASER UNIVERSITY
Summer 2023

Copyright in this work is held by the author. Please ensure that any reproduction
or re-use is done in accordance with the relevant national copyright legislation.

Declaration of Committee

Name:	**Jeonghun Lee**
Degree:	**Doctor of Philosophy**
Thesis title:	**Exploring the magnetism of the $4f$-based intermetallic compounds on geometrically frustrated lattices**
Committee:	**Chair:** Malcolm Kennett Professor, Physics
	Eundeok Mun Supervisor Associate Professor, Physics
	David Broun Committee Member Associate Professor, Physics
	Steve Dodge Committee Member Associate Professor, Physics
	Karen Kavanagh Examiner Professor, Physics
	Stephen Julian External Examiner Professor, Physics

Abstract

Rare-earth-based intermetallic systems display a wide variety of distinct magnetic properties. Besides the well-known ferromagnetic and antiferromagnetic orderings, specific arrangements of magnetic moments in the lattice can exhibit a wide range of complex magnetic behaviours, such as magnetic frustration, low-dimensional antiferromagnetism, quantum spin liquids and so on. These magnetic phenomena are not restricted to a certain class of materials but are commonly linked to a structural motif. It has been shown that the effects of magnetic frustration are often pronounced in materials with high crystal symmetries and are commonly observed in antiferromagnets with certain lattice geometries, such as 2D square lattices, Kagome (corner-sharing triangles) and triangular lattices (edge-sharing triangles) and pyrochlore (corner-sharing tetrahedra) and face-centred cubic (edge-sharing tetrahedra) structures. The systems studied in this thesis include $CeCd_3P_3$ and RV_6Sn_6, which adopt a hexagonal crystal structure with 2D triangular lattices of $4f$ moments possessing trigonal and hexagonal point symmetry, respectively, and RNi_4Cd, where the $4f$ moments form a 3D face-centred cubic lattice. These systems serve as platforms for exploring the magnetic properties of $4f$ moments in different environments, with a particular emphasis on geometrically frustrated lattices. This thesis is based on the characterization of their crystal structures and their thermodynamic and transport properties.

This thesis also addresses the role of carrier density in $4f$ magnetism, which is often overlooked. For indirect Ruderman–Kittel–Kasuya–Yosida (RKKY) exchange interactions, conduction electrons are mediators in metals. In Ce- and Yb-based metallic systems, the interplay between intersite $4f$–$4f$ coupling and onsite Kondo coupling with conduction electrons determines the ground state, as described by Doniach's phase diagram. However, the carrier density, which is determined by the number of conduction electrons and holes, can impact these interactions and potentially influence the established phase diagram. Therefore, it is necessary to study the phase diagram for low-carrier density systems. While numerous examples of metallic systems exist, those with low carriers are scarce. $CeCd_3P_3$ and $Ce_{3+x}Ru_4Sn_{13-x}$ are low-carrier systems, as evident from their large room-temperature-resistivity values (>1 mΩ cm). $CeCd_3P_3$ with negligible hybridization provides an opportunity to study frustrated magnetism on Ce triangular lattices and to investigate RKKY physics in low-carrier density cases. $Ce_{3+x}Ru_4Sn_{13-x}$, with two crystallographic

sites for Ce ions, represents a rare example, where magnetic and electronic properties can be systematically controlled by the occupancy of Ce-ion on the $2a$ site, denoted as x. The electrical resistivity of $Ce_{3+x}Ru_4Sn_{13-x}$ displays a transition from Kondo lattice behaviour to semiconductor-like behaviour with increasing x. Investigating the ground state of $Ce_{3+x}Ru_4Sn_{13-x}$ for various x may elucidate the role of low carriers on the magnetic properties of heavy fermion systems.

Keywords: Rare-earth-based intermetallic compounds, geometrical frustration, low-carrier-density, magnetism, crystalline electric field effect, RKKY, Kondo effect

Dedication

I dedicate this thesis to my family. Without their support and encouragement, I would not have been able to complete this academic milestone. My wife and son have consistently motivated and supported me throughout my journey. I also extend my appreciation to my parents, whose support and belief in me helped me persist in completing this degree.

Acknowledgements

I would like to express my deepest gratitude to my supervisor, Dr. Eundeok Mun, for his guidance and support throughout my PhD program. Without his incredible patience, I would not have been able to surmount the various challenges that I encountered along the way.

Additionally, I would like to extend my sincere appreciation to the members of my supervisory committee, Dr. David Broun and Dr. Steve Dodge, for their invaluable advice and constructive criticism during the annual progress committee meetings.

I would also like to thank my lab colleagues, Dr. Suyoung Kim, Obinna Uzoh, David Evans and Zachary Podrebersek, for their weekly group meetings, which provided a platform for stimulating discussions about our research. Their contributions have enriched my work and broadened my perspectives.

Finally, I am grateful to my family and friends for their support throughout my program. Their love, encouragement and belief in me have been constant sources of motivation and inspiration.

Table of Contents

List of Tables

List of Figures

Chapter 1

Introduction

Rare-earth-based intermetallic systems contain localized $4f$ electron moments. The trivalent state of rare-earth elements makes them chemically similar, which allows one to synthesize a rare-earth series of isostructural compounds to systematically study their physical properties without abruptly changing their crystal structures. In addition, these systems provide an opportunity to study magnetic ordering phenomena, magnetic anisotropy and other properties related to many electron quantum numbers of the spin (S), orbital (L), and total angular momenta (J) of the f shell.

In many Ce- and Yb-based metallic systems, interesting phenomena have been observed when $4f$ electrons are delocalized. In these metallic systems, the onsite Kondo coupling between localized $4f$ moments and conduction electrons competes with the intersite Ruderman–Kittel–Kasuya–Yosida (RKKY) interaction, where the ground states can be qualitatively explained by the relative strength of the two interactions. In a small Kondo coupling J_K or in weak hybridization between $4f$ moments and conduction electrons, the RKKY interaction is dominant and the $4f$ moments form a long-range magnetic order. In a large J_K, strong hybridization results in a paramagnetic heavy fermion state due to the screening of $4f$ moments by conduction electrons. In the intermediate J_K regime, two interactions compete strongly, but they can be easily tuned by external nonthermal control parameters. For example, a continuous suppression of magnetic order toward a quantum critical point can be achieved by pressure, magnetic field and chemical substitution. At the quantum critical point, non-Fermi liquid behaviours resulting from quantum fluctuations have often been observed.

Despite the classical Doniach's picture (see Section 2.10) giving a good general explanation of the observed behaviour of the Kondo lattice system, many heavy fermion materials exhibit ground states that deviate from it. It has been theoretically and experimentally suggested that the strength of quantum fluctuation driven by geometrical frustration or low-carrier density plays an important role in developing unconventional quantum criticality. To elucidate the role of magnetic frustration with specific lattice geometry and low-

carrier density, the discovery of new $4f$ systems is necessary to provide more experimental evidence.

1.1 Search for intermetallic systems with geometrically frustrated lattice

This thesis is a comprehensive exploration of multiple distinct intermetallic systems that aims to expand the general knowledge of rare-earth-based magnetism in various crystal structures and to explore the effects of magnetic frustration in metallic materials. Magnetic frustration emerges from competing magnetic interactions, resulting in suppression of the long-range magnetic order with unusual and interesting ground states, such as non-collinear magnetic structures, unconventional spin density waves or spin glasses. These magnetic states do not belong to specific classes of materials; however, they are generally linked to a certain structural motif. It has been observed that the effects of magnetic frustration are particularly pronounced in insulating antiferromagnets with high crystal symmetries and geometrically frustrated lattices, such as 2D square nets, Kagome (corner-sharing triangles) and triangular (edge-sharing triangles) lattices and pyrochlore (corner-sharing tetrahedra) and face-centred cubic (edge-sharing tetrahedra) structures. To explore the effect of magnetic frustration in conducting materials, families of compounds that contain a variety of multi-electron quantum numbers J, together with geometrically frustrated lattices, were synthesized and investigated with X-ray diffraction and thermodynamic and transport property measurements. This provided more experimental evidence of which unusual thermodynamic and transport behaviours of interest can be observed and potentially linked to frustrated magnetism. Finding examples in which the effect of magnetic frustration coexists with itinerant conduction electrons is challenging but offers the possibility of revealing highly novel electronic states. The materials were chosen based on multiple structure types, with magnetic ions occupying the geometrically frustrated lattice while having various carrier densities. The intermetallic systems investigated in this thesis were examined in their single crystalline forms.

The subsequent sections provide a brief overview of the motivations and research conducted on these intermetallic systems, emphasizing the specific aspects that will be examined.

1.2 $CeCd_3X_3$ (X = P and As)

Single crystals of $CeCd_3X_3$ (X = P and As) were synthesized to investigate the magnetism of Ce-ions on triangular lattices. The $CeCd_3P_3$ compound adopts a hexagonal $ScAl_3C_3$-type structure (space group $P6_3/mmc$), in which the Ce triangular layers are well separated by the Cd and X atoms and form a 2D geometrically frustrated triangular lattice in the *ab*-

plane, with the Ce^{3+} atoms having trigonal-point symmetry. The results of magnetization, electrical and Hall resistivity and specific heat measurements of single-crystal $CeCd_3P_3$ indicate a strongly anisotropic magnetic response in a low-carrier-density environment, an emergent spin-orbit-entangled doublet ground state of Ce at low temperatures and low-temperature antiferromagnetic ordering at $T_N \sim 0.41$ K. However, due to the extremely low-carrier density of this compound, the Kondo effect is absent. Thus, $CeCd_3P_3$ provides an opportunity to study the complex interplay between magnetic frustration on the Ce triangular lattice and RKKY physics in a low-carrier density condition.

Due to the high vapor pressure of P and As, the samples of $CeCd_3X_3$ single crystals were grown by my supervisor. As for my contribution, I performed X-ray diffraction, specific heat, resistivity and magnetization experiments on both $CeCd_3P_3$ and $LaCd_3P_3$, as well as RCd_3As_3 (R = La, Ce). Furthermore, I took responsibility for the manuscript's preparation, including the creation of plots and writing. This work has been published in *Physical Review B* [1, 2].

1.3 $R\mathbf{V_6Sn_6}$

As part of my MSc, I synthesized single crystals of the heavy rare-earth compounds RV_6Sn_6 (R = Gd−Tm), along with the non-magnetic analog R = Y and Lu in 2016. At that time, the literature only reported polycrystalline samples, and there was limited information available regarding the physical properties of these compounds, apart from magnetization measurements on polycrystalline GdV_6Sn_6. Since then, the RT_6X_6 system has gained interest in the condensed matter physics community due to the observation of exotic quantum phenomena in CoSn, $Co_3Sn_2S_2$ and Fe_3Sn_2 associated with topologically nontrivial band structures. Recent angle-resolved photoemission spectroscopy (ARPES) experiments have highlighted the unique characteristics of RT_6X_6, such as flat Dirac cones and saddle points. One of the appealing aspects of RT_6X_6 compounds is the pristine setting they provide for realizing these states, as the Kagome layer formed by the transition metal in RT_6X_6 does not contain any other atoms. The RT_6X_6 compounds crystallize into a hexagonal $HfFe_6Ge_6$-type structure, with hexagonal layers formed by the rare-earth atoms and Kagome layers formed by the vanadium atoms. Growing single crystals of nonmagnetic RV_6Sn_6 compounds, such as R = Y and Lu, offers an opportunity to study magnetism on the Kagome lattice. However, the vanadium ions on the Kagome layers do not possess a magnetic moment, allowing for a focused investigation of the magnetism arising solely from the $4f$ moments on the hexagonal layers. Among these, TbV_6Sn_6 exhibits the strongest magnetic anisotropy due to its crystal structure and the influence of the crystal electric field (CEF) effect on the $4f$ moments. Additionally, the magnetic ordering temperature in these compounds roughly followed the de Gennes factor, suggesting the dominant role of the RKKY exchange interactions between the $4f$ moments. The separation between the rare-earth layers in RV_6Sn_6,

similar to that in hexagonal $R\mathrm{Cd}_3X_3$ (X = P and As) compounds, is significant, resulting in a quasi-2D rare-earth hexagonal lattice. This configuration has attracted considerable interest because theoretical and experimental studies have proposed that RKKY interaction in such structures could potentially host a skyrmion phase in conjunction with geometric frustration.

In this study, I grew single crystals and conducted measurements of powdered X-ray diffraction patterns, specific heat, resistivity and magnetization. This work has been published in *Physical Review Materials* [3].

1.4 $R\mathbf{Ni}_4\mathbf{Cd}$

To explore the magnetic properties of localized $4f$ moments in a face-centred cubic (fcc) lattice, single crystals of $R\mathrm{Ni}_4\mathrm{Cd}$ (R = rare-earth) were synthesized. The magnetic rare-earth ions forms an fcc lattice, which may have resulted in geometrical frustration. This investigation built upon previous work on $\mathrm{YbNi}_4\mathrm{Cd}$ (MSc thesis), which exhibited unconventional quantum criticality near the putative quantum critical point (QCP). The rare-earth series $R\mathrm{Ni}_4\mathrm{Cd}$, particularly $\mathrm{GdNi}_4\mathrm{Cd}$, provides an opportunity to examine the extent of magnetic frustration in this family and possibly shed light on the observed quantum criticality in $\mathrm{YbNi}_4\mathrm{Cd}$. The S-state of Gd^{3+} ions eliminates the influence of CEF effects, making Gd compounds the best choice for studying magnetic interactions between rare-earth moments. Additionally, the isostructural compounds $R\mathrm{Cu}_4\mathrm{In}$ (R = Gd−Tm) displays a signature of magnetic frustration with a frustration parameter $f = |T_N/\theta_p| \sim 10$, which can be tuned by substituting In with Cd. Thus, it is desirable to investigate the parameters and conditions affecting T_N and θ_p to better understand the role of magnetic frustration in the magnetic properties of the RT_4X family (R = Gd−Tm, T = Cu and Ni, X = In, Cd, Ag, Au, Pd, Mg and Cu).

In this study, I synthesized single crystals of $R\mathrm{Ni}_4\mathrm{Cd}$ and conducted measurements of X-ray diffraction patterns, specific heat, resistivity and magnetization. I also took full responsibility for the preparation of the manuscript, including the creation of plots and writing. This work has been submitted to *Physical Review Materials*.

1.5 $\mathbf{Ce}_{3+x}\mathbf{Ru}_4\mathbf{Sn}_{13-x}$

This study explores the ground state of the $\mathrm{Ce}_{3+x}\mathrm{Ru}_4\mathrm{Sn}_{13-x}$ compound. Magnetization, specific heat and resistivity measurements reveal intriguing characteristics: the absence of magnetic ordering, the presence of a broad maximum in specific heat and magnetic susceptibility at low temperatures and Kondo-lattice-like behaviour in resistivity. These observations highlight the intricate interplay between carrier density and the Kondo effect. However, the physical properties derived from the Kondo effect cannot be solely attributed to ordinary Kondo interactions coupled with crystal field effects. Notably, the investigation unravels the

significance of Ce ion occupancy at the 2a site in $Ce_{3+x}Ru_4Sn_{13-x}$, which has two distinct crystallographic sites for Ce ions. While the 2d-site is fully occupied by Ce, the occupancy of Ce at the 2a site varies due to its coexistence with Sn. The control of this occupancy becomes feasible by carefully selecting the initial loading composition.

Furthermore, single crystals of $R_{3+x}Ru_4Ge_{13-x}$ for R = Ce and Yb were synthesized. Investigations of magnetization, specific heat and resistivity measurements for $R_3Ru_4Ge_{13}$ (R = Y, Ce, Gd, Yb, Lu) demonstrate characteristics associated with heavy fermion systems. $Ce_{3+x}Ru_4Ge_{13-x}$ exhibits a stronger Kondo interaction compared to $Yb_{3+x}Ru_4Ge_{13-x}$ due to its mixed valence character. In contrast, $Yb_{3+x}Ru_4Ge_{13-x}$ displays an anomalous magnetic order at low temperatures, as evidenced by a broad peak in specific heat. The previously reported isostructural compound $Yb_3Ir_4Ge_{13}$, classified as a Kondo semimetal, exhibits a broad peak in the specific heat rather than a clear λ-like transition. The fragile magnetism observed in $Yb_3Ir_4Ge_{13}$ was suggested to result from the failure to establish long-range magnetic ordering due to low-carrier density [4]. Therefore, Ce- and Yb-based $R_{3+x}T_4X_{13-x}$ systems serve as examples of novel phenomena resulting from the interplay between Kondo and RKKY interactions under low-carrier density, which is further modulated by the occupancy of Ce at the specific site.

Only $Ce_{3+x}Ru_4Sn_{13-x}$ will be included in this thesis. The synthesis and measurements of $R_{3+x}Ru_4Ge_{13-x}$ have been completed; however, they will not be included in the thesis due to incomplete data analysis. The work of $Ce_{3+x}Ru_4Sn_{13-x}$ has been published in *Physical Review Materials* [5].

1.6 Layout of the thesis

This thesis is structured as follows. Chapter 2 provides a comprehensive discussion on the magnetic properties of rare-earth-based intermetallic compounds. This chapter also discusses the approach to growing single crystals, which serves as the standard procedure for the growth of single crystals investigated in this thesis. The main intermetallic systems studied in this thesis are presented in subsequent chapters. Chapters 3, 4, 5 and 6 each focus on $CeCd_3P_3$, RV_6Sn_6, RNi_4Cd and $Ce_{3+x}Ru_4Sn_{13-x}$, respectively. These chapters comprise an introduction, experimental results and their subsequent discussions. Each chapter concludes with a summary that highlights the key findings. Chapter 7 concludes the thesis by summarizing the main findings and providing an outlook for future research directions. Overall, this thesis presents a comprehensive exploration of different intermetallic systems, providing insights into their magnetic properties and contributing to a broader understanding of 4f systems.

Chapter 2

Theoretical and experimental overview of intermetallic compounds

2.1 Single ion magnetism

While many textbooks have covered the basics of magnetism [6], this section focuses on the essential information necessary to explain the observed magnetic properties of rare-earth-based intermetallic compounds. Magnetism, a quantum mechanical phenomenon, results from the quantization of the spin and orbital motions of electrons in units of $\hbar$. The magnetic properties of an atom or ion are determined by the electronic state of its partially filled shell. The appropriate Hamiltonian for a single ion with a partially filled shell can be expressed as follows [7]:

$$H = \underbrace{\sum_{i=1}\left(\frac{p^2}{2m} + V(r_i)\right)}_{H_0} + \underbrace{\sum_{i<k}\frac{q^2}{r_{ij}}}_{H_{Coulomb}} + \underbrace{\sum_{i}\xi(r)(\mathbf{l}_i \cdot \mathbf{s}_i)}_{H_{SOC}} \tag{2.1}$$

where H_0 is the most dominant term which describes the sum of the kinetic and potential energy of electrons without interactions between the electrons. The states of electrons in the same shell, which have $2(2l+1)$ possibilities, are degenerate. The factor 2 outside the bracket accounts for the spin degrees of freedom. The remaining $H_{Coulomb}$ and H_{SOC} terms are treated as perturbations to H_0. With the Coulomb interaction, the $2(2l+1)$ degeneracy is lifted. Because of the large electrostatic electron-electron repulsion, the lowest energy configuration of the electrons in the shell is achieved by distributing electrons among $2l+1$ possible orbitals in such a way that the occupation of two electrons in the same orbital is least favored. Since H_0 is independent of total orbital angular momentum L ($\sum_i l_i$) and total spin angular momentum S ($\sum_i s_i$), which commute with H_0, L and S as well as J are good quantum numbers. The spin-orbit interaction couples total orbital angular momentum with total spin angular momentum, i.e. $J = L \pm S$, also known as Russell–Saunders (LS) coupling

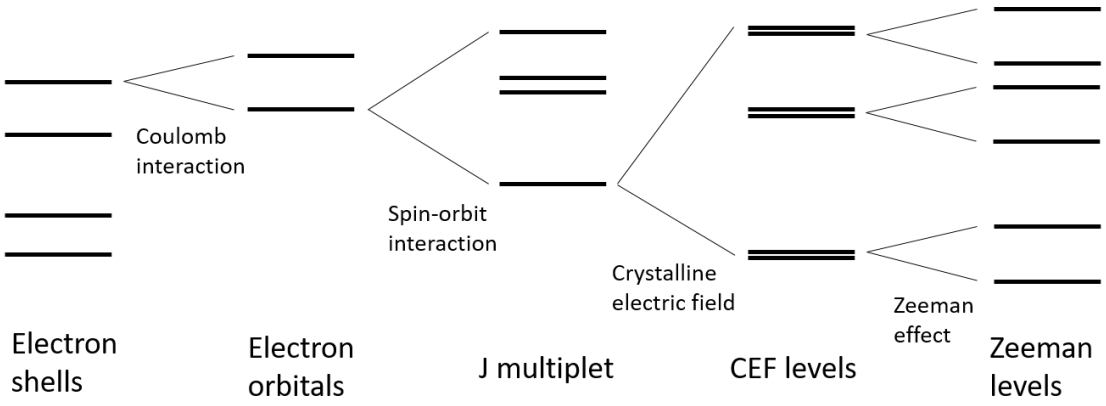

Figure 2.1: Overview of the energy splitting scheme for $4f$ ions in a crystalline solid.

scheme. For lighter atoms, where Coulomb interaction dominates over spin-orbit interaction, the Russell-Saunders coupling scheme is appropriate. However, for heavier atoms where the strength of spin-orbit interaction increases with atomic number as $H_{SOC} \propto Z^2$, the j-j coupling scheme should be used when $H_{Coulomb} \ll H_{SOC}$. In the j-j coupling scheme, the total angular momentum of each electron in the unfilled shell is determined to a first approximation by $j_i = l_i \pm s_i$ [7].

2.2 Single ion in a crystalline solid

In real materials, magnetism arises from the collective contributions of magnetic ions within a solid. For crystalline materials, the constituent atoms form a periodic lattice that produces periodic electrostatic charge distributions. If one of the constituent atoms is magnetic, the magnetic ion experiences anisotropic electrostatic fields produced by neighboring ions, known as the crystalline electric field (CEF) which will be discussed in Section 2.5. In this environment, the degeneracy of the single J multiplet described in Section 2.1 is further lifted. The relative energy scale between spin-orbit coupling and CEF depends on the source of magnetism (e.g. $3d$ vs. $4f$), and determines the order in which the splitting occurs. If the source of magnetism is $3d$, spin-orbit coupling is generally much weaker than CEF ($H_{SOC} \ll H_{CEF}$), and the strong CEF quenches the orbital moment ($L = 0$). In this case, the CEF splitting precedes the SOC splitting. If the source of magnetism is $4f$, the energy scale of CEF is much weaker than spin-orbit coupling ($H_{CEF} \ll H_{SOC}$), and the Hund's rule ground state is applicable, with $4f$ magnetism well-explained by the total angular momentum J. An external magnetic field within the solid further lifts the degeneracy, known as Zeeman splitting. Figure 2.1 provides an overview of the energy splitting scheme for typical $4f$ ions in a crystalline solid.

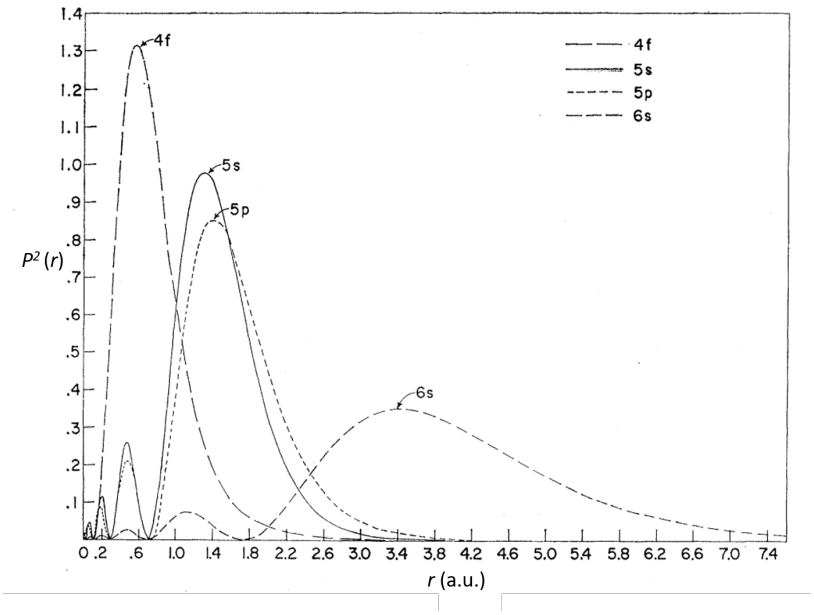

Figure 2.2: Radial wavefunctions of various shells for Gd^{3+} [8].

2.3 $4f$ moment

The rare-earth elements comprise 15 lanthanides ranging from lanthanum ($4f^0$) to lutetium ($4f^{14}$), along with scandium and yttrium. Scandium and yttrium have an empty $4f$ shell, which makes them non-magnetic. In lanthanide elements, the observed local moment character arises from the well-preserved $4f$ shells that are shielded by the outer completely filled $5s^2$ and $5p^6$ shells. The atomic configuration of lanthanides is $[Xe]4f^n6s^2$, except for lanthanum, cerium, gadolinium, and lutetium, which have $[Xe]4f^n5d^16s^2$. In the ionic state, the two $6s$ electrons and one electron from the $4f$ shell are lost, leading to the trivalent state R^{3+}. As a result, $4f$ electrons do not participate in chemical bonding and are weakly affected by the surrounding environment. Freeman and Watson [8] performed Hartree-Fock calculations to determine the square of the radial wavefunctions of various shells for Gd^{3+}, as shown in Figure 2.2. The positions of the $4f$ electrons are likely to be closer to the atom's core than those of the 5s, 5p, and 6s electrons. Therefore, the $4f$ electrons are localized on the atom in intermetallic compounds, and the $4f$ wavefunction does not overlap with another $4f$ wavefunction of a nearest-neighbor atom. Consequently, the $4f$ system can be regarded as a model system that describes localized $4f$-moments fixed at the lattice points.

To determine the moment of $4f$-electrons, it is commonly assumed that the quantum numbers describing $4f$-electrons are derived from the LS-coupling scheme. This assumption is valid since the gap between the LS-multiplets is large enough that the total orbital angular momentum L and the total spin angular momentum S remain good quantum numbers. The values of L and S can be obtained from the ground state electronic configuration

of $4f$-electrons, and the rules for finding L and S are given by the sum of the orbital quantum numbers l_i and spin quantum numbers s_i, respectively. Additionally, the total angular momentum J, due to strong spin orbit coupling, is given by Hund's rule as follows:

- Combination electrons that has maximum spin multiplicity ($2S$+1) has the lowest energy
- Out of all possible maximum $2S$+1, one that has maximum L has lowest energy
- $J = |L - S|$ for less than half-filled shell and $J = L + S$ for more than half-filled shell

The magnetic properties arising from the rare-earth elements are governed by the Hund's rule ground state. The magnetic moment due to the orbital angular momentum and the spin angular momentum are given by

$$L = \mu_B L = \mu_B \sqrt{L(L+1)}, \tag{2.2}$$

$$S = g_s \mu_B S = 2\mu_B \sqrt{S(S+1)}, \tag{2.3}$$

where μ_B is the Bohr magneton. The magnetic moment due to both L and S is

$$\mathbf{J} = \mathbf{L} + \mathbf{S} = \mu_B(\mathbf{L} + \mathbf{S}) \tag{2.4}$$

According to Wigner Eckhardt theorem, the total moment due to total angular momentum is given by

$$\boldsymbol{\mu} = -g_J \mu_B \mathbf{J}, \tag{2.5}$$

where g_J is the Landé g-factor which accounts for the different weight of the spin and the orbital contributions to the total angular momentum. The Landé g-factor is given by

$$g_J = 1 + \frac{J(J+1) + S(S+1) - L(L+1)}{2J(J+1)} \tag{2.6}$$

The summary of associated quantum numbers for $4f$-electrons and Landé g-factors is tabulated in Tab. 2.1.

2.4 Curie-Weiss law

According to the classical theory of paramagnetism, magnetic moments are treated as individual magnetic dipoles that do not interact with one another.

$$H = \sum_{j=1}^{N} (H_0^{(j)} + H_{SO}^{(j)} - \mathbf{m}_j \cdot \mathbf{B}_0) \tag{2.7}$$

$H_0^{(j)}$ represents the total background energy arising from the Coulomb interaction between electrons and the nucleus on the jth ion. $H_{SO}^{(j)}$ accounts for the spin-orbit coupling effect on

Table 2.1: A summary of associated quantum numbers for $4f$-electrons and Landé g-factors in lanthanide series.

$4f$ e^-	$[R^{3+}]$	S	L	J	g_J
0	La	0	0	0	–
1	Ce	1/2	3	5/2	6/7
2	Pr	1	5	4	4/5
3	Nd	3/2	6	9/2	8/11
4	Pm	2	6	4	3/5
5	Sm	5/2	5	5/2	2/7
6	Eu	3	3	0	–
7	Gd	7/2	0	7/2	2
8	Tb	3	3	6	3/2
9	Dy	5/2	5	15/2	4/3
10	Ho	2	6	8	5/4
11	Er	3/2	6	15/2	6/5
12	Tm	1	5	6	7/6
13	Yb	1/2	3	7/2	8/7
14	Lu	0	0	0	–

the jth ion. Finally, the Zeeman energy term is added. The balance between the strengths of the spin-orbit coupling and the Zeeman interactions determines the magnetization. The magnetization is defined as

$$\mathbf{M} = n\mathbf{<m>}, \tag{2.8}$$

where n is N/V and the brackets $<\cdots>$ is the quantum statistical average. The magnetization induced in a paramagnet by a magnetic field $\mathbf{B}_0$ applied along the z-direction is

$$M = n\frac{1}{Z_1}Tr(me^{\beta H_1}) = nk_BT\frac{\partial}{\partial B_0}\ln Z_1, \tag{2.9}$$

where Z_1 is the single-particle partition function. The factors that affect the magnetization are thermal energy k_BT, spin-orbit interaction, and magnetic field.

The partition function Z_1 can only be determined in the limiting cases since J is no longer a useful quantum number when the magnetic field is present.

In the strong spin-orbit coupling limit, which is applicable in magnetic, rare-earth-based, intermetallic compounds, it it generally assumed that only the ground state of the (LS)-multiplets is occupied and J can become a useful quantum number.

The relevant energy is then

$$E_{\gamma LSJM_j} = E^{(0)}_{\gamma LSJ} + g_J M_J \mu_B B_0. \tag{2.10}$$

From this we can obtain the partition function

$$Z_1 = e^{-\beta E^{(0)}_{\gamma LSJ}} \frac{\sinh\left(\beta g_J \mu_B B_0 (J + \frac{1}{2})\right)}{\sinh(\frac{1}{2}\beta g_J \mu B_0)}. \tag{2.11}$$

Using Eq. 2.9, the magnetization can obtained as

$$M = M_0 B_J(\beta g_J J \mu_B B_0), \tag{2.12}$$

where M_0 is the saturation magnetization, $M_0 = nJg_J\mu_B$, B_J is the Brillouin function, which is defined as

$$B_J(x) = \frac{2J+1}{2J}\coth\left(\frac{2J+1}{2J}x\right) - \frac{1}{2J}\coth\left(\frac{x}{2J}\right). \tag{2.13}$$

The magnetic susceptibility is obtained by

$$\chi = \mu_0 \left(\frac{\partial M}{\partial B_0}\right)_T. \tag{2.14}$$

In the high-temperature limit ($\beta\mu_B B_0 \ll 1$), the Brillouin function reduced to

$$B_J \approx \frac{J+1}{3J}x + O(x^3), \tag{2.15}$$

which leads to the Curie's law

$$\chi = \frac{C}{T} = \frac{N_A p_{eff}^2 \mu_0 \mu_B^2}{3k_B T}, \tag{2.16}$$

where C is the Curie constant. p_{eff} is the effective magneton number and can be defined as

$$p_{eff} = g_J\sqrt{J(J+1)}. \tag{2.17}$$

Curie's law does not take into account interactions between magnetic moments, while the Curie-Weiss law extends it by incorporating the effect of the Weiss molecular field, denoted by λ. At high temperatures, the thermal energy dominates over the exchange interaction between magnetic moments. As temperature decreases, the exchange interaction grows stronger, causing the magnetic moments to align spontaneously. The energy at which spontaneous magnetization occurs is proportional to the internal magnetic field, known as the Weiss molecular field or exchange field H_{ex}, which is related to the magnetization produced by local electron spins.

The exchange interaction between the electron spins lies on the realm of quantum mechanics. The exchange interaction energy is

$$E_{ex} = 2\tilde{J}\sum_{i<j}\mathbf{S}_i \cdot \mathbf{S}_j, \tag{2.18}$$

where the sum is over nearest spins. $\tilde{J}$ is the exchange field, which is taken as a mean field, is produced by the exchange interactions with the nearest spins. The exchange field at i-th spin is

$$H_{ex}(i) = -\frac{2\tilde{J}_z}{g\mu_B} < \mathbf{S} > . \tag{2.19}$$

The magnetization is given by

$$M = N_A g\mu_B < \mathbf{S} > . \tag{2.20}$$

Then the effective field becomes

$$H = H_0 + H_{ex} = H_0 + \lambda M, \tag{2.21}$$

where H_0 is the external field. The Curie's law now becomes

$$\chi = \frac{M}{(H_0 + \lambda M)} = \frac{C}{T}. \tag{2.22}$$

After rearranging, the Curie-Weiss law can be obtained:

$$\chi = \frac{C}{T - C\lambda} = \frac{C}{T - \theta_{CW}}, \tag{2.23}$$

where θ_{CW} is the paramagnetic Curie-Weiss temperature, given by

$$\theta_{CW} = C\lambda = \frac{N_A g^2 \mu^2 S(S+1)}{3k_B}\frac{2z\tilde{J}}{g^2\mu_B^2 N_A} = \frac{2z\tilde{J}}{3k_B}S(S+1). \tag{2.24}$$

The magnitude of θ_{CW} indicates the strength of the molecular field, which also measures the strength of exchange interactions between the spins. If $\theta_{CW} > 0$ ($\tilde{J} > 0$), ferromagnetic exchange interactions are dominant. If $\theta_{CW} < 0$ ($\tilde{J} < 0$), antiferromagnetic exchange interactions are dominant.

2.5 Crystalline electric field

Rare-earth intermetallic compounds exhibit very large magnetic anisotropy that arise mostly from the crystalline electric field (CEF). When moment-bearing ions occupy a crystallo-

graphic site, the surrounding atoms produce electric fields due to their charge distributions. This CEF splits the degeneracy of Hund's rule ground state multiplet.

In the point charge model, the surrounding atoms are treated as point charges located at $\vec{R}$. If the rare-earth ion's position is at the origin, the potential at a point $\vec{r}$ can be obtained by summing the potentials from the surrounding point charges as follows [9]:

$$V(\vec{r}) = \frac{1}{4\pi\epsilon_0} \sum_l \frac{q_i}{|\vec{r} - \vec{R}_i|}, \tag{2.25}$$

which satisfies Laplace equation, $\nabla^2 V = 0$. Expanding the potential V_{CEF} as the product of a radial component and spherical harmonics is a convenient approach because it makes it easier to find the matrix element. Specifically, the potential can be expressed in terms of spherical harmonics or tesseral harmonics, which can then be used to obtain the matrix element. The expansion takes the form:

$$V(r, \theta, \phi) = \sum_i \sum_{m=-l}^{l} A_l^m r^l Y_l^m(\theta, \phi), \tag{2.26}$$

where

$$A_l^m = (-1)^m \frac{4\pi}{2l+1} \sum_j \frac{q_j}{R^{l+1}} Y_l^{-m}(\Theta, \Phi) \tag{2.27}$$

Then, the CEF hamiltonian is

$$H_{CEF} = -|q| \sum_i V_i(\vec{r}) \tag{2.28}$$

A common method to determine the energy levels and eigenfunctions of ions in a crystalline electric field is to diagonalize the CEF matrix. One approach to calculating the matrix elements involves expressing Equation 2.28 using Stevens operators, which involve J_z or $J_\pm$. The CEF Hamiltonian becomes

$$H_{CEF} = \sum_n \sum_m B_n^m O_n^m, \tag{2.29}$$

where the Stevens operators O_n^m are functions of the total angular momentum J, while the CEF parameters B_n^m include θ_l term and determine the energy levels of the CEF states. θ_l can be denoted as Stevens factors α_j, β_j, and γ_j for l =2, 4, and 6, respectively. Stevens factors depend on the form of the electronic charge cloud. Values of Stevens factors for rare-earth ions can be found other textbook [10].

The Hamiltonian given in Eq. 2.29 is dependent on the symmetry of the central atom, and therefore limits the number of non-zero CEF parameters. It is important to determine the crystallographic site occupied by rare-earth ions, as this will help simplify the CEF Hamiltonian. In cases where rare-earth ions occupy a crystallographic site with cubic point

symmetry, the CEF Hamiltonian can be reduced to

$$H_{CEF}^{cubic} = B_4^0(O_4^0 + 5O_4^4) + B_6^0(O_6^0 - 21O_6^6) \tag{2.30}$$

For Ce^{3+}, Stevens factor γ_j becomes zero, which further reduces the Hamiltonian with only B_4^0 parameter. The CEF of cubic symmetry lifts the Hund's rule ground state multiplet $J = 5/2$ into a doublet Γ_7 and a quartet Γ_8-quartet as follows

$$\begin{aligned} |\Gamma_7\rangle &= a\,|\pm 5/2\rangle - b\,|\mp 3/2\rangle \\ |\Gamma_8\rangle &= \begin{cases} |\pm 1/2\rangle \\ b\,|\pm 5/2\rangle + a\,|\mp 3/2\rangle \end{cases} \end{aligned} \tag{2.31}$$

For the cubic point symmetry, the value of B_4^0 is given by $B_4^0 = \Delta/360$, where Δ is the energy gap between Γ_7 and Γ_8. To determine the ground state and energy gap, experiments such as neutron scattering, magnetic susceptibility, and specific heat measurements are necessary.

The CEF levels have a significant impact on the physical properties of these compounds, and temperature-dependent magnetic susceptibility, magnetization, and magnetic specific heat can be calculated when a magnetic field is applied along $\alpha = x, y, z$ as follows:

$$\chi_{\alpha\alpha}(T) = N_A(g_J\mu_B)^2 \left[\sum_n \beta \frac{e^{-\beta E_n}}{Z} \langle\lambda_n|\, J_\alpha\, |\lambda_n\rangle^2 + \sum_n \sum_m \frac{1}{\Delta E} \frac{e^{-\beta E_m} - e^{-\beta E_n}}{Z} \langle\lambda_m|\, J_\alpha\, |\lambda_n\rangle^2 \right] \tag{2.32}$$

$$M_\alpha(T) = g_J\mu_B \sum_n \frac{e^{-\beta E_n}}{Z} \langle\lambda_n|\, J_\alpha\, |\lambda_n\rangle \tag{2.33}$$

$$C(T) = k_B \sum_n \frac{-\beta E_n}{Z} \left(\frac{E_n}{k_B T}\right)^2 - k_B \sum_n \left(\frac{e^{-\beta E_n}}{Z} \frac{E_n}{k_B T}\right)^2 \tag{2.34}$$

When rare-earth ions occupy a crystallographic site with hexagonal or tetragonal point symmetry, a strong magnetic anisotropy exists between the basal plane and the c axis. Magnetic susceptibility with the field applied along different crystallographic directions gives rise to anisotropy, except for Gd due to its S-state ($L = 0$). The paramagnetic Curie-Weiss temperature θ_α, obtained from the magnetic susceptibility of a single crystal with a field applied along the α-direction, can be expressed as follows [11]:

$$k_B\theta_\alpha = \frac{\sum_n \langle\Gamma_n| \left[J_\alpha^2 - \frac{J(J+1)}{3} H_{CEF}\, |\Gamma_n\rangle\right]}{\sum_n \langle\Gamma_n|\, J_\alpha^2\, |\Gamma_n\rangle} \tag{2.35}$$

Using Eq. 2.35, the paramagnetic Curie-Weiss temperatures for different field directions can be expressed in terms of B_2^0 and B_2^2 as follows:

$$\begin{aligned} k_B\theta_x &= \tfrac{1}{10}(B_2^0 - B_2^2)(2J-1)(2J+3) \\ k_B\theta_y &= \tfrac{1}{10}(B_2^0 + B_2^2)(2J-1)(2J+3) \\ k_B\theta_z &= -\tfrac{1}{5}B_2^0(2J-1)(2J+3). \end{aligned} \tag{2.36}$$

The magnetic susceptibility in the basal plane is assumed to be isotropic for rare-earth ions occupying a crystallographic site with hexagonal or tetragonal point symmetry. In these point symmetry, $B_2^2 = 0$ and the second order CEF parameter B_2^0 can be obtained by the difference between $k_B\theta_x$ and $k_B\theta_z$ as follows:

$$k_B(\theta_x - \theta_z) = \frac{3}{10}B_2^0(2J-1)(2J+3). \tag{2.37}$$

The second order CEF parameter B_2^0 can be expressed as $B_2^0 = \alpha_J <r^2> A_2^0$, where α_J denotes the multiplicative Stevens factor which is a rare-earth-dependent and $<r^2>$ represents the mean square of the $4f$ electron radius, in the point charge model. A_2^0 is a coefficient in the expansion of the solution of Laplace's equation in spherical harmonics for the electrostatic potential at the rare earth site due to the CEF. All A_2^0 values are negative throughout the rare-earth series. The sign of B_2^0 is determined by α_J. Since $<r^2>$ is always positive, the sign of B_2^0 is solely determined by α_J. If B_2^0 is the predominant term, then a negative B_2^0 value would favor the alignment of magnetic moments in the basal plane, while a positive B_2^0 value would prefer the alignment of magnetic moments along the c axis. The sign of α_J are positive for Sm^{3+}, Er^{3+}, Tm^{3+}, and $Yb3^{3+}$. For heavy rare-earth intermetallic compounds with rare-earth occupying non-cubic point symmetry site, the change in easy-magnetization from Ho to Er observed in experiment is the result of this CEF effects on rare-earth ions.

2.6 RKKY interaction

The small overlap between $4f$ orbitals on neighboring rare-earth ions due to the much smaller mean radius of the $4f$ shell compared to the interionic spacing makes direct exchange coupling between $4f$-moments difficult. However, in metals, despite similar interionic spacing to that of insulators, magnetic couplings between ions are two orders of magnitude stronger, allowing for magnetic order up to 300 K. This is due to the indirect exchange interaction, mediated by conduction electrons. Ruderman and Kittel independently developed the theory to describe this indirect exchange coupling between the nuclear spin and conduction electron spin via the hyperfine interaction in 1954 [12]. This theory was later applied to localized $4f$-moments by Kasuya [13] and Yosida [14], and the name RKKY was coined after these four scientists.

The exchange interaction, J_{sf}, between the localized spin $\boldsymbol{S}_i$ at $\boldsymbol{R}$ and a conduction electron spin $\boldsymbol{s}_i$ at $\boldsymbol{r}$ is treated as a perturbation and can be written as

$$H_{sf} = -J(\mathbf{r}-\mathbf{R})\sum_{i=1}^{2}\mathbf{s}_i\cdot\mathbf{S}_i \tag{2.38}$$

where $J(\boldsymbol{r}-\boldsymbol{R})$ is approximated with the constant $J_0\delta(\mathbf{r}-\mathbf{R})$ in the RKKY interaction. It is important to note that the exchange interaction, also known as s-f interaction, between a $4f$ electron and a conduction electron is determined by the interband exchange interaction $J(\mathbf{k},\mathbf{k}^{'})$ in momentum space. The interband mixing results in an antiparallel alignment between the spin of the $4f$ electron and that of the conduction electron, particularly for ions with more than half-filled $4f$ shells (R = Gd - Yb). This interband mixing is highly dependent on the direction of the conduction electron momentum, and thus, results in anisotropies in the RKKY conduction spin-density distribution [15, 16]. However, in the RKKY theory, the exchange integral is assumed to be isotropic, meaning that the indirect exchange is unchanged with respect to a uniform rotation of the angular momenta, and a function of $\mathbf{k}-\mathbf{k}^{'}=q$ only. In this theory, $J(q)$ is considered to be a constant J_0 [17], albeit with crude approximations.

A single ionic spin S on the electrons gas leads to the spin polarization of the conduction electrons. Since H_{sf} is spin dependent, conduction electrons of different spin respond differently. The wavefunctions in the the first order perturbation theory are

$$\psi_{\pm}^{(1)}(\mathbf{r},\mathbf{k}) = \psi_{\pm}^{(1)}(\mathbf{r},\mathbf{k}) + \sum_{\mathbf{k}^{'},s}\psi_s(\mathbf{r},\mathbf{k}^{'})\frac{\langle\psi_s(\mathbf{r},\mathbf{k}^{'})|\,H_{sf}\,|\psi_{\pm}(\mathbf{r},\mathbf{k})\rangle}{E(\mathbf{k})-E(\mathbf{k}^{'})}, \tag{2.39}$$

where $s=\pm$ refers to the spin, and E($\mathbf{k}$) is the unperturbed energy of an electron in state $\mathbf{k}$. The densities of electron with + and - spins are the sums of $|\psi_{\pm}^{(1)}(\mathbf{r},\mathbf{k})|^2$ over all filled states. The spin polarization can be defined as

$$P(r) = \sum_{\mathbf{k}} f(\mathbf{k})\{|\psi_{+}^{(1)}(\mathbf{r},\mathbf{k})|^2 - \psi_{-}^{(1)}(\mathbf{r},\mathbf{k})|^2\}, \tag{2.40}$$

where $f(\mathbf{k})$ is the occupation number for states $\mathbf{k}$. Using the free electron model, Eqs. 2.39 and 2.40 give the spin polarization as

$$P(r) = \sum_{\mathbf{q}} J(\mathbf{q})\sum_{\mathbf{k}}\left\{\frac{f(\mathbf{k})-f(\mathbf{k}+\mathbf{q})}{E(\mathbf{k})-E(\mathbf{k}+\mathbf{q})}\right\}e^{i\mathbf{q}\cdot\mathbf{r}} \tag{2.41}$$

$$= \sum_{\mathbf{q}} J(\mathbf{q})\chi(\mathbf{q})e^{i\mathbf{q}\cdot\mathbf{r}}, \tag{2.42}$$

where $\chi(\mathbf{q})$ is the susceptibility function. By changing the summation to integration, $\mathbf{q}$-dependent susceptibility becomes

$$\chi(\mathbf{q}) = \frac{mk_F}{4\pi^2\hbar^2}\left(1 + \frac{4k_f^2 - q^2}{4k_F}\ln\frac{q+2k_F}{q-2k_F}\right). \tag{2.43}$$

The real space susceptibility can be obtained by Fourier transform and is given by

$$\chi(\mathbf{r}) = \frac{1}{(2\pi)^3}\int d^3\mathbf{q}\chi(\mathbf{q})e^{i\mathbf{q}\cdot\mathbf{r}} \tag{2.44}$$

$$= \frac{9\pi Z^2}{2V^2E_F}F(2k_Fr), \tag{2.45}$$

where Z is the number of conduction electrons per atom, V is the atomic volume, and

$$F(x) = \frac{\sin x - x\cos x}{x^4}. \tag{2.46}$$

The Ruderman-Kittel function form, denoted by $F(x)$, is responsible for the oscillatory nature of the RKKY interaction. This long-range interaction is a consequence of the sharply defined Fermi surface resulting from the Fermi-Dirac distribution function $f(\mathbf{k})$, which contains a large portion of parallel surfaces separated by $2k_F$. The period of oscillation in real space is $2\pi/2k_F$, and $F(x)$ decays as $\cos(2k_Fr)/r^3$. This oscillatory behavior is similar to Friedel oscillations, which occur when the electron gas responds to a delta-function charge and results in oscillations in electron charge density.

The polarization produced by a spin at R_i will interact with another spin at R_j through H_{fs}. The second order perturbation theory, the effective interaction between the two spins is

$$H_{ij} = -\sum_{\mathbf{k},\mathbf{k}'} |\langle\mathbf{k}'|H_{fs}|\mathbf{k}\rangle|^2\left\{\frac{f(\mathbf{k}) - f(\mathbf{k}+\mathbf{q})}{E(\mathbf{k}) - E(\mathbf{k}+\mathbf{q})}\right\}, \tag{2.47}$$

where $f(\mathbf{k})$ is the Fermi-Dirac distribution function which is to restrict intermediate state to $|\mathbf{k}'| > k_F$ and occupied states to $|\mathbf{k}| \leq k_F$. Substituting Eq. 2.38 leads to an effective Hamiltonian of the Heisenberg type between two localized spins as follows

$$H_{ij} = -J(\mathbf{R}_i - \mathbf{R}_j)\mathbf{S}_i \cdot \mathbf{S}_j, \tag{2.48}$$

where

$$J(\mathbf{R}_i - \mathbf{R}_j) = \sum_{\mathbf{q}} J^2(\mathbf{q})\chi(\mathbf{q})e^{i\mathbf{q}\cdot(\mathbf{R}_i - \mathbf{R}_j)} \tag{2.49}$$

In the RKKY approximation, $J(\mathbf{q}) = J_0$ and using Eq. 2.43

$$J(\mathbf{R}_i - \mathbf{R}_j) = \frac{9\pi Z^2 J_0^2}{2V^2E_F}F(2k_F|\mathbf{R}_i - \mathbf{R}_j|) \tag{2.50}$$

since

$$k_F = (3\pi^2N)^{1/3}; E_F = \frac{\hbar^2}{2m}(3\pi^2N)^{2/3} \tag{2.51}$$

2.7 de Gennes scaling

Within the mean field theory, $C\lambda$ in Eq. 2.23 is the paramagnetic Curie-Weiss temperature θ_p and λ is proportional to the exchange interaction. Thus, θ_p can be expressed as follows:

$$k_B\theta_p = \frac{-3\pi z^2 m j_{sf}^2}{4\hbar k_F^2} S(S+1) \sum_i F(2k_F R_i) \tag{2.52}$$

Typically, the magnetic moments of rare-earth ions are described by the quantum number J. It would be convenient to express $\mathbf{S}$ in terms of $\mathbf{J}$ in Eq. 2.38, i.e. $\mathbf{S} = (g_J - 1)\mathbf{J}$. Since the mean field demands θ_p equal to ordering temperature T_M, this leads to

$$k_B T_M = k_B\theta_p = \frac{-3\pi z^2 m j_{sf}^2}{4\hbar k_F^2} (g_J - 1)^2 J(J+1) \sum_i F(2k_F R_i), \tag{2.53}$$

where $(g_J - 1)^2 J(J+1)$ is known as de Gennes factor. It is expected that T_M and θ_p scales linearly with the de Gennes factor if rare-earth provides the same number of electron to the conduction band [18]. The de Gennes factor is highest for Gd. Hence, Gd typically exhibits the highest ordering temperature in the isostructural series. Note that it is sometimes observed that the magnetic ordering temperature of Tb is higher than that of Gd. This can be attributed to the significant magnetic anisotropy of Tb ions caused by crystal electric field (CEF) effects.

2.8 Kondo effect

The typical temperature-dependent behavior of a metal's resistivity is determined by the scattering mechanisms of conduction electrons, such as electron-phonon and electron-electron interactions, which weaken as temperature decreases. However, in metals with dilute magnetic impurities, a rise in resistivity as temperature decreases has been observed. This was first noted by Jun Kondo in 1964 [19], who identified the single-ion Kondo effect as the cause of the $-\log(T)$ dependence in resistivity. Kondo employed second-order perturbation theory to describe the antiferromagnetic coupling between the spin of the conduction electron $\mathbf{s}$ and the spin of the localized moment $\mathbf{S}$ in the Hamiltonian. It should be noted that Kondo's perturbation theory is valid only above the characteristic energy scale of the Kondo interaction [20], $k_B T_K$, which is given by

$$k_B T_K = D e^{-1/2JN(E_F)}, \tag{2.54}$$

where D is the conduction electron bandwidth and $N(E_F)$ is the density of states at the Fermi level. For $T \ll T_K$, in a strong coupling limit, subsequent non-perturbative approaches such as Anderson's *poor man scaling* [21] and Wilson's renormalization group [22] have

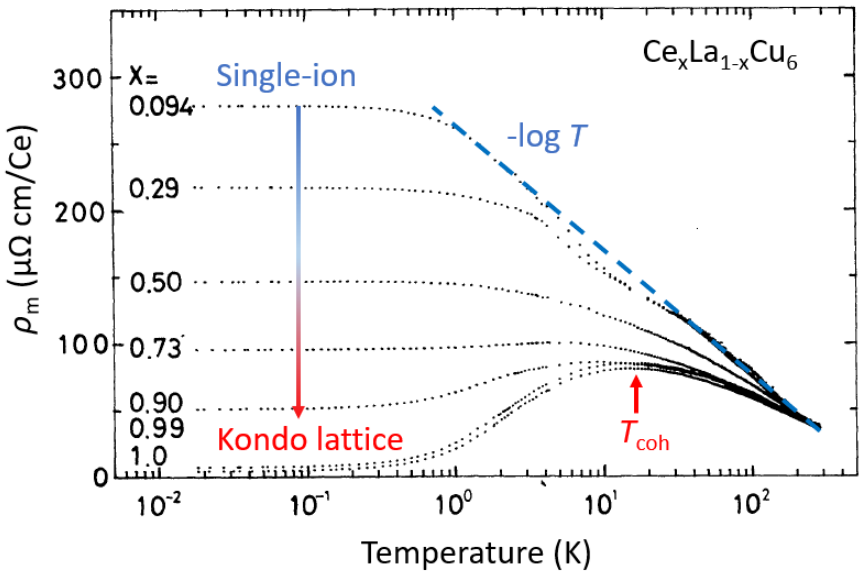

Figure 2.3: Temperature-dependent magnetic resistivity of $Ce_xLa_{1-x}Cu_6$ showing the evolution from single-ion regime to Kondo lattice regime by increasing Ce substitution. Figure is modified from [23].

revealed that a cloud of conduction electrons scatters off a magnetic impurity and screens it completely as $T \to 0$, forming the many-body nonmagnetic singlet.

2.9 Kondo lattice

The preceding section discussed the single-ion Kondo effect, in which isolated magnetic impurities are dispersed randomly throughout a metallic host and exhibit Kondo scattering incoherently at high temperatures [24]. However, when these magnetic impurities are arranged periodically, a phenomenon known as the dense Kondo lattice occurs. In this case, many individual single-ion Kondo effects behave collectively, resulting in a coherent state at low temperatures. The Hamiltonian that describes the Kondo lattice model is as follows:

$$H = \sum_{\mathbf{k},\sigma} \epsilon(\mathbf{k}) c^{\dagger}_{\mathbf{k}} c_{\mathbf{k},\sigma} + J_K \sum_i \mathbf{S}_i \cdot \mathbf{s}_i, \tag{2.55}$$

where J_K is the antifferomagnetic coupling between the spin of the local moment and the spin of the conduction electrons. Upon decreasing temperature, the Kondo coherence leads to the development of a broad maximum in resistivity with negative logarithmic temperature dependence, as observed in the single-ion Kondo effect. This evolution from the single-ion Kondo effect to Kondo coherence can be observed in the compound $Ce_xLa_{1-x}Cu_6$, as illustrated in Fig. 2.3. At low concentrations of Ce ($x = 0.094$), magnetic Ce ions act as independent scattering centers, resulting in a random distribution within the crystallographic

site. However, as the Ce concentration increases, the periodicity of Ce increases, leading to coherent scattering and a return to normal metallic behavior. The reduced spin disorder scattering, imposed by translational symmetry, occurs at a characteristic energy scale known as the coherence temperature (T_{coh}), which is indicated at the resistivity maximum. In the Kondo lattice regime (also known as the heavy fermion regime), the conduction electrons strongly hybridize with the $4f$ electrons below T_{coh}, and the coherence state recovers Fermi liquid regime, resulting in $\rho(T) \propto T^2$.

The crystalline electric field effect described in section 2.5 and the Kondo effect described in section 2.9 are typically discussed separately. However, in real materials, both effects are present and interact with each other, resulting in a combined effect that cannot be explained by simply adding the two contributions. In some Ce- and Yb-based Kondo lattice systems, the Kondo effect acts on one of the CEF splitting levels depending on the relative energy strengths of the CEF energy gap and the characteristic Kondo temperature. The resulting magnetic specific heat, resistivity, magnetic susceptibility as a function of temperature has been calculated in Refs. [25, 26, 27].

2.10 Doniach phase diagram

The competition between inter-site RKKY interaction and on-site Kondo interactions determines the ground state of a Ce- or Yb-based intermetallic compound [28]. As explained in Sections 2.6 and 2.8, the energy scales associated with these interactions are $T_{RKKY} = J_K^2 N(E_F)$ and $T_K = De^{-1/2J_K N(E_F)}$, where J_K is the exchange interaction between the $4f$ electron and conduction electrons, and $N(E_F)$ is the electronic density of states at the Fermi level. Figure 2.4 depicts the classical Doniach phase diagram illustrating the competition between RKKY and Kondo interactions, where the relative strength of these interactions can be adjusted by a single parameter $J_K N(E_F)$. The strength of J_K is determined by the hybridization potential V_{sf} and the position of the $4f$ level E_{4f} with respect to the Fermi level E_F. In the Hubbard model, the intra-site Coulomb repulsion energy U for the two electrons with opposite spin is much greater than $E_F - E_{4f}$. J_K can be given by

$$J_K \approx \frac{V_{sf}^2}{E_F - E_{4f}}. \tag{2.56}$$

Rare-earth-based intermetallic compounds typically have $4f$ levels that lie deep inside the Fermi level. As a result, the difference between E_F and E_{4f} is large, which leads to a small J_K. In this regime, the magnetically ordered state is favored. However, the strength of $J_K N(E_F)$ can be adjusted through chemical doping, pressure, or magnetic field, allowing for the suppression of magnetic order as $J_K N(E_F)$ increases and T_{RKKY} becomes comparable to T_K. In the regime $T_K \sim T_{RKKY}$, many exotic phenomena driven by quantum fluctuation have been observed. In the large $J_K N(E_F)$ limit, all local moments are fully screened and

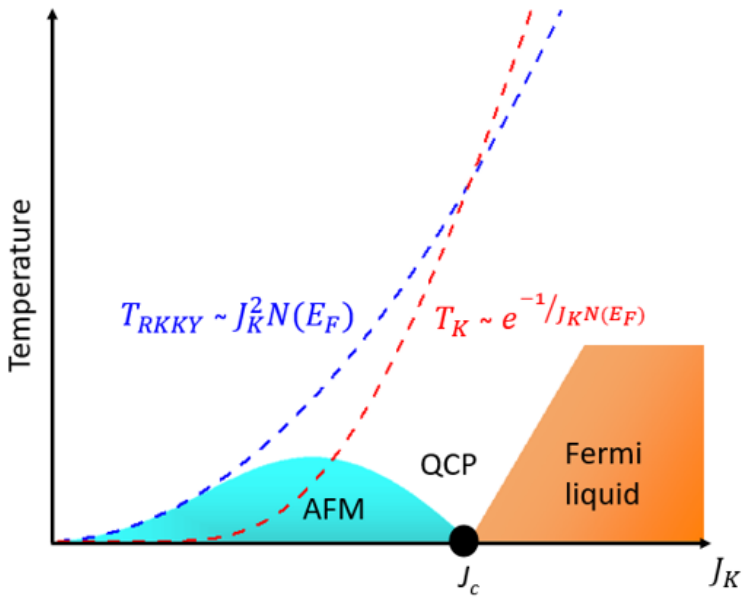

Figure 2.4: Doniach phase diagram.

behave like a paramagnet, entering a paramagnetic heavy fermion regime. In this regime, the Fermi liquid state ($\rho \propto T^2$) is typically recovered.

2.11 Geometrical frustration

Typically, geometrical frustration refers to a phenomenon observed in antiferromagnets on a two-dimensional (2D) triangular lattice of Ising spins, where it becomes impossible to align all spins antiparallel simultaneously [29]. In general, spins minimize their energy by ordering, such as parallel alignment for ferromagnets and antiparallel alignment for antiferromagnets. However, in triangular lattices with antiferromagnetic exchange interaction, not all spins can be ordered simultaneously, leading to a large number of degenerate ground states [30]. This phenomenon, arising solely from geometric constraints, is known as geometrical frustration. Triangle or tetrahedron motifs, as shown in Fig. 2.5, can be used to construct 2D and 3D frustrated lattices such as Kagome (corner-sharing triangles) and triangular lattices (edge-sharing triangles), and pyrochlore (corner-sharing tetrahedra) and face-centred cubic (edge-sharing tetrahedra). The degree of geometrical frustration in a material can be quantified by the frustration parameter, which is defined as:

$$f = \frac{|\theta_{CW}|}{T_N}, \tag{2.57}$$

where materials with $f > 10$ are considered to be strongly frustrated [30]. The magnetic behavior of a material is strongly influenced by its crystal structure, which determines the

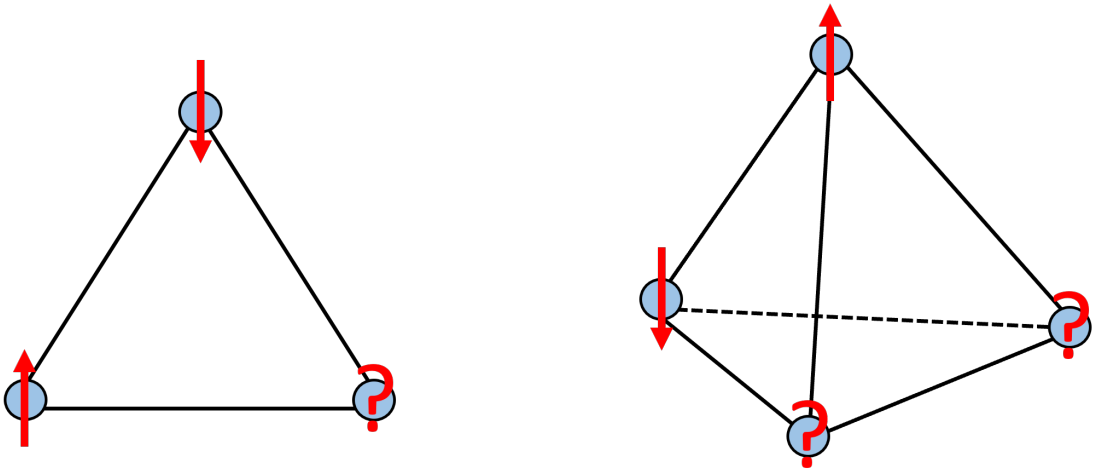

Figure 2.5: Triangular and tetrahedron unit.

arrangement of localized moments. Thus, understanding the crystal structure is crucial for explaining the observed magnetic properties.

Strongly geometrically frustrated systems provide a platform for studying novel phenomena, such as highly correlated fluctuating spin liquid state QSL [31, 32]. Several candidate materials have been proposed for hosting various types of QSL depending on the models used to describe them. The most notable candidates are 2D organic salts κ-(BEDT-TTF)$_2$Cu$_2$(CN)$_3$ [33], Herbertsmithite ZnCu$_3$(OH)$_6$Cl$_2$ [34], α-RuCl$_3$ [35], and YbMgGaO$_4$ [36]. $4f$-based frustrated systems, which exhibit strong spin-orbit coupling, have also demonstrated novel phenomena arising from anisotropic exchange interactions, such as the realization of spin ice in pyrochlore R_2Ti$_2$O$_7$ (R = Dy and Ho) [37] and complex spin texture, such as skyrmion in Gd$_2$PdSi$_3$ [38].

Unlike geometrically frustrated insulating magnets, where only short-range interactions dominate via superexchange or dipolar exchange interactions, the presence of the conduction electrons in $4f$-based metallic systems fosters RKKY exchange interactions, which stabilize long-range ordering even in a frustrated lattice. In *fcc* RCu$_4X$ (R = Gd - Tm and X = In, Cd) [39], it has been shown that the degree of magnetic frustration can be modified by the electrical conductivity, altering the coupling strength between the moments by changing the effective number of conduction electrons participating in the RKKY interactions. This change in relative coupling strengths (e.g., superexchange vs. RKKY) between the moments has resulted in various magnetic structures [40, 41, 42].

Moreover, when $4f$-electrons undergo Kondo effect in a frustrated lattice, the combination of quantum fluctuations induced by geometrical frustration and the Kondo screening leads to novel types of quantum phase transitions with various novel phases such as metallic

spin liquid, which is distinctive from the spin liquid described above, and Kondo-destructed antiferromagnetic and paramagnetic phases with different Fermi surface volumes [43, 44]. Doniach phase diagram only considers the Kondo coupling J_K as the parameter controlling the relative strength between RKKY and Kondo interactions. However, theoretical studies and experimental evidence suggest that an additional parameter, Q, which represents the strength of quantum fluctuations or zero-point motion induced by geometrical frustration or competing interactions, is necessary to explain non-Fermi liquid behavior and antiferromagnetic phases with small and large Fermi surfaces in heavy fermion systems [45, 46, 47, 48].

The compounds YbPtBi [49], YbAgGe [50], and $Pr_2Ir_2O_7$ [51] have been reported to exhibit non-Fermi-liquid behaviors due to geometrical frustration. However, it is worth noting that similar quantum critical phases have also been observed in Ge-substituted $YbRh_2Si_2$ [52] and $YbAlB_4$ [53], which are not geometrically frustrated. Therefore, it is important to investigate whether frustration-like behavior in these compounds arises from non-frustrated lattices or if additional parameters other than Q are necessary to fully understand the global phase diagram.

2.12 Kondo Lattice in dilute carrier limit

The presence of a sufficient number of conduction electrons is necessary for the formation of either a magnetically ordered state between local $4f$-moments via RKKY interactions or a Fermi liquid state by strong hybridization between $4f$-electron and conduction electrons via Kondo interactions. However, heavy fermion systems with an insufficient number of conduction electrons have recently garnered interest due to their exotic behaviors. Kondo screening via singlet formation requires at least one conduction electron per localized f electron. When the total number of localized $4f$-electrons exceeds the total available conduction electrons for screening, full screening cannot be achieved, resulting in protracted Kondo screening. This phenomenon was first predicted theoretically in the periodic Anderson model [54] and subsequently observed experimentally in YbX_4In (X = Ag, Cd, In, Mg, Tl, Zn) [55], low-carrier system $CeNi_{2-\delta}As_2$ [56], and in $CeNi_{2-\delta}(As_{1-x}P_x)_2$ [57]. The full Kondo screening, which promotes $4f$-electron spin to the Fermi sea and increases the Fermi surface volume, cannot be achieved within a low conduction electron background, resulting in a small Fermi surface. In conventional Doniach's phase diagram, the competing interaction can be varied by the Kondo coupling J_K or density of state at the Fermi level $N(E_F)$. Due to the easy tunability of Kondo coupling with non-thermal controls, heavy fermion systems that have been studied for quantum criticality are mostly metals that assume there are sufficient numbers of conduction electrons. However, heavy fermion systems with low-carrier-density are lacking, and it is desirable to search for such systems to understand the role of carrier concentration on competing interactions and quantum criticality.

In Kondo lattice systems, the low number of conduction electrons can lead to gap formation, as demonstrated by the prototypical Kondo insulator SmB_6, where the transition from metallic to insulating behavior in resistivity is observed with decreasing temperature due to the opening of a gap induced by the hybridization of $4f$-electrons with conduction electrons via strong spin-orbit coupling [58, 59]. This is a consequence of the periodic Anderson Kondo lattice model in the half-filled case, where one local moment and one conduction electron per unit cell contribute to the conduction electron band, causing the chemical potential to fall in the gap and leading to the insulating behavior. The importance and tunability of spin-orbit coupling in Kondo insulators has been demonstrated in $Ce_3Bi_4Pt_3$, where the transition from Kondo insulator to semimetal can be observed by decreasing the strength of spin-orbit coupling as Pt is replaced by Pd [60]. The inclusion of spin-orbit coupling of $5d$-conduction electrons in Kondo lattice systems and reducing the number of conduction electrons give rise to various phases such as topological Kondo insulators [61], Dirac-Kondo semimetals [62], and Weyl-Kondo semimetals [63], which compete with conventional Kondo-coherent and magnetic states and introduce a new regime in the heavy fermion phase diagram [64, 62].

2.13 Single crystal growth by flux method

In research, high quality samples are essential in all aspects of materials science, especially condensed matter physics. The absence of impurities and defects associated with grain boundaries can provide unique mechanical, optical, electrical, and magnetic properties that can be anisotropic. Polycrystalline samples consist of small single crystals with randomly oriented grains separated by grain boundaries, where the random crystal orientation averages out any anisotropic properties. Consequently, crucial information on magnetic and electronic anisotropies is absent from bulk physical property measurements of polycrystalline samples. Therefore, high quality single crystals are necessary to study directional dependence of various physical properties.

In this thesis, although there are several techniques available for growing single crystals, all samples are grown by the flux method which involves growing single crystals from high temperature solutions [65]. In this method, all the constituents dissolve into the flux at sufficiently high temperatures, where common flux elements include Al, Bi, Ga, In, Pb, and Sn, owing to their low melting temperatures. Compared to other single crystal growth methods such as Czochralski and zone refining, the flux method has several advantages. One of the main advantages is that it allows for growing single crystals within the temperature range of a typical bench-top furnace by utilizing the eutectic regime in the phase diagram. The Czochralski and zone melting methods are typically limited to compounds that melt congruently, whereas the flux method is suitable for both incongruently melting and peritectically decomposing materials. When the growth conditions for the flux method are determined, multiple parameters are required to be considered, such as the purity and

melting temperature of constituent elements and temperature profiles. Binary phase diagram often helps to determine the ratio among constituents and maximum and decanting temperature.

Understanding the binary phase diagram is essential to grow single crystals of a target compound. In the following, the basic elements of the binary phase diagram is explained, which is a vital information for growing ternary compounds studied in this thesis. As an example, the Gd-Cd phase diagram is shown in Fig.2.6. There are six thermodynamically stable binary compounds indicated by vertical lines: GdCd, α- and β-$GdCd_2$, $GdCd_3$, $Gd_{11}Cd_{45}$, $Gd_{13}Cd_{58}$, and $GdCd_6$. The liquidus line separates the liquid region and the regions containing liquid and solid. An incongruently melting compound decomposes into another solid and liquid phase before melting completely. Except GdCd compound, all binary compounds in the Gd-Cd phase diagram melt congruently (peritectic decomposition). $GdCd_6$, for example, is stable up to 716 °C and decomposes into $Gd_{13}Cd_{58}$ and liquid above 716 °C, known as the peritectic reaction. GdCd melts congruently at 1170 °C, meaning that it melts completely into liquid above 1170 °C with the same composition as the solid.

This binary phase diagram can be utilized to grow single crystals by the flux method, typically preparing the initial mixture with the desired composition. For example, if the target compound is $GdCd_6$, one can use the composition indicated by a red circle in Fig.2.6(a). The mixture with 92 % Cd and 8 % Gd is heated to the temperature corresponding to the horizontal position of the red circle (800 °C), and then slowly cooled down to 400 °C which is sufficiently above the melting temperature of Cd (∼324 °C). When the mixture reaches the liquidus line, $GdCd_6$ starts to form, following the red line along the liquidus line. At 400 °C, the solid phase $GdCd_6$ can be separated from the liquid phase by a centrifuge. The cooling rate and initial stoichiometry can be adjusted to obtain a larger size and better quality of the sample that is likely to yield by a longer cooling time. However, it is not always the case.

To grow a ternary compound, the similar procedure for growing a binary compound can be followed. However, since ternary phase diagrams are not widely available, binary phase diagrams of the constituent elements are relied upon to prevent the formation of unwanted binary phases. The goal is to choose an initial mixture composition with sufficient amounts of flux and without any binary liquidus lines at the working temperatures of the constituent elements. Note that to avoid reactions with the crucible, the concentration of rare earth elements should be less than 12% as a rule of thumb.

In Fig.2.7(a), a ternary plot of Gd-Ni-Cd displays known binary (gray circle) and ternary intermetallic compounds (stars). Binary compounds located on the edges of the ternary plot can be grown using binary phase diagrams, shown in Fig.2.6 b) and c). Since the ternary phase diagram are unknown, the liquidus surface for a target phase has to be guessed from the Gd-Cd, Gd-Ni, and Cd-Ni binary phase diagrams. For instance, to grow $GdNi_4Cd$ (target phase), the initial mixture composition is chosen as 1:4:25 = Gd:Ni:Cd, as indicated by the

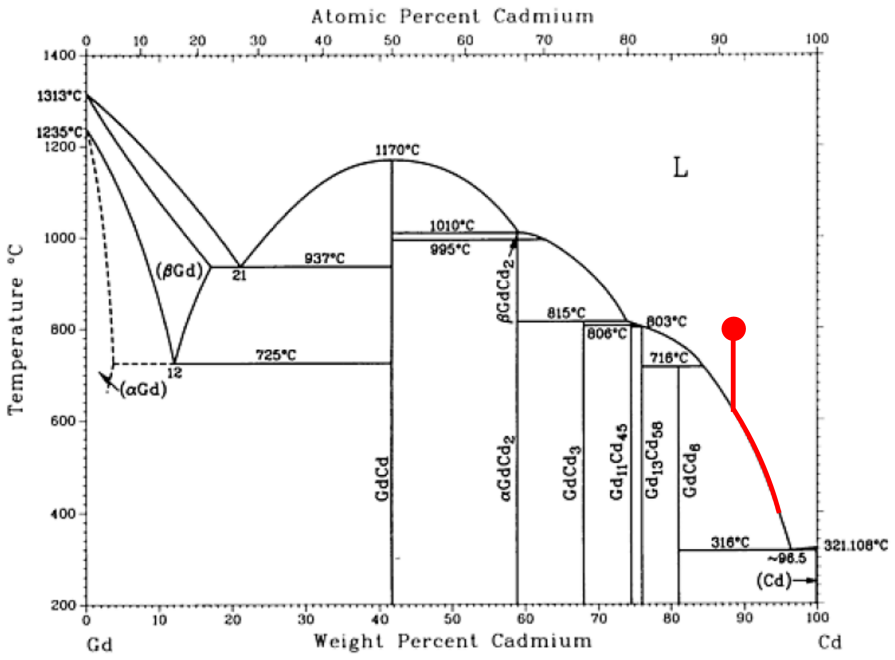

Figure 2.6: Binary phase diagram for Gd-Cd.

blue circle. At this composition, Gd and Ni will dissolve into Cd melt above 700°C. Based on the Gd-Cd and Ni-Cd phase diagrams, there are no liquidus lines for binary compounds above 700°C, providing an opportunity to grow $GdNi_4Cd$, if it exists, above 700 °C. Also, when cooled just above 700°C, touching liquidus surfaces for other ternary phases indicated by black stars should be minimized to maximize the yield of the target phase.

The techniques of growing a ternary single crystal described above are used for all single crystals studied in this thesis. Details of single crystal growth, used in this thesis, are described in each corresponding chapter.

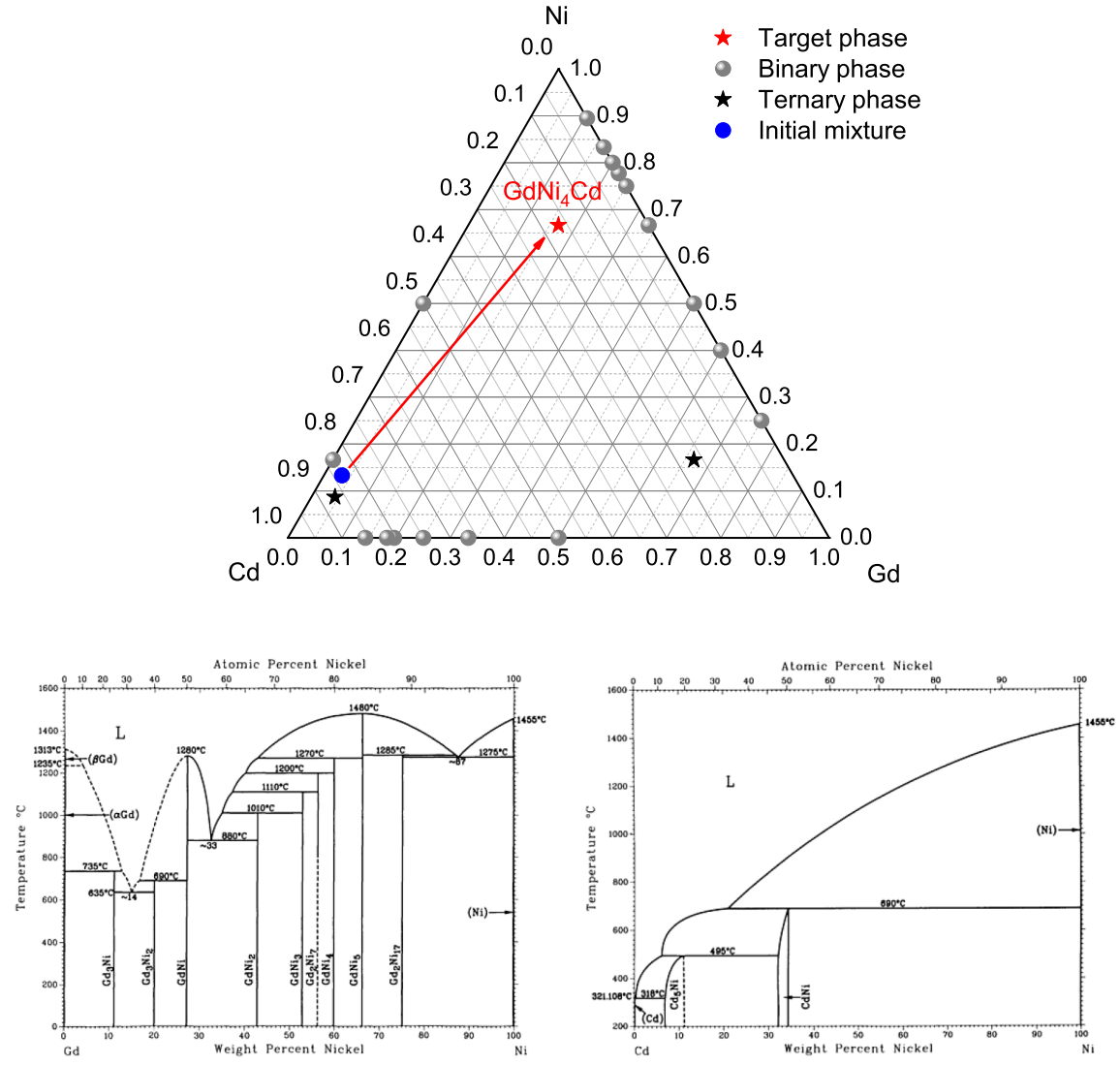

Figure 2.7: Phase diagrams. a) Ternary phase diagram for Gd-Ni-Cd. b) Binary phase diagram for Gd-Ni and Cd-Ni

Chapter 3

The 2D metallic triangular lattice antiferromagnet $CeCd_3P_3$

3.1 Abstract

Single crystals of RCd_3P_3 (R = La and Ce) have been investigated by magnetization, electrical resistivity, Hall coefficient, and specific heat. Magnetization measurements of $CeCd_3P_3$ demonstrate clear quasi-2D magnetic behavior. Electrical resistivity and Hall coefficient measurements suggest that RCd_3P_3 compounds are low carrier-density metallic systems, in strong contrast to an earlier study of polycrystalline material. Specific heat and electrical resistivity measurements of $CeCd_3P_3$ reveal a high temperature (structural) phase transition at T_s = 127 K and antiferromagnetic ordering below T_N = 0.41 K. Upon applying magnetic field in the easy-plane ($H \| ab$) the magnetic ordering temperature increases to 0.43 K at $H \sim 15$ kOe, demonstrating partial lifting of the magnetic frustration. The large electronic specific heat persists in an unusually wide range of temperature above T_N, due to the frustrated spins. The observation of conventional metallic behavior in the electrical resistivity suggests that the f-electrons in $CeCd_3P_3$ undergo negligible hybridization with the conduction electrons. Thus, $CeCd_3P_3$ may be a model system for exploring the complex interplay between magnetic frustration and RKKY physics on a low carrier-density Ce triangular lattice.

3.2 Introduction

The ground states of geometrically frustrated insulating magnets exhibit a range of unconventional order parameters [30, 66, 67]. In low dimensional quantum magnets, competing magnetic exchange interactions give rise to strong frustration accompanied by enhanced quantum fluctuations. For such systems, frustration may prevent the magnet from forming long range order, leading to magnetically liquid states [31, 68, 69, 70]. These "spin liquids" come in different forms, depending on the type of magnetic exchange interaction (*e.g.*, Heisenberg, Dzyaloshinskii-Moriya, or Kitaev) and the lattice geometry (*e.g.*, square,

triangular, Kagome, honeycomb, or pyrochlore) [66, 31, 69]. In particular, spins on two-dimensional (2D) triangular lattices, interacting antiferromagnetically via XY or Heisenberg exchange, provide an excellent opportunity to study various ground states, and have strong potential for realizing the spin-liquid state in 2D [29, 71, 72, 73, 74, 75, 76, 77, 78]. Until now, most such spin systems have been insulating. Finding examples in which the spin-liquid state coexists with itinerant conduction electrons remains challenging, but offers the possibility of revealing highly novel electronic states.

For triangular lattice (TL) magnets with $4f$-electrons, spin-orbit entanglement strongly enhances quantum fluctuations and promotes a liquid ground state characterized by highly anisotropic interactions between moments [79, 80, 81, 82, 83, 84, 85]. In the absence of spin-orbit coupling, it has been shown that the frustration is partially lifted by forming a planar 120^o spin structure with strong magnetic anisotropy [86, 87, 88, 89, 90]. Examples of f-electron materials with 2D TL structures include spin-gapped $YbAl_3C_3$ [91, 92, 93, 94], spin-liquid systems $YbMgGaO_4$ [95, 96, 97, 98, 36] and $NaYbS_2$ [99, 100], and easy-plane antiferromagnets $CeCd_3P_3$ and $CeCd_3As_3$ [101, 102]. Recently, a putative quantum spin-liquid state in which magnetic order remains absent and magnetic excitations persist down to low temperatures has been claimed for $4f$-electron insulating TL magnets such as $YbMgGaO_4$ [97] and $NaYbS_2$ [99], where an effective $J_{\rm eff} = 1/2$ spin moment can be realized due to strong spin-orbital coupling in conjunction with the crystalline electric field (CEF) effect. For metallic materials, containing Ce and Yb elements, the physical properties are associated with the competition between Kondo hybridization and RKKY interactions [28, 103]. However, rich behavior can also be driven by magnetic frustration, which promotes complex ordering and might even lead to a quantum spin liquid state under some circumstances [48, 104, 105, 106, 107, 49, 50, 108]. Clearly, then, it is desirable to uncover new f-electron metals satisfying the conditions for magnetic frustration.

In this report, we present physical properties of single crystals of RCd_3P_3 (R = La and Ce). At room temperature, RCd_3P_3 materials adopt the hexagonal $ScAl_3C_3$-type structure (space group $P6_3/mmc$), in which the Ce triangular layers are well separated by the Cd and P atoms and form a 2D, geometrically frustrated TL in the ab-plane, with the Ce^{3+} atoms having trigonal point symmetry [101, 109, 110, 111]. The results of magnetization, electrical and Hall resistivity, and specific heat measurements of single crystal $CeCd_3P_3$ indicate strongly anisotropic quasi-2D magnetism associated with low carrier-density metallic behavior; an emergent spin-orbit-entangled doublet ground state of Ce at low temperatures; a high temperature (structural) phase transition at $T_s = 127$ K; and low temperature antiferromagnetic ordering at $T_N = 0.41$ K. Previously, polycrystalline $CeCd_3P_3$ was reported to be a semiconductor with a band gap of ∼0.75 eV, with measurements of magnetic susceptibility revealing no magnetic ordering down to 0.48 K [101]. Similarly, the isostructural system $CeZn_3P_3$ was reported as showing semiconducting behavior with a relatively small band gap [112, 113, 114].

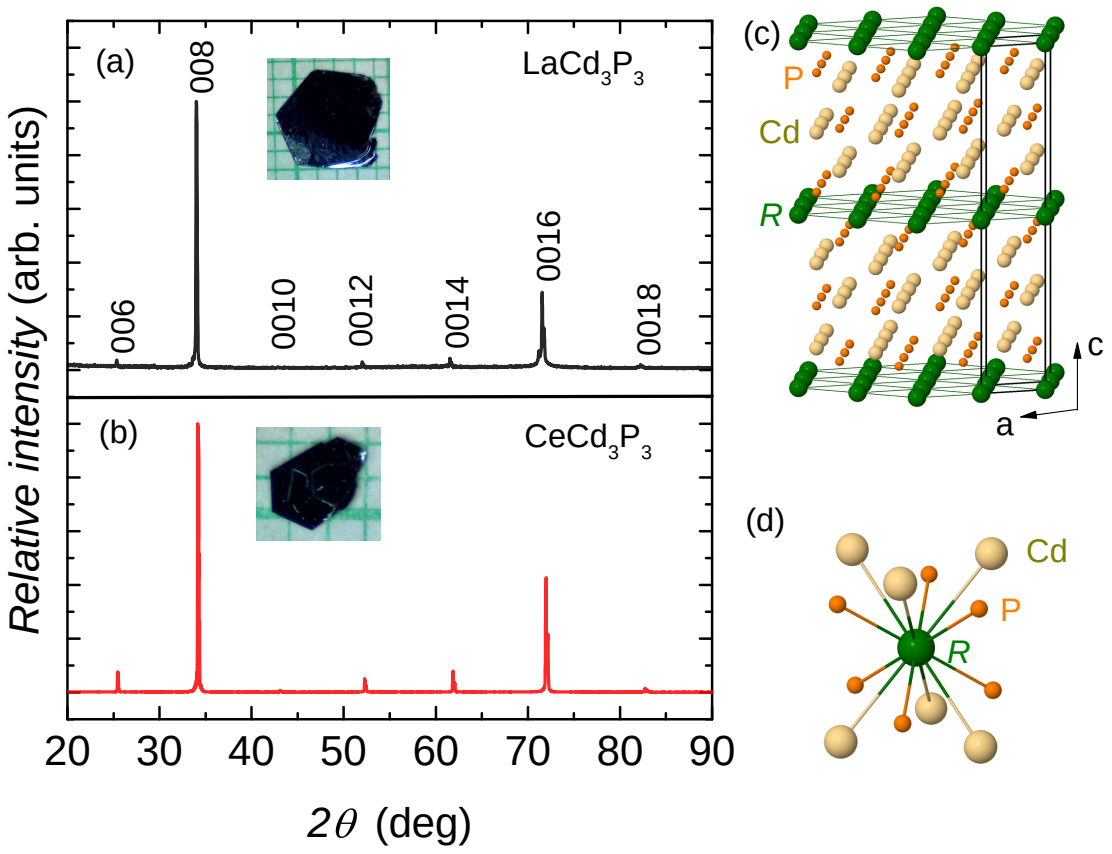

Figure 3.1: (a) (b) Single crystal X-ray patterns for RCd$_3$P$_3$ (R = La and Ce). Insets show photographs of LaCd$_3$P$_3$ and CeCd$_3$P$_3$ single crystals on a 1 mm grid scale. (c) Crystal structure of RCd$_3$P$_3$. (d) Local coordination environments of R-site.

3.3 Experiments

Single crystals of RCd$_3$P$_3$ (R = La and Ce) were prepared by high temperature ternary melt [65]. The as-grown single crystals have hexagonal morphology and form very thin ab-plane platelets, reflecting their layered structure, as shown in Fig. 3.1. The samples have been characterized using powder X-ray diffraction (XRD) in a Rigaku MiniFlex instrument at room temperature. The XRD pattern contains no indications of impurity phases. Analysis of the powder XRD patterns shows that samples crystallize in the hexagonal ScAl$_3$C$_3$-type structure ($P6_3/$mmc, 194) with lattice parameters a = 4.2767 Å and c = 20.9665 Å for CeCd$_3$P$_3$ and a = 4.2925 Å and c = 21.0763 Å for LaCd$_3$P$_3$, consistent with earlier work [101]. As seen in the platelet XRD results in Fig. 3.1, only (0, 0, ℓ) reflection peaks are detected, indicating that the crystallographic c-axis is perpendicular to the planes.

Magnetization was measured as a function of temperature, from 1.8 to 300 K, and magnetic field, up to 70 kOe, using a Quantum Design (QD) Magnetic Property Measurement System (MPMS). Four-probe ac resistivity measurements were performed in a QD Physi-

cal Property Measurement System (PPMS). Hall resistivity measurements were performed in a four-wire geometry, for which the magnetic field directions were reversed to remove magnetoresistance effects due to voltage-contact misalignment. Specific heat was measured by the relaxation method down to $T = 0.37$ K in a QD PPMS. For the dc transport measurements, samples were prepared by attaching Pt wires using silver paste. Due to the high contact resistance, of the order of 50 Ω at room temperature, we were not able to measure dc resistivity at low temperatures. Thus, microwave surface resistance measurements were performed below 5 K, at a frequency of 202 MHz.

3.4 Results

Figure 3.2(a) shows the temperature dependence of magnetic susceptibility, $\chi(T) = M/H$, of $LaCd_3P_3$. $\chi(T)$ displays temperature independent, diamagnetic behavior down to roughly 100 K. As temperature decreases $\chi(T)$ increases slightly below 100 K, most likely due to the presence of paramagnetic impurities, consistent with the magnetic field dependence of magnetization at $T = 1.8$ K shown in Fig. 3.2(b).

Figure 3.2(c) shows the temperature dependence of the electrical resistivity, $\rho(T)$, of $LaCd_3P_3$. The $\rho(T)$ curve exhibits typical metallic behavior below 400 K, except for a distinct feature near $T_s = 172.5$ K. The phase transition temperature T_s is determined from analysis of $d\rho/dT$ and indicated by the arrow in Fig. 3.2(d). However, $\chi(T)$ shows no sign of a phase transition near T_s. It is notable that the resistivity at 300 K is much larger than that of typical metals, suggesting low carrier concentration in this system. The effect of a magnetic field on the phase transition is shown in Fig. 3.2(d), where the application of 90 kOe along the c direction shifts the transition upwards by less than 1 K. It should be noted that in earlier work on polycrystalline $LaCd_3P_3$, $\rho(T)$ exhibited semiconducting behavior and showed no sign of a phase transition near T_s [101].

The temperature dependence of the specific heat, $C_p(T)$, of $LaCd_3P_3$ is shown in Fig. 3.2(e). $C_p(T)$ reveals a clear signature of the phase transition, with a λ-like anomaly at $T_s = 173$ K (see inset), consistent with the electrical resistivity. No thermal hysteresis is observed at T_s, as seen in the inset of Fig. 3.2(e). Because the specific heat curve does not follow $C_p(T) = \gamma T + \beta T^3$ at low temperatures, as shown in Fig. 3.2(f), neither γ nor Debye temperature Θ_D can be accurately obtained. Thus, the value of γ is estimated by a linear extrapolation to zero temperature of the $C_p(T)/T$ curve below 2.1 K. Within error, the estimated γ is consistent with zero, reflecting either a small electronic enhancement or a low carrier-density. Note that the $C_p(T)/T$ value at 1.8 K is ~ 2.5 mJ/mole K^2.

The inverse magnetic susceptibility, $1/\chi(T)$, of $CeCd_3P_3$ is displayed in Fig. 3.3(a), for $H\|ab$ and $H\|c$, together with the polycrystalline average, defined by $\chi_{\text{poly}} = \frac{2}{3}\chi_{ab} + \frac{1}{3}\chi_c$. Remarkably, χ_{ab} is much larger than χ_c, reflecting two dimensional magnetic behavior most likely due to the presence of strong CEF effects. At high temperatures, the susceptibility

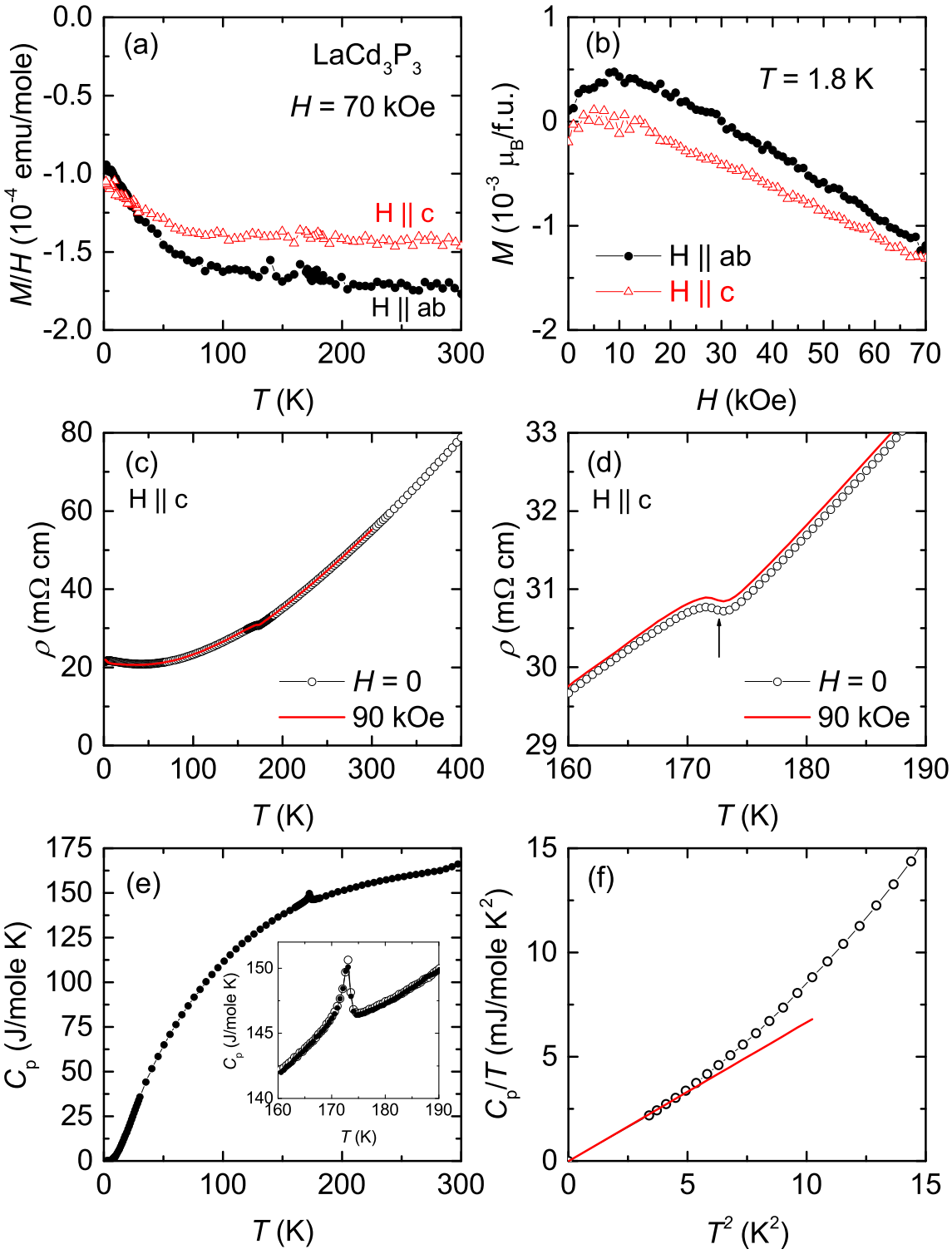

Figure 3.2: Physical properties of $LaCd_3P_3$. (a) Magnetic susceptibility M/H at $H = 70$ kOe for $H \| ab$ and $H \| c$. (b) Magnetization isotherm $M(H)$ at $T = 1.8$ K. (c) Electrical resistivity $\rho(T)$ at $H = 0$ and 90 kOe. (d) The data from (c) for 160 K $< T <$ 190 K. Vertical arrow indicates a minimum in $d\rho(T)/dT$. (e) Specific heat C_p. The inset shows an enlarged plot near the phase transition. Open and closed symbols are the data taken on warming and cooling, respectively. (f) C_p/T vs. T^2. The solid line represents the linear extrapolation of C_p/T below 2.1 K.

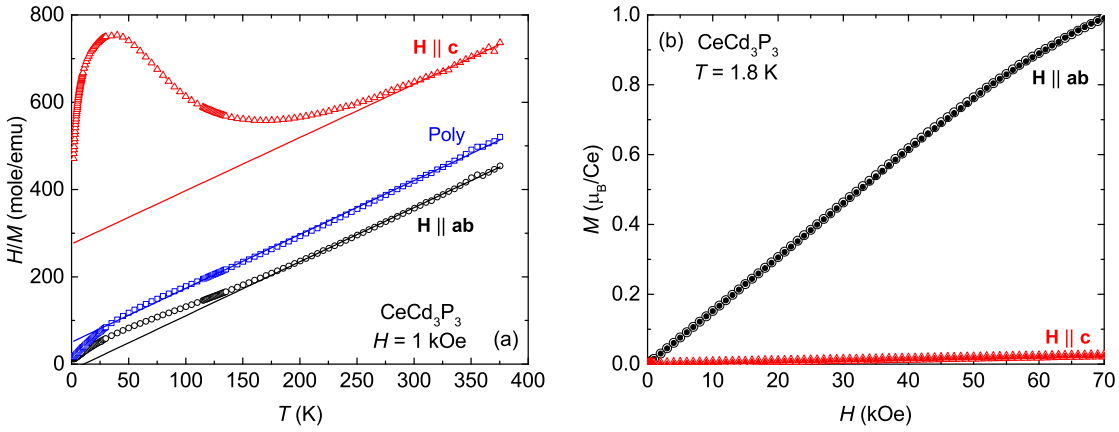

Figure 3.3: (a) Inverse magnetic susceptibility of $CeCd_3P_3$ for $H\|ab$, $H\|c$, and the polycrystalline average, as defined in the text. Solid lines are Curie–Weiss fits to the data. (b) Magnetization isotherms $M(H)$ for $H\|ab$, $H\|c$ at $T = 1.8$ K. Open and closed symbols represent up-sweeps and down-sweeps of the magnetic field, respectively.

data are well described by a Curie–Weiss law, $\chi(T) = C/(T - \theta_p)$, where C and θ_p are the Curie constant and Weiss temperature, respectively. The effective magnetic moments (μ_{eff}) and θ_p values estimated from $1/\chi(T)$ are 2.56 μ_B and -225 K for $H\|c$, 2.54 μ_B and 10 K for $H\|ab$, and 2.54 μ_B and -40 K for the polycrystalline average, respectively. Note that for $H\|c$, μ_{eff} and θ_p are highly dependent on the fitting range, and the results quoted above are for a fit performed in the range 300 K to 375 K. The effective moments obtained are close to the theoretical value of $\mu_{\text{eff}} = 2.54\ \mu_B$ for free Ce^{3+} ions. The large negative θ_p for χ_{poly} indicates strong antiferromagnetic coupling in $CeCd_3P_3$. The deviation of magnetic susceptibility from a Curie-Weiss law below ~ 250 K can be attributed to CEF effects. It should be noted that μ_{eff} and θ_p inferred from the polycrystalline average are consistent with earlier work on polycrystalline samples, which reported $\mu_{\text{eff}} = 2.77\ \mu_B$ and $\theta_p = -60$ K [101]. Furthermore, these values are rather similar to findings on $CeCd_3As_3$ [102] and $CeZn_3As_3$ [110] powder samples. Since the magnetic susceptibility at high temperatures is strongly influenced by the CEF, μ_{eff} and θ_p are also estimated by fitting the $1/\chi(T)$ curve below 10 K: $\mu_{\text{eff}} = 2.03\ \mu_B$ and $\theta_p = -4$ K for $H\|ab$; $\mu_{\text{eff}} = 1.7\ \mu_B$ and $\theta_p = -4.1$ K for the polycrystalline average. It should be noted that $1/\chi(T)$ for $H\|c$ shows no linear temperature dependence below the maximum around ~ 50 K.

Figure 3.3(b) shows the magnetization $M(H)$ measured for $H\|c$ and $H\|ab$ in fields up to 70 kOe at $T = 1.8$ K. No hysteresis loop is observed for either orientation of magnetic field. $M(H)$ displays a large anisotropy between $H\|c$ and $H\|ab$, reflecting two-dimensional magnetic behavior, as expected from the crystal structure and the easy-(ab) plane of magnetization. $M(H)$ for $H\|c$ is very small and increases linearly up to 70 kOe, whereas $M(H)$ for $H\|ab$ increases linearly up to 45 kOe and starts to roll over slightly at higher magnetic fields, reaching a value of $\sim 1\ \mu_B/Ce^{3+}$ at 70 kOe. $M(H)$ at 70 kOe is smaller than that

expected from the theoretical value of $gJ = 2.14\ \mu_B$, obtained using the $J = 5/2$ free-ion result for Ce^{3+}.

Figure 3.4(a) compares $C_p(T)$ of $CeCd_3P_3$ with that of $LaCd_3P_3$. On cooling, $C_p(T)$ of $CeCd_3P_3$ reveals a somewhat broadened λ-like feature at $T_s \sim 127$ K, and a sharp λ-like anomaly at $T_N = 0.41$ K, as seen in Figs. 3.4(b) and (c), respectively. No thermal hysteresis is observed at either transition. Note that previous magnetic susceptibility measurements on polycrystalline material reported no indications of magnetic ordering or electronic structure changes down to 0.48 K [101]. In the new single crystal measurements, the anomaly at 0.41 K and the large specific heat below 5 K prevent us from using the $C_p(T) = \gamma T + \beta T^3$ analysis to estimate γ and Θ_D directly from low temperature data. Instead, using a linear fit to C_p/T vs. T^2 above 5 K, shown in Fig. 3.4(d), we find that the Debye temperature is $\Theta_D \sim 140$ K and that the electronic specific heat coefficient is consistent with zero. The negligibly small γ value suggests either a small effective mass or low density for the charge carriers in $CeCd_3P_3$.

The magnetic contribution to the specific heat, C_m, of $CeCd_3P_3$ is obtained by subtraction of data obtained on the nonmagnetic analog $LaCd_3P_3$. Figure 3.5 shows C_m (solid circles, left axis) together with the magnetic entropy S_m (solid line, right axis). In addition to the λ-like anomalies at T_N and T_s, two distinct features are observed in C_m: i) a broad feature above T_N, indicative of a large electronic contribution (large C_m/T) to the magnetic specific heat; and ii) a broad local maximum at ~ 150 K, suggestive of a Schottky contribution. Note that the sharp features at 127 K and 173 K are due to the non-coincident structural phase transitions in $CeCd_3P_3$ and $LaCd_3P_3$. Because of the magnetic ordering below 0.41 K, an unambiguous extrapolation of the specific heat to $T = 0$ cannot be made. Thus, the integration of C_m/T has been performed from the base temperature of 0.37 K. This will underestimate the total magnetic entropy, especially at low temperatures. At T_N, roughly 20% of the $R\ln(2)$ entropy is released as seen from Fig. 3.5. Above T_N, S_m increases smoothly towards higher temperatures and approaches 5 J/mole-K around 5 K, which is smaller than $R\ln(2)$. When the missing entropy below 0.37 K ($\sim$1 J/mole-K) is taken into account, we believe that the true value of this entropy is $R\ln(2)$, consistent with a Kramers doublet ground state. With further increasing temperature, S_m increases smoothly towards higher temperature, merging with the doublet-ground-state $R\ln(2)$ entropy value at about 40 K. The full $R\ln(4)$ entropy is recovered at around 200 K. The dashed line in Fig. 3.5 represents a three-level Schottky contribution with the first excited state at 260 K and the second excited state at 600 K. Thus, the broad local maximum around 150 K can be explained by the effect of thermally excited CEF energy levels.

C_m/T curves for $H \| ab$ are plotted at select magnetic fields in Figs. 3.6(a) and (b). The magnetic ordering temperature T_N increases slightly up to 15 kOe then decreases beyond this field. For $H > 22.5$ kOe, the magnetic ordering is suppressed below the base temperature of the experiment. For $H = 50$ kOe, C_m/T increases logarithmically with

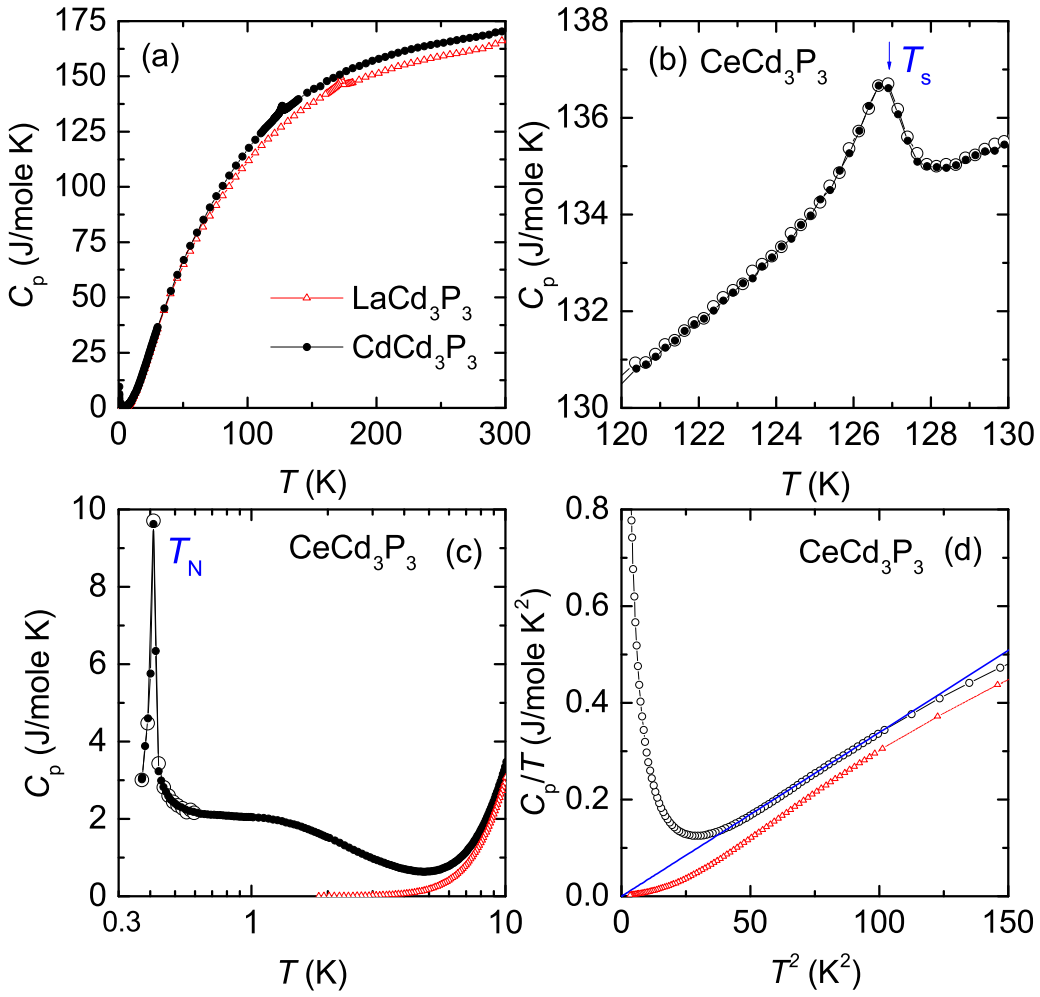

Figure 3.4: (a) Zero field $C_p(T)$ for $CeCd_3P_3$ and $LaCd_3P_3$. (b) $C_p(T)$ of $CeCd_3P_3$ near the phase transition T_s. Open and closed symbols are data taken while cooling and warming, respectively. (c) $C_p(T)$ below 10 K on a logarithmic scale. Open and closed symbols are data taken while cooling and warming, respectively. (d) C_p/T vs T^2. The solid line shows the fit to $\gamma T + \beta T^3$ above 5 K. For comparison, specific heat of $LaCd_3P_3$ is in (c) and (d).

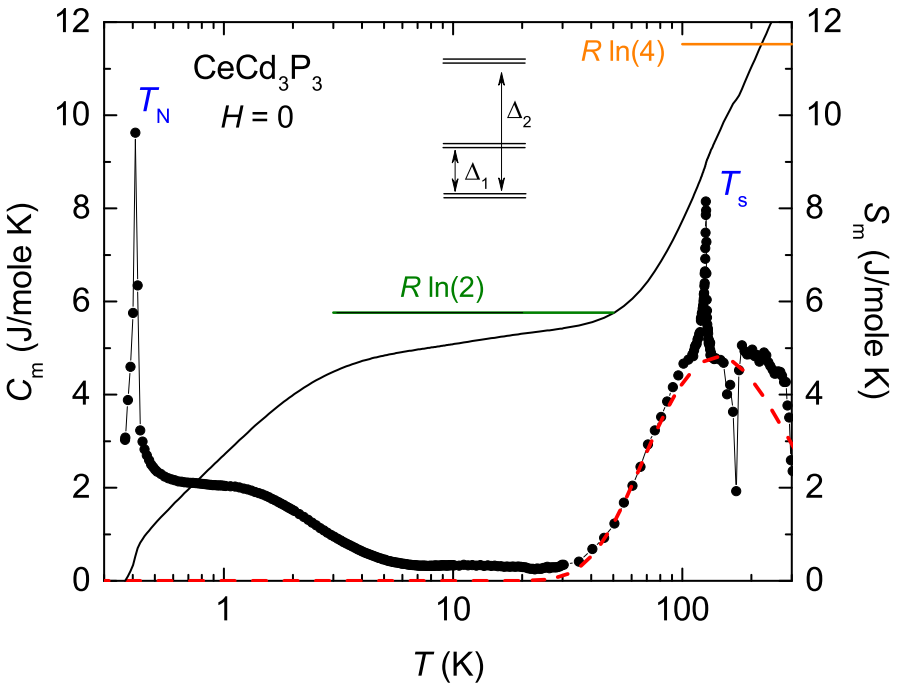

Figure 3.5: Magnetic part of the specific heat C_m (solid circles, left axis) and magnetic entropy S_m (solid line, right axis). The dashed line represents the calculated Schottky contribution, based on a three-doublet configuration with $\Delta_1 = 260$ K and $\Delta_2 = 600$ K.

decreasing temperature below 1.5 K. For $H \geq 60$ kOe, a broad maximum develops in C_m/T and moves to higher temperature as magnetic field increases. The height and width of the maximum cannot be solely ascribed to an electronic Schottky contribution due to Zeeman splitting of the ground state doublet, as shown by the solid line in Fig. 3.6(c), which is calculated for an 8 K energy splitting.

The specific heat as a function of field, $C_p(H)$, is shown in Fig. 3.6(d). The $C_p(H)$ curve at $T = 0.41$ K indicates three peaks at $H = 1.2$, 3.2, and 19 kOe. No hysteresis is detected for these peaks. For $H > 19$ kOe, $C_p(H)$ drops sharply with a slope change around 50 kOe. This slope change becomes a broad local maximum and moves toward higher field as temperature increases. Figure 3.6(e) shows $C_m(H)/T$ as a function of magnetic field, extracted from the specific heat measurement as a function of temperature in a constant field. Data taken from $C_p(H)$ at $T = 0.41$ K (open circles) are also shown. For $H < 50$ kOe, $C_m(H)/T$ indicates large peaks due to magnetic ordering. $C_m(H)/T$ at $T = 0.37$ K shows a maximum at ~ 2 kOe and a peak at ~ 22.5 kOe. When the temperature is increased to 0.43 K, a single peak is observed around ~ 15 kOe. At $T = 0.5$ K, $C_m(H)/T$ depends weakly on field below 50 kOe, but is quickly suppressed above this field. All the anomalies observed in the low temperature specific heat measurements are used to construct a partial H–T phase diagram for $H \| ab$, shown in Fig. 3.6(f). Since magnetic ordering can be suppressed

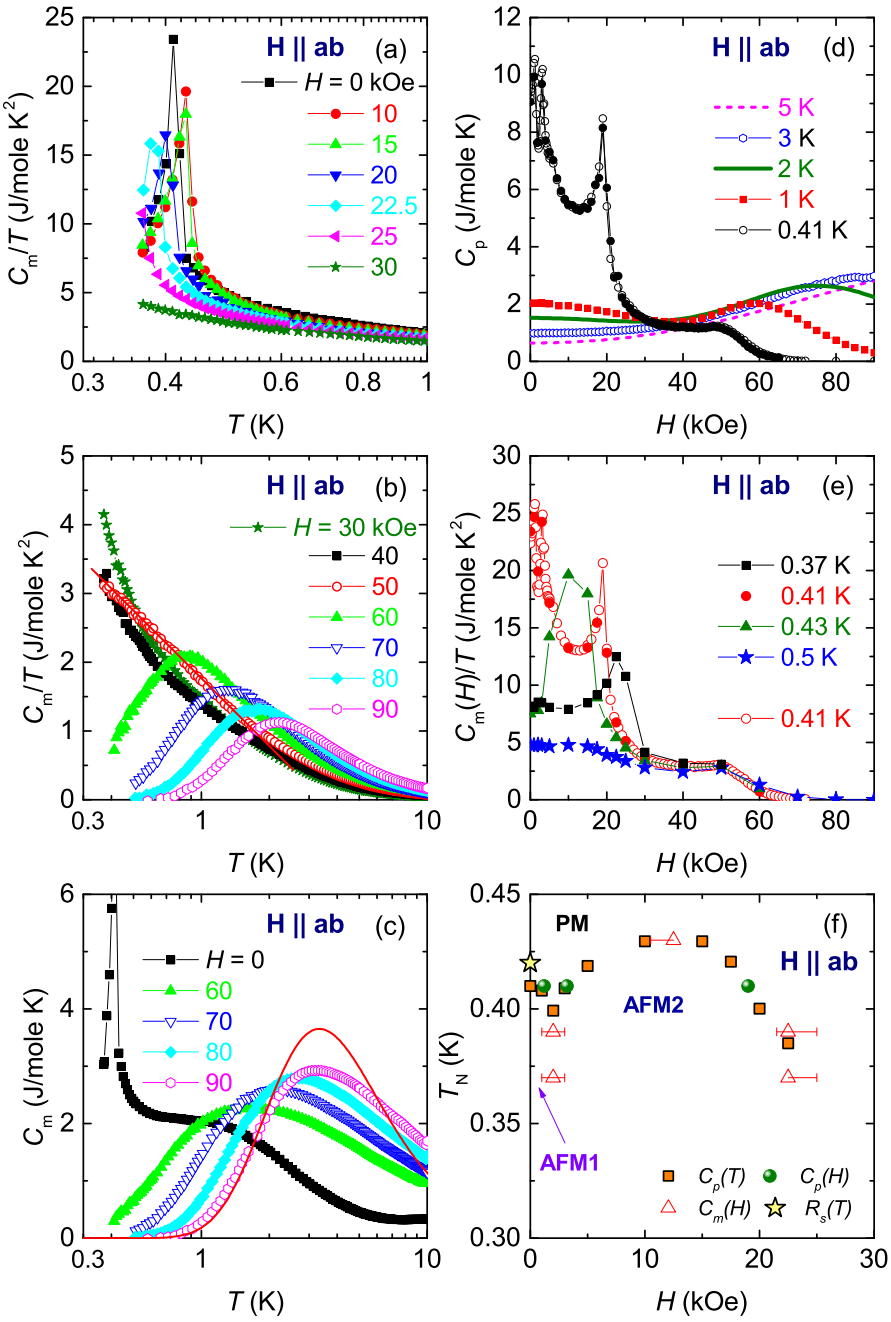

Figure 3.6: $CeCd_3P_3$: Magnetic field dependence of the specific heat for $H||ab$. (a) C_m/T below 1 K at selected magnetic fields. (b) C_m/T below 10 K at selected magnetic fields. Solid lines are guides to the eye. (c) $C_m(T)$ below 10 K at $H = 0$, 60, 70, 80, and 90 kOe. The solid line represents a field-induced Schottky contribution based on two levels split by 8 K. (d) C_p as a function of field at selected temperatures. For $T = 0.41$ K, open and closed symbols are data taken while increasing and decreasing magnetic field. (e) $C_m(H)/T$ as a function of magnetic field at selected temperatures. Open circles for $T = 0.41$ K are obtained from the field dependence $C_p(H)$. Solid symbols are taken from the temperature dependence $C_m(T)$. (f) H–T phase diagram. Solid squares and circles are taken from the peak positions in $C_p(T)$ and $C_p(H)$, respectively. Triangles are taken from the peak position in $C_m(H)$. Star is taken from the microwave surface resistance measurement.

by external magnetic fields, it is expected that the 0.41 K phase transition in zero field is not related to ferromagnetic ordering but instead antiferromagnetism. There are at least two ordered antiferromagnetic phases, denoted AFM1 and AFM2, and a paramagnetic phase, PM.

Figure 3.7(a) shows $\rho(T)$ for $CeCd_3P_3$, for currents flowing in the ab-plane (ρ_{ab}) and along the c-axis (ρ_c). The resistivity is anisotropic, with ρ_{ab} about 5 times larger than ρ_c at 300 K, where the resistivity values are 28.12 mΩ-cm and 5.16 mΩ-cm, respectively. $\rho(T)$ decreases with decreasing temperature, indicating metallic behavior for both current directions. Note that no pronounced resistivity anisotropy is observed in a La-based analogous compound.

There is a nonmonotonic feature around $T_s = 128$ K, with the local minimum in ρ_{ab} determined from the zero crossing in $d\rho/dT$ and indicated by the arrow in the inset of Fig. 3.7(a). There is no evidence of thermal hysteresis. Since the resistivity of $LaCd_3P_3$ also shows a similar anomaly, around 173 K, it is likely the same phenomenon is responsible in both compounds. It should be noted that the earlier study of polycrystalline $CeCd_3P_3$ indicated semiconducting behavior and showed no such phase transition at T_s [101]. A small positive magnetoresistance (MR) is observed in $CeCd_3P_3$ across the entire measured temperature range, and an applied magnetic field of 90 kOe does not shift T_s. Due to the large contact resistance ($\sim$50 Ω at 300 K) in the dc resistivity measurements, microwave measurements were instead performed below 5 K. The surface resistance, $R_s(T)$, shown in Fig. 3.7(b), increases with decreasing temperature and displays a slope change at 0.42 K [Fig. 3.7(c)]. The phase transition temperature is determined from the change in slope of R_s(T), and is consistent with the specific heat results presented earlier.

It is notable that $\rho(T)$ of both the La- and Ce-compounds is much larger than the resistivity values usually observed in rare-earth-based intermetallic compounds, suggesting a low carrier concentration in these systems. As a further probe of the carrier-density, the Hall resistivity ρ_H has been measured as a function of temperature and magnetic field. ρ_H curves for $CeCd_3P_3$ are plotted as a function of field in the inset of Fig. 3.8 at selected temperatures, where it is seen that ρ_H is linear in field and positive for the entire temperature range. The temperature dependence of the Hall coefficient, $R_H = \rho_H/H$, is plotted for $H = 90$ kOe in Fig. 3.8. It should be emphasized that ρ_H/H is effectively temperature independent and indicates only a tiny jump at the phase transition $T_s = 128$ K. The positive sign of ρ_H/H indicates that transport is dominated by hole-like carriers. Based on a one-band model the carrier-density is estimated to be $\sim 6 \times 10^{20}/\text{cm}^3$ at 300 K, which corresponds to ~ 0.002 carriers per formula unit (f.u.), confirming the low carrier-density. Thus, the negligibly small γ values for $LaCd_3P_3$ and $CeCd_3P_3$ (obtained from the high temperature C/T vs. T^2) are due to the low carrier-density in these compounds.

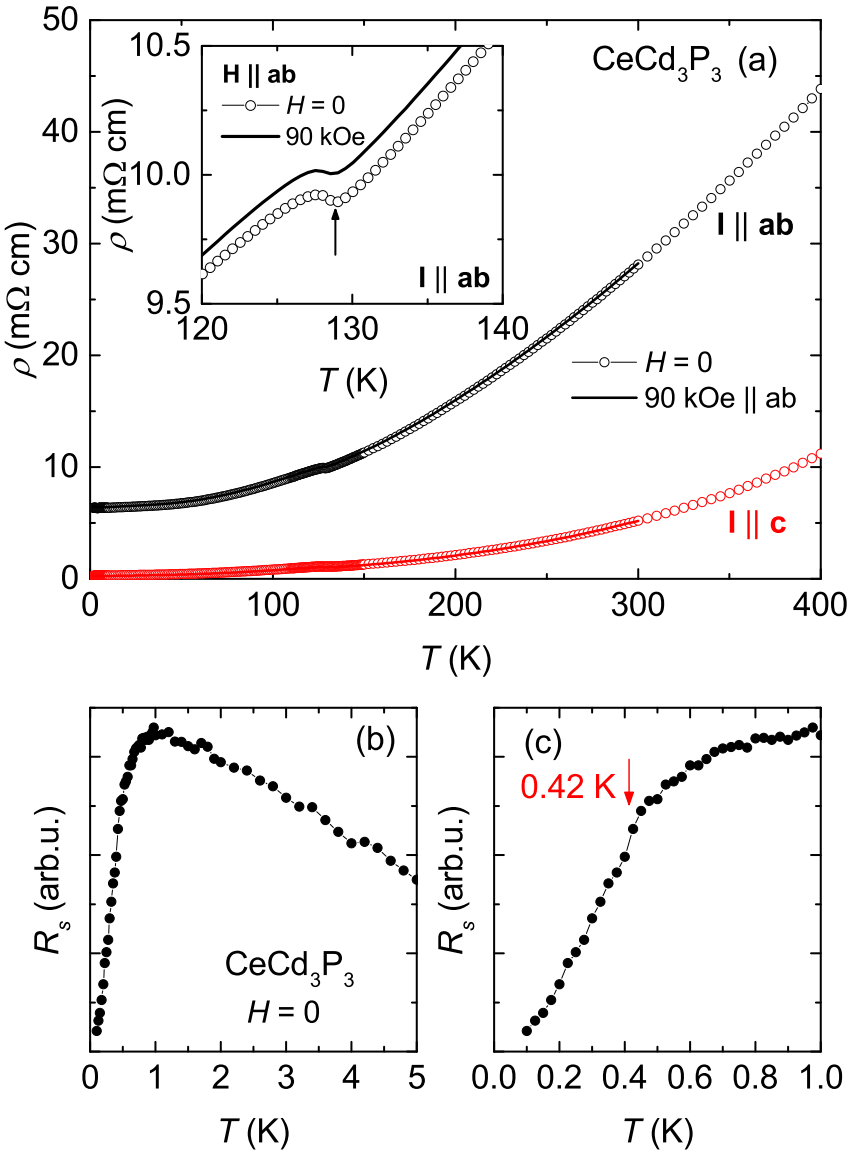

Figure 3.7: (a) $\rho(T)$ curves for $CeCd_3P_3$ for currents flowing in the ab-plane and c-axis, at $H = 0$ and 90 kOe. Inset: enlarged plot near the phase transition T_s for $I \| ab$. Vertical arrow indicates the location of the local minimum in $\rho_{ab}(T)$ obtained, from a $d\rho/dT$ analysis. (b) Microwave surface resistance, R_s, below 5 K. (c) Enlarged plot of R_s below 1 K. Vertical arrow indicates the phase transition temperature.

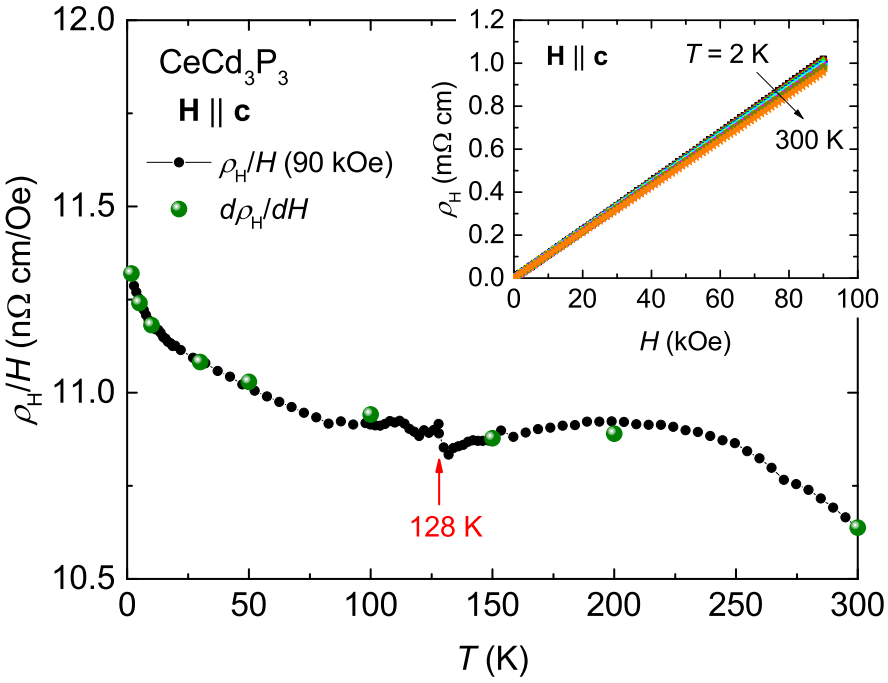

Figure 3.8: Hall coefficient ρ_H/H of $CeCd_3P_3$ at $H = 90$ kOe. Solid symbols are taken from the field dependence of Hall resistivity ρ_H. The inset shows ρ_H curves measured at fixed temperatures of $T = 2$, 5, 10, 30, 50, 100, 150, 200, and 300 K (top to bottom). The Hall coefficients, $d\rho_H/dH$, obtained from linear fits, are consistent with the ρ_H/H temperature sweep data.

3.5 Discussion

Due to the strong spin-orbit coupling and CEF, combined with the trigonal point symmetry of the Ce-atom, the ground state of Ce^{3+} ions in $CeCd_3P_3$ is a Kramers doublet. Many Ce-based compounds with trigonal point symmetry show a similar CEF scheme with a very pronounced easy-plane anisotropy and a small c-axis magnetization. For example, the anisotropic $\chi(T)$ curves and θ_p values of $CeCd_3P_3$ are rather similar to those of $CeIr_3Ge_7$ [111] and $CeCd_3As_3$ [102] compounds. A comprehensive analysis of the CEF scheme of Ce^{3+} in the trigonal point symmetry has been presented in Ref. [111], where a strong easy-plane anisotropy is originates from large positive CEF parameters B_2^0 and B_4^3. Note that the mixing CEF parameter B_4^3 is absent for the sixfold point symmetry in hexagonal systems, resulting in pure $|\pm 1/2\rangle$, $|\pm 3/2\rangle$, and $|\pm 5/2\rangle$ CEF doublets [115, 111] Unlike the sixfold case, the presence of B_4^3 in trigonal symmetry induces mixing of the $|\pm 5/2\rangle$ and the $|\mp 1/2\rangle$ states in the ground-state doublet. For isostructural $CeCd_3As_3$, the highly anisotropic $\chi(T)$ is well reproduced by this CEF calculation, where the energy splittings between the ground state and the first and second excited states are $\Delta_1 = 241$ K and $\Delta_2 = 282$ K [111]. Although we have not attempted to extend the CEF calculation of Ref. [111] to $CeCd_3P_3$, we have carried out a fit to specific heat data using the three-doublet scheme shown in Fig. 3.5. Based on the specific heat analysis, the CEF scheme of $CeCd_3P_3$ is quite similar to that of $CeCd_3As_3$, except for a larger overall splitting, where the second excited state is located at $\Delta_2 = 600$ K. Since the ground state Kramers doublet is well isolated from the excited states, the low temperature thermodynamic and transport properties of $CeCd_3P_3$ must be governed by the low energy state of the Ce^{3+} ions. Therefore, the 2D magnetism of $CeCd_3P_3$ cannot be explained solely on the basis of an effective $J_{\text{eff}} = 1/2$ ground state, but both $|\pm 5/2\rangle$ and $|\mp 1/2\rangle$ contributions must be considered together.

It is notable that the high temperature anomaly at T_s in $\rho(T)$ of RCd_3P_3 is observed at the same temperature as the λ-like anomaly in the specific heat. The failure to observe a corresponding anomaly in $\chi(T)$ means that this transition cannot have a magnetic origin. In addition, the isostructural RAl_3C_3 (R = Ce, Dy, Er, Tm, Yb, and Lu) compounds show clear structural phase transitions [93]. Considering that the crystal structures are of the same type as the RAl_3C_3 materials, it is reasonable to assume that the high temperature anomalies observed in the RCd_3P_3 compounds have a structural origin. $\rho(T)$ and ρ_H/H only show a small jump at T_s, and it is expected that the change of Fermi surface volume on passing through the phase transition will be small due to the low carrier-density. Note that $\rho(T)$ and ρ_H/H in the low carrier-density $YbAl_3C_3$ compound also only display a small jump at the structural phase transition [91]. The carrier-density of $CeCd_3P_3$ (0.002 carriers per f.u.) is about five times smaller than that of $YbAl_3C_3$ (0.01 carriers per f.u.) [91]. Detailed x-ray measurements of RCd_3P_3 are underway to clarify the nature of the transition at T_s.

Since the specific heat contains a large electronic contribution above T_N (the broad feature below 5 K shown in Fig. 3.5), an interesting question arises as to whether the $4f$ electrons in $CeCd_3P_3$ are hybridized with the conduction electrons. It is a well known fact that the specific heat of many Ce- and Yb-based Kondo-lattice compounds display similar broad features at low temperatures, with large γ values (due to the Kondo effect), accompanied by resistivities that show either maxima or logarithmic upturns resulting from Kondo scattering in conjunction with the CEF [116]. The resistivity of $CeCd_3P_3$ instead suggests non-hybridized metallic behavior (Fig. 3.7), in which the effects typically associated with a Kondo lattice system are absent. One possible explanation of the local moment behavior in $CeCd_3P_3$ is that there are simply not enough carriers to screen the f-electron moments. Supporting this interpretation, Kondo lattice compounds generally show a negative magnetoresistance at low temperatures [116]. By contrast, a small positive MR is observed in $CeCd_3P_3$ over the entire temperature range measured. Significantly, except for the difference in temperature of the anomalies at T_s, $\rho(T)$ in $CeCd_3P_3$ is the same as in $LaCd_3P_3$. Therefore, as there is no sign of a Kondo contribution to the resistivity, we speculate that the large electronic specific heat below 5 K is due to the effects of magnetic frustration. In a frustrated system, the presence of several competing states leads to a very large number of low-lying excitations, which manifests as an anomalously large specific heat at low temperatures [66]. It should be noted that to rigorously exclude heavy fermion behaviour, the specific heat of $CeCd_3P_3$ will need to be measured down to temperatures much lower than T_N.

A further indication of the significance of frustration comes from the frustration parameter $f = |\theta_p/T_N|$, which we estimate to be of the order of 100 for $CeCd_3P_3$, based on the polycrystalline average $\theta_p \sim -40$ K and $T_N = 0.41$ K. This is sufficiently large to indicate that magnetic frustration may indeed play a dominant role at low temperatures. Applying a magnetic field within the easy plane raises T_N to higher temperatures, demonstrating partial lifting of frustration. In addition, the small amount of magnetic entropy released at T_N and the full $R\ln(2)$ entropy recovered at much higher temperatures indicate a competition between AFM order and frustration. Therefore, frustration effects associated with the oscillatory nature of the RKKY exchange interaction may be important in this system. It has been shown that frustrated itinerant magnets with localized f-moments (no Kondo effect) and a small Fermi surface display an increase of the resistivity with decreasing temperature, where the frustration is necessary to observe the resistivity upturn produced by the RKKY mechanism [117]. Although due to high contact resistance in our $CeCd_3P_3$ samples the dc resistivity cannot be directly measured, the microwave surface resistance R_s clearly indicates a non-logarithmic resistivity increase at low temperatures. Interestingly, a recent study of the frustrated, metallic, 2D-TL antiferromagnet $PdCrO_2$ found that long-range interactions such as RKKY do not compete with the spin frustration [118]. The electrical resistivity above T_N showed a sub-linear temperature dependence as a characteristic of the

frustrated metallic magnetism, while the conduction electrons in $PdCrO_2$ do not strongly affect the spin frustration below T_N, which was evidenced by the 120° spin structure.

From magnetization measurements, it is clear that the spins in $CeCd_3P_3$ are strongly easy-plane due to the CEF, giving rise to an XY spin system. The partial H–T phase diagram of metallic $CeCd_3P_3$ shown in Fig. 3.5(f) is similar to that of 2D insulating triangular lattice systems with easy-plane anisotropy [78, 88]. A well known example of a quasi-2D easy-plane (XY) TL system is insulating $RbFe(MoO_4)_2$ [119], where the obtained magnetic phase diagram is similar to the theoretical calculation for the XY model [87, 88, 120, 121]. Based on a classical Heisenberg model for an insulating system, the phase diagram should display a magnetic structure change from a 120° structure in zero field to the up-up-down (uud) structure with increasing magnetic field, leading to a 1/3 magnetization plateau [88]. Indeed, multiple magnetic-field-induced metamagnetic transitions have been observed in many TL systems such as insulating Cs_2CuBr_4 [122] and metallic $Sr_3Ru_2O_7$ [123]. However, the interaction between spin-orbit entangled Kramers-doublet local moments on a planar triangular lattice is rather complex from a theoretical point of view [67, 81, 83, 84]. By this analogy with insulating triangular lattice systems, it would therefore be interesting to measure magnetization below T_N to determine whether a magnetization plateau corresponding to the uud structure exists in the $CeCd_3P_3$ compound. However, we suspect that the 120° magnetic order may not be stable in $CeCd_3P_3$. The triangular lattice will be distorted on passing through the high temperature (structural) phase transition (T_s), resulting in spatially anisotropic exchange interactions. This may resemble the case of $YbAl_3C_3$, where the structural phase transition from hexagonal to orthorhombic distorts the equilateral triangular lattice [124, 94]. A similar situation could occur in $YbMgGaO_4$, where Ga- and Mg-site mixing may destroy the 120° magnetic order and induce a quantum spin-liquid state [125, 126].

Since the magnetic ordering in $CeCd_3P_3$ can be suppressed by relatively small magnetic fields, in spite of the large θ_p, a zero temperature phase transition can be expected. The metallic nature of $CeCd_3P_3$ naturally introduces an interplay between RKKY and Kondo interactions. However, the hybridization between f-electrons and conduction electrons is very weak, which, in turn, suggests that the magnetic field will induce behavior that is distinct from that in ordinary heavy fermion systems. Taking into account the frustrated nature of the $CeCd_3P_3$ crystal structure and the strong AFM interactions, the ground state is expected to be degenerate. This degeneracy will be partially lifted by the high temperature (structural) phase transition T_s and the onset of antiferromagnetic ordering below T_N. The finite specific heat up to 50 kOe at 0.5 K (Fig. 3.6) and unusual temperature dependence of $C_m/T \sim \log(1/T)$ for $H = 50$ kOe points to there being a degeneracy, implying that the frustration is not fully relieved by the phase transitions. Although $CeCd_3P_3$ is metallic, it is expected that the geometrically frustrated nature of the low temperature phase is the key to understanding the anomalous specific heat behavior. Recently, an experimental and

theoretical effort has been underway to classify and understand the global phase diagram of AFM heavy fermion metals, where the degree of local moment quantum fluctuations can be tuned by dimensionality or geometrical frustration [48, 104, 105, 106, 107, 49, 50, 108]. We expect that $CeCd_3P_3$, in which the Kondo coupling is negligible, will have a key role to play in developing such a phase diagram. This in turn raises questions such as: whether the long-range magnetically ordered phase in $CeCd_3P_3$ really displays similar physics to that of a heavy fermion system; and the nature of the interplay between magnetic frustration and the RKKY interaction. Further detailed investigations of low temperature physical properties will be necessary to address these points.

3.6 Summary

X-ray, magnetization, electrical and Hall resistivity, and specific heat measurements have been performed on single crystal RCd_3P_3 (R = La and Ce) compounds. The results obtained for $CeCd_3P_3$ provide evidence of strongly anisotropic quasi-2D magnetism; an emergent spin-orbit entangled doublet ground state of Ce at low temperatures; a low carrier-density metallic state without Kondo lattice behavior; a high temperature (structural) phase transition at $T_s = 127$ K; and low temperature antiferromagnetic ordering at $T_N = 0.41$ K. A partial H–T phase diagram has been constructed above 0.37 K, in which the antiferromagnetic order initially increases with magnetic field before being suppressed to lower temperatures at higher fields. The specific heat in zero field indicates a large electronic contribution (C_m/T) below ~ 5 K, which persists up to 50 kOe. Although it only occurs over a limited temperature range, C_m/T at 50 kOe shows a logarithmic temperature dependence $C_m/T \sim \log(1/T)$. In conclusion, the complex interplay between the low carrier-density metallic state and frustrated magnetism may make $CeCd_3P_3$ an ideal system in which to explore strong correlation effects in a metallic host.

Chapter 4

Anisotropic magnetic property of single crystals $R\mathrm{V_6Sn_6}$ (R = Y, Gd - Tm, Lu)

4.1 Abstract

$R\mathrm{V_6Sn_6}$ (R = Y, Gd - Tm, Lu) single crystals are synthesized by Sn-flux method and their physical properties are characterized by magnetization, resistivity, and specific heat measurements. Powder X-ray diffraction patterns of all samples can be well indexed with the hexagonal $\mathrm{HfFe_6Ge_6}$-type structure, where rare-earth atoms form hexagonal layers and vanadium atoms form Kagome layers. At high temperatures, magnetic susceptibility measurements of moment bearing rare-earths (R = Gd - Tm) follow Curie-Weiss behavior. Effective moments estimated from the polycrystalline average of magnetic susceptibility curves are consistent with the values for free R^{3+} ions. Strong magnetic anisotropy due to crystalline electric field effects is observed for moment bearing rare-earths, except $\mathrm{GdV_6Sn_6}$. The easy magnetization direction is determined to be c-axis for R = Tb - Ho and ab-plane for R = Er and Tm. The vanadium ions in $R\mathrm{V_6Sn_6}$ possess no magnetic moment. The compounds for R = Y and Lu exhibit typical characteristics of paramagnetic metals. At low temperatures, the magnetic ordering is confirmed from magnetization, specific heat, and resistivity: the highest $T_N = 4.9$ K for $\mathrm{GdV_6Sn_6}$ and the lowest $T_N = 2.3$ K for $\mathrm{HoV_6Sn_6}$. No magnetic ordering is observed down to 1.8 K for R = Er and Tm. A slight deviation of the magnetic ordering temperature from the de Gennes scaling suggests the dominant Ruderman-Kittel-Kasuya-Yosida (RKKY) exchange interaction between rare-earth moments in metallic $R\mathrm{V_6Sn_6}$ compounds.

4.2 Introduction

Intermetallic compounds with the chemical formula RT_6X_6 (R = rare-earth, T = V, Cr, Mn, Fe, Co, X = Ge , Sn) have shown complex magnetic and electronic properties that are

emerged from the interplay between localized $4f$ and itinerant $3d$ electrons [127, 128, 129, 130, 131, 132]. The RT_6X_6 compounds crystallize into either the fully ordered $HfFe_6Ge_6$-type or other disordered YCo_6Ge_6-type or $SmMn_6Sn_6$-type structure, depending on the size of the constituent R, T, and X atoms [127, 133, 134, 135]. In these crystal structures the rare-earth ions form hexagonal layers and the transition metal ions form Kagome layers. When both R and T bear magnetic moments in their sublattices such as RMn_6Sn_6, the compounds show temperature dependent magnetic structures which are governed by the relative strength of R-R, R-T, and T-T exchange couplings [136, 129]. In RMn_6Sn_6, a strong antiferromagnetic coupling between rare-earth and Mn sublattices leads to a simultaneous ordering of both sublattices [128], where the compounds with R = Gd - Ho show a collinear ferrimagnetic ordering above room temperatures and the compounds with R = Er and Tm show an antiferromagnetic ordering of Mn sublattice at high temperatures followed by a ferrimagnetic ordering of R sublattice at low temperatures [137]. The magnetic structure of these compounds is highly dependent on crystalline electric field (CEF) [137]. It has been observed that when the transition metals bear no magnetic moment (e.g. T = Cr and Co), a very low magnetic ordering temperature arises only from the rare-earth sublattice. For example, RCr_6Ge_6 compounds indicate the magnetic ordering below 15 K [138, 131] and RCo_6X_6 (X = Ge, Sn) compounds show the magnetic ordering below 3 K [139, 140]. In particular, $GdCo_6Sn_6$ is a paramagnet down to 1.8 K [140].

In recent years, there have been considerable efforts to investigate topologically nontrivial states associated with the Kagome lattice [141, 142, 143]. The RV_6Sn_6 compounds have gained attention due to their topologically nontrivial band structures [144, 145, 146], where RV_6Sn_6 can host 2D Kagome surface states [147]. Measurements using an angle resolved photoemission spectroscopy (ARPES) on single crystals of RV_6Sn_6 (R = Gd and Ho) and density functional theory calculations show characteristics of Dirac cone, saddle point, and flat band, which arise from the vanadium Kagome lattice [147]. It is also suggested that Dirac crossing at the K-point gives rise to non-linear Hall resistivity in GdV_6Sn_6 and YV_6Sn_6 [148].

Despite growing interest in electronic properties in the RV_6Sn_6 series, their magnetic properties have not yet been studied, except for R = Gd and Y. Magnetization measurements on single crystals of RV_6Sn_6 (R = Gd and Y) confirm that vanadium (V) ions possess no magnetic moments and Gd ions order antiferromagnetically below ~5 K [148, 149]. Since the transition metal V is non-magnetic, RV_6Sn_6 would provide an opportunity to study magnetic properties arising solely from the rare-earth triangular lattice. It has been reported that single crystals of RV_6Sn_6 grown by the flux method adopt the $HfFe_6Ge_6$-type for R = Gd and Y [148], whereas polycrystalline samples of RV_6Sn_6 grown by the arc melt technique adopt the $SmMn_6Sn_6$-type for R = Gd - Tm and Lu and the $HfFe_6Ge_6$-type for R = Y [150]. In this report, we present the crystal structure and physical properties of RV_6Sn_6 (R = Y, Gd - Tm, Lu) single crystals grown by Sn-flux.

Single crystals of RV$_6$Sn$_6$ (R = Y, Gd - Tm, Lu) were grown by Sn-flux [65]. The constituent elements were cut into smaller pieces and placed in an alumina crucible in the ratio R : V : Sn = 1 : 6 : 62, and then sealed into an amorphous silica tube under partial argon atmosphere. The ampoule was heated up to 1225 °C over three hours, held there for five hours, and then slowly cooled down to 850 °C at a rate of 1.25 °C/hr. Single crystals were separated from the flux by centrifuging. The obtained single crystals have a plate-like morphology with a clean hexagonal facet (ab-plane) being the base of the plate as shown in the inset of Fig. 4.1(c). All grown single crystals have similar hexagonal morphology, but compounds with heavier rare-earth elements tend to form thicker single crystals. The average thickness of the obtained single crystals varies from ∼0.2 mm (GdV$_6$Sn$_6$) to ∼1 mm (LuV$_6$Sn$_6$).

To verify the crystal structure of the title compounds and their lattice parameters, powder X-ray diffraction (XRD) patterns of crushed single crystals were collected in a Rigaku MiniFlex diffractometer at room temperature and analyzed using a *GSAS-II* software [151]. Si standard was used to minimize the instrumental error. The dc magnetization as a function of temperature from 1.8 to 300 K and magnetic fields up to 70 kOe was measured in a Quantum Design (QD) Magnetic Property Measurement System (MPMS). Four-probe ac resistivity measurements were performed with $I \parallel ab$ from 300 K down to 1.8 K in a QD Physical Property Measurement System (PPMS). Specific heat was measured by the relaxation technique down to 1.8 K in a QD PPMS.

4.3 Results and discussion

4.3.1 Crystal structure

The obtained and calculated powder XRD patterns for TbV$_6$Sn$_6$, as a representative example in the series, are shown in Fig. 4.1(a). The observed peak positions are well indexed by the fully ordered HfFe$_6$Ge$_6$-type structure ($P6/mmm$, no. 191). In earlier studies the two structural prototypes for RV$_6$Sn$_6$ compounds are reported [Fig. 4.1(b)]: single crystalline samples (grown by Sn-flux) for R = Gd and Y [148] crystallize into the fully occupied HfFe$_6$Ge$_6$-type; polycrystalline samples (synthesized by arc melt) crystallize into the HfFe$_6$Ge$_6$-type for R = Y and the SmMn$_6$Sn$_6$-type for R = Gd - Tm [150]. The SmMn$_6$Sn$_6$-type is a disordered variant of the HfFe$_6$Ge$_6$-type. In the SmMn$_6$Sn$_6$-type, the fractional occupancy of additional R and Sn sites are reported to vary from 3 to 10 %, depending on R [150]. In this study, the fully ordered HfFe$_6$Ge$_6$-type structure is used to analyze the powder XRD patterns as it does not show any appreciable difference between the observed and calculated intensities, as shown in Fig. 4.1(a). The detection of subtle difference between the two structure types requires a much higher resolution diffractometer with rigorous Rietveld refinement.

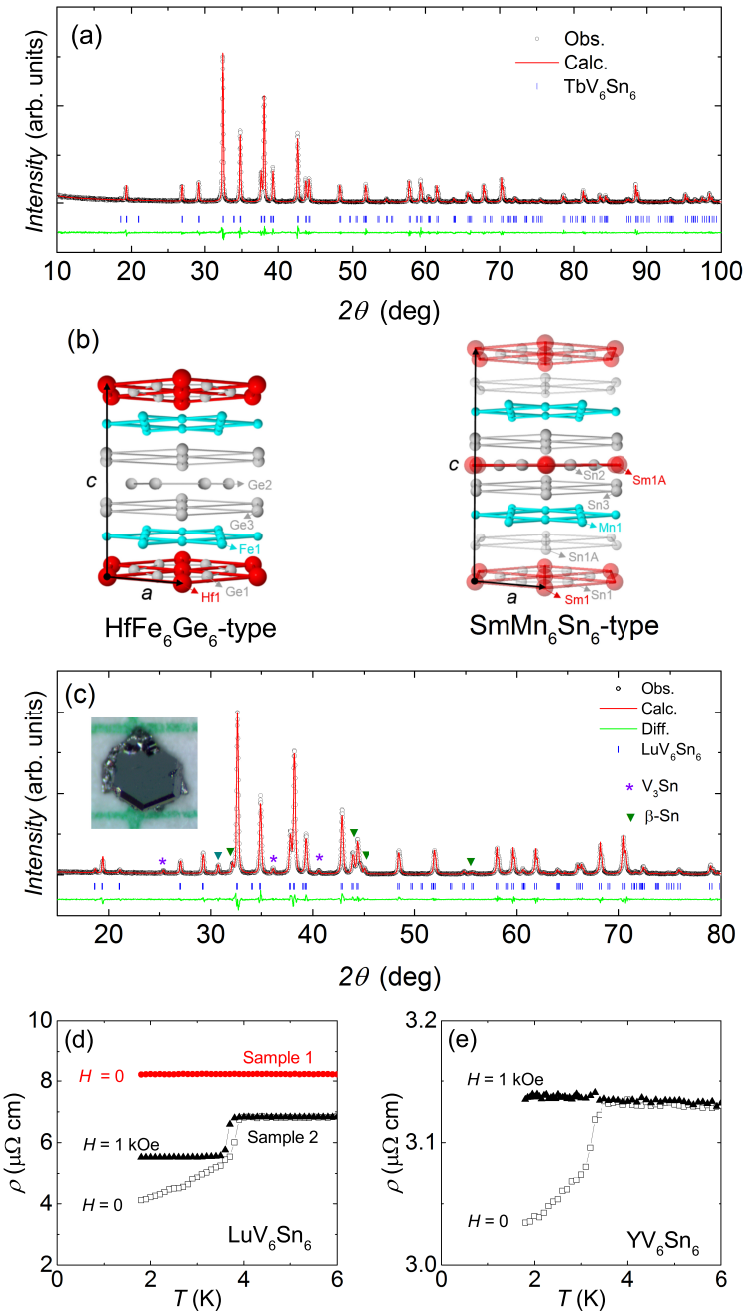

Figure 4.1: (a) Powder XRD patterns of TbV_6Sn_6. Red line is the calculated XRD patterns using $HfFe_6Ge_6$-type structure. Green line represents the difference between the data and calculated patterns. (b) Schematics of $HfFe_6Ge_6$-type and $SmMn_6Sn_6$-type structure. To clearly show hexagonal rare-earth and Kagome transition metal layers c-axis is not drawn to scale, where each layer is shifted upward. (c) Powder XRD patterns of LuV_6Sn_6. Impurity phases of V_3Sn and β-Sn are marked by purple asterisk and green triangle symbols, respectively. Inset shows a photograph of LuV_6Sn_6 on mm grid. (d) Electrical resistivity of two LuV_6Sn_6 samples at $H = 0$ and 1 kOe. (e) Electrical resistivity of YV_6Sn_6 at $H = 0$ and 1 kOe.

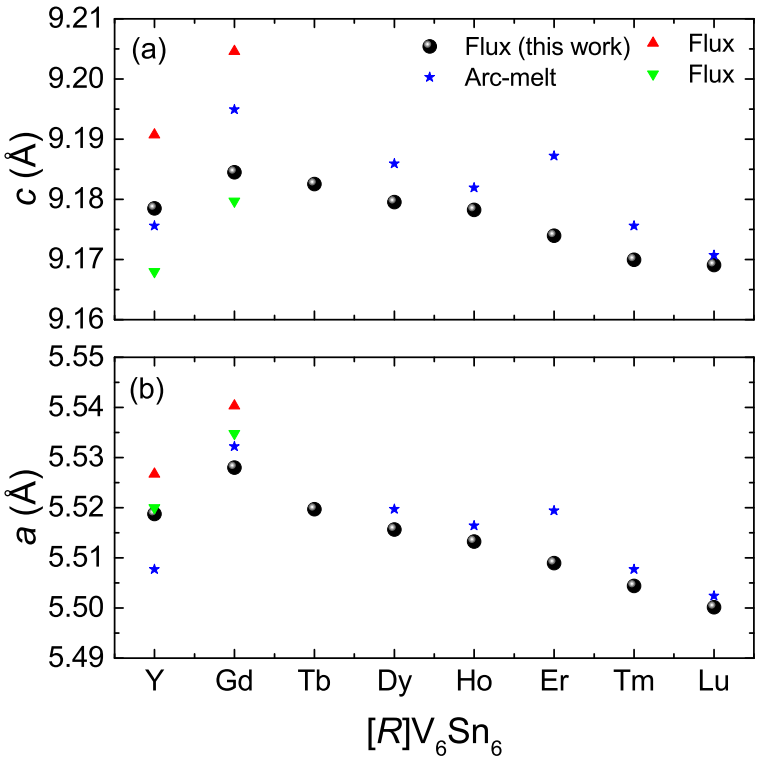

Figure 4.2: (a) Lattice parameter c and (b) lattice parameter a as a function of rare-earth elements [R] (black circles). Blue stars [150], red up-triangles [148], and green down-triangles [149] are taken from other reports.

The obtained lattice parameters c and a are shown in Figs. 4.2(a) and (b), respectively. Both a and c decrease with increasing R atomic number, following lanthanide contraction, implying that the valence state of the heavy rare-earth ions in RV$_6$Sn$_6$ compounds are trivalent. The lattice parameters obtained from earlier studies [148, 149, 150] are included in Fig. 4.2. The variations in lattice parameters are probably due to the different sample quality, refinement with different structure-type, and instrumental error.

4.3.2 Impurity phase

The obtained powder XRD patterns and physical property measurements performed on this series show two minor impurity phases. As shown in Fig. 4.1(c), a traceable amount of V$_3$Sn and β-Sn phases are detected in LuV$_6$Sn$_6$. Note that to demonstrate impurity phases detected in this family of materials the XRD patters, taken without cleaning sample surfaces, are presented in the figure. However, when small pieces of single crystals are carefully collected and surfaces of samples are polished or cleaned by diluted HCl acid, clean XRD patterns can be obtained as like the case for TbV$_6$Sn$_6$. These two are the only impurity phases detected in the RV$_6$Sn$_6$ series and also consistent with impurities found in the previous report [150]. V$_3$Sn and β-Sn phases are known to have superconducting transitions at T_c = 3.8 K [152] and 3.7 K [153], respectively. The presence of these superconducting phases are clearly seen in electrical resistivity, $\rho(T)$, measurements. $\rho(T)$ curves on two different LuV$_6$Sn$_6$ samples are shown in Fig. 4.1(d). Sample 1 and 2 are two different pieces of single crystals grown from the same batch. $\rho(T)$ of the sample 1 indicates no resistivity drop below 4 K. $\rho(T)$ of the sample 2 shows the superconducting transition below 4 K at H = 0, which cannot be fully suppressed by applying magnetic field of 1 kOe. This is probably due to the superconducting V$_3$Sn phase. For the YV$_6$Sn$_6$ sample, its partial superconducting transition can be fully suppressed by a magnetic field of 1 kOe, as shown in Fig. 4.1(e). The superconducting transition in YV$_6$Sn$_6$ probably originates from β-Sn. It should be emphasized that superconducting transitions observed in resistivity measurements are not intrinsic to the ternary compound, as its resistivity does not go to zero below T_c. Thus, the superconducting transition below 4 K originates from impurity phases either on surfaces or embedded within the samples.

4.3.3 LuV$_6$Sn$_6$ and YV$_6$Sn$_6$

The temperature-dependent magnetic susceptibility, $\chi = M/H$, curves for R = Lu and Y at H = 70 kOe are shown in Fig. 4.3(a). Due to the small size of single crystals, multiple pieces of YV$_6$Sn$_6$ were loaded into a gel capsule to measure magnetic susceptibility, which can be considered as a polycrystalline average. At high temperatures M/H curves of both samples are weakly dependent on temperature, while M/H curves at low temperatures exhibit an upturn probably due to paramagnetic impurities. The absolute value of magnetic susceptibility of both compounds is a bit larger than that of typical Y- and Lu-based

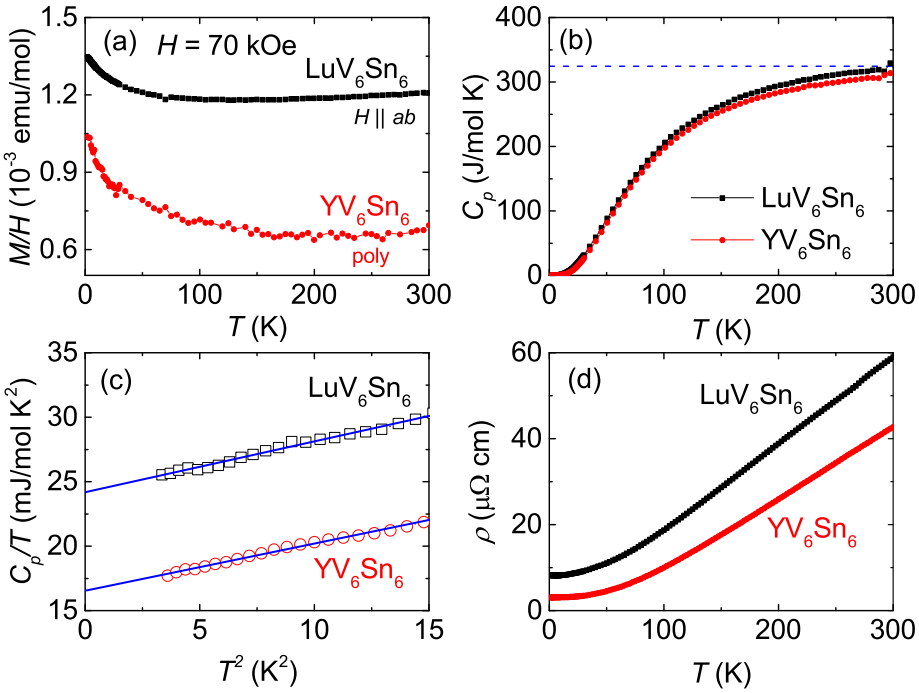

Figure 4.3: Physical property measurements of LuV_6Sn_6 and YV_6Sn_6. (a) M/H at H = 70 kOe. (b) Specific heat at $H = 0$. Horizontal line represents the Dulong-Petit limit. (c) C_p/T vs. T^2 plot for LuV_6Sn_6 at $H = 20$ kOe and YV_6Sn_6 at $H = 30$ kOe. Solid lines represent fits to $C_p(T) = \gamma T + \beta T^3$. (d) Electrical resistivity at $H = 0$.

intermetallic compounds [154, 155, 156]. For YV_6Sn_6 the absolute value of M/H at 300 K has the similar order of magnitude as previously reported values ($\sim 10^{-3}$ emu/mol) [148, 149]. Thus, the enhanced magnetic susceptibility seems to be the generic feature in non-magnetic RV_6Sn_6 compounds. From the magnetization measurements we infer that the V ions in these compounds do not carry magnetic moment. Typically, a magnetic moment on V is observed in vanadium complexes such as insulating spinel ZnV_2O_4 (V^{3+}, $S = 1$) [157] and triangular lattice antiferromagnet VCl_2 (V^{2+}, $S = 3/2$) [158]. The absence of the magnetic moment on V ions in RV_6Sn_6 implies quenching of the spin magnetic moment [159], where Sn atoms may have contributed to quenching of the spin moment on vanadium by forming metallic or covalent bonds, as evidenced by short V-Sn distances [150].

The temperature-dependent specific heat, $C_p(T)$, curves of LuV_6Sn_6 and YV_6Sn_6 are shown Fig. 4.3(b). At high temperatures the $C_p(T)$ curves of both compounds are almost identical and approach the Dulong-Petit limit at 300 K. At low temperatures, $C_p(T)$ can be described by considering electronic and phonon contributions: $C_p(T) = \gamma T + \beta T^3$. Figure 4.3(c) shows plots of C/T vs. T^2 for R = Lu at $H = 20$ kOe and R = Y at 30 kOe. Due to the superconducting transition below 4 K the specific heat data under magnetic field are used to estimate the electronic specific heat coefficient (γ) and Debye temperature (θ_D). The obtained γ values are $\sim$24 mJ/mole K^2 for R = Lu and $\sim$17 mJ/mole K^2 for R = Y.

The estimated θ_D from β is ~400 K for both compounds. Note that a rather high γ value (~67 mJ/mole K^2), obtained by fitting C/T vs. T^2 curve from 200 to 600 K^2, has been reported for YV_6Sn_6 sample [149]. The $\rho(T)$ curves for both R = Lu and Y are shown in Fig. 4.3(d). The resistivity curves decrease monotonically as temperature is lowered down to 1.8 K, following a typical metallic behavior.

4.3.4 Physical properties of RV$_6$Sn$_6$ (R = Gd - Tm)

The magnetic susceptibility of all moment bearing members in RV$_6$Sn$_6$ follows the Curie-Weiss, $\chi(T) = C/(T - \theta_p)$, behavior at high temperatures. The inverse magnetic susceptibility, $1/\chi = H/M$, curves of RV$_6$Sn$_6$ are plotted in Fig. 4.4 for both $H \parallel ab$ and $H \parallel c$ at H = 10 kOe. A polycrystalline average is estimated by $\chi_{poly} = 2/3\chi_{ab} + 1/3\chi_c$. Effective moments, μ_{eff}, and Weiss temperatures, θ_p, are obtained by fitting $1/\chi$ curves above 150 K to the Curie-Weiss law. The effective moments of RV$_6$Sn$_6$ estimated from polycrystalline average are close to that of free R^{3+}-ion values, as summarized in Table 4.1, implying a 3+ valence state of the rare-earth ions (R = Gd - Tm) and no magnetic moment on V ions. Thus, magnetic properties of RV$_6$Sn$_6$ can be explained by considering $4f$ moments of rare-earth ions. The θ_p^{poly} values obtained from polycrystalline average are negative for all rare-earths, indicating antiferromagnetic exchange interactions between rare-earth moments. For GdV$_6$Sn$_6$, μ_{eff} = 8.1 μ_B and θ_p = -0.2 K, which is consistent with that of previous polycrystalline study [148]. However, θ_p of earlier single crystal study is positive (~7.6 K) [149], which is somewhat larger than our result and other report [148]. This discrepancy may be related to different growth conditions.

The M/H curves of RV$_6$Sn$_6$, measured at H = 1 kOe for both $H \parallel ab$ and $H \parallel c$, are shown in the insets of Fig. 4.4. The M/H curves for R = Gd - Ho show slope changes below 5 K as a signature of the antiferromagnetic ordering. The magnetic ordering temperature determined from $d\chi T/dT$ is T_N = 4.8, 4.3, 2.9, and 2.3 K for R = Gd, Tb, Dy, and Ho, respectively. The magnetic ordering is not detected down to 1.8 K for R = Er and Tm.

Table 4.1: A summary of magnetic properties of RV$_6$Sn$_6$ (R = Gd - Tm): magnetic ordering temperatures T_N^{χ} determined from $d\chi T/dT$ at $H = 1$ kOe, T_N^{ρ} determined from $d\rho/dT$ at $H = 0$, $T_N^{C_m}$ determined from the maximum in C_m; easy magnetization direction direction; Weiss temperatures θ_p^{ab}, θ_p^{c}, and θ_p^{poly}; effective moment μ_{eff} (theoretical value for free R^{3+} ion); and CEF parameter B_2^0.

R	T_N^{χ}(K)	T_N^{ρ}(K)	$T_N^{C_m}$(K)	easy-direction	θ_p^{ab} (K)	θ_p^{c} (K)	θ_p^{poly} (K)	μ_{eff} (μ_B/R^{3+})	B_2^0(K)
Gd	4.8	5.0	4.9		0.9	-2.5	-0.2	8.1 (7.9)	0.2
Tb	4.3	4.2	4.2	c-axis	-38.3	32.3	-14.3	10.0 (9.7)	-1.4
Dy	2.9	2.9	3.0	c-axis	-13.4	17.0	-3.5	10.5 (10.7)	-0.4
Ho	2.3	2.3	2.4	c-axis	-4.5	4.5	-1.5	10.9 (10.6)	-0.1
Er				ab-plane	3.3	-29.9	-7.8	9.9 (9.6)	0.4
Tm				ab-plane	10.3	-71.2	-17.2	8.1 (7.6)	1.7

The magnetization isotherm, $M(H)$, at $T = 2$ K in this series clearly shows a magnetic anisotropy between $H \parallel ab$ and $H \parallel c$, as shown in Fig. 4.5. Magnetization measurements indicate no detectable hysteresis for all RV$_6$Sn$_6$. The easy magnetization direction is along the c-axis for R = Tb, Dy, and Ho and ab-plane for R = Er and Tm. As expected, $M(H)$ of GdV$_6$Sn$_6$ indicates no anisotropy at high magnetic fields, but $M(H)$ for $H \parallel c$ is slightly smaller than that for $H \parallel ab$, as displayed in the inset of Fig. 4.5(a). The saturated magnetization values of GdV$_6$Sn$_6$ and TbV$_6$Sn$_6$ at 70 kOe are close to the theoretical values of free Gd (7 μ_B/Gd) and Tb (9 μ_B/Tb) ion. $M(H)$ of GdV$_6$Sn$_6$ is similar to ones observed in previous reports [148, 149]. The saturated magnetization values for R = Dy - Tm at 70 kOe are somewhat smaller than their theoretical gJ values. The observed large magnetic anisotropy implies the presence of the strong CEF acting on $4f$-moments.

Figures 4.6(a)−(f) present the $\rho(T)$ curves of RV$_6$Sn$_6$. Note that due to the superconducting impurity phase $\rho(T)$ curves at $H = 1$ kOe for R = Gd, Tb, and Tm are plotted. At high temperatures, $\rho(T)$ follows typical metallic behavior with resistivity values ranging $10 - 100$ $\mu\Omega$ cm at 300 K. At low temperatures, $\rho(T)$ curves for R = Gd - Ho show a sharp drop at T_N due to the loss of spin disorder scattering, indicated by arrows in the insets of Fig. 4.6 (a)−(d). $\rho(T)$ of GdV$_6$Sn$_6$ and YV$_6$Sn$_6$ is similar to that of previous reports. [148, 149]

Figure 4.7(a) shows the $C_p(T)$ curves for R = Gd - Tm and Lu. The specific heat of all RV$_6$Sn$_6$ compounds reaches the value close to the Dulong-Petit limit at 300 K. At low temperatures, specific heat measurements for R = Gd - Ho show λ-like peaks (insets) as signatures of magnetic ordering, which are better seen in the magnetic part of specific heat (C_m). The magnetic ordering temperatures, determined from the peak positions, for R = Gd, Tb, Dy, and Ho are T_N = 4.9, 4.2, 3.0, and 2.4 K, respectively, which are consistent with magnetic susceptibility and resistivity measurements. For R = Er and Tm, no peak in $C_p(T)$ is observed down to 1.8 K. The low-temperature C_m curves for R = Gd - Tm are obtained by subtracting the specific heat of LuV$_6$Sn$_6$ and plotted in Figs. 4.7(b) and (c). In addition to the sharp peaks at T_N, C_m curves show broad maxima at higher temperatures. These maxima correspond to the Schottky contributions, as the R^{3+} ions (R = Tb - Tm) are influenced by the CEF. It has to be noted that C_m of GdV$_6$Sn$_6$ shows an unusual Schottky-like anomaly (a broad maximum centered around 50 K), despite CEF splitting not being expected in Gd-based compounds. This anomaly may be due to the subtraction error.

The observed magnetic ordering temperatures for RV$_6$Sn$_6$ are plotted in Fig. 4.8 as a function of de Gennes factor. Unlike RFe$_6$Ge$_6$ [132] and RMn$_6X_6$ (X = Ge and Sn) [128, 130] which have magnetic ordering temperatures above the room temperature, RV$_6$Sn$_6$ compounds indicate the magnetic ordering at much lower temperatures. When the transition metals possess no magnetic moments in this family of materials such as RCo$_6$X$_6$ (X = Ge and Sn) [140] and RCr$_6$X$_6$ [131], a relatively low magnetic ordering temperature has been

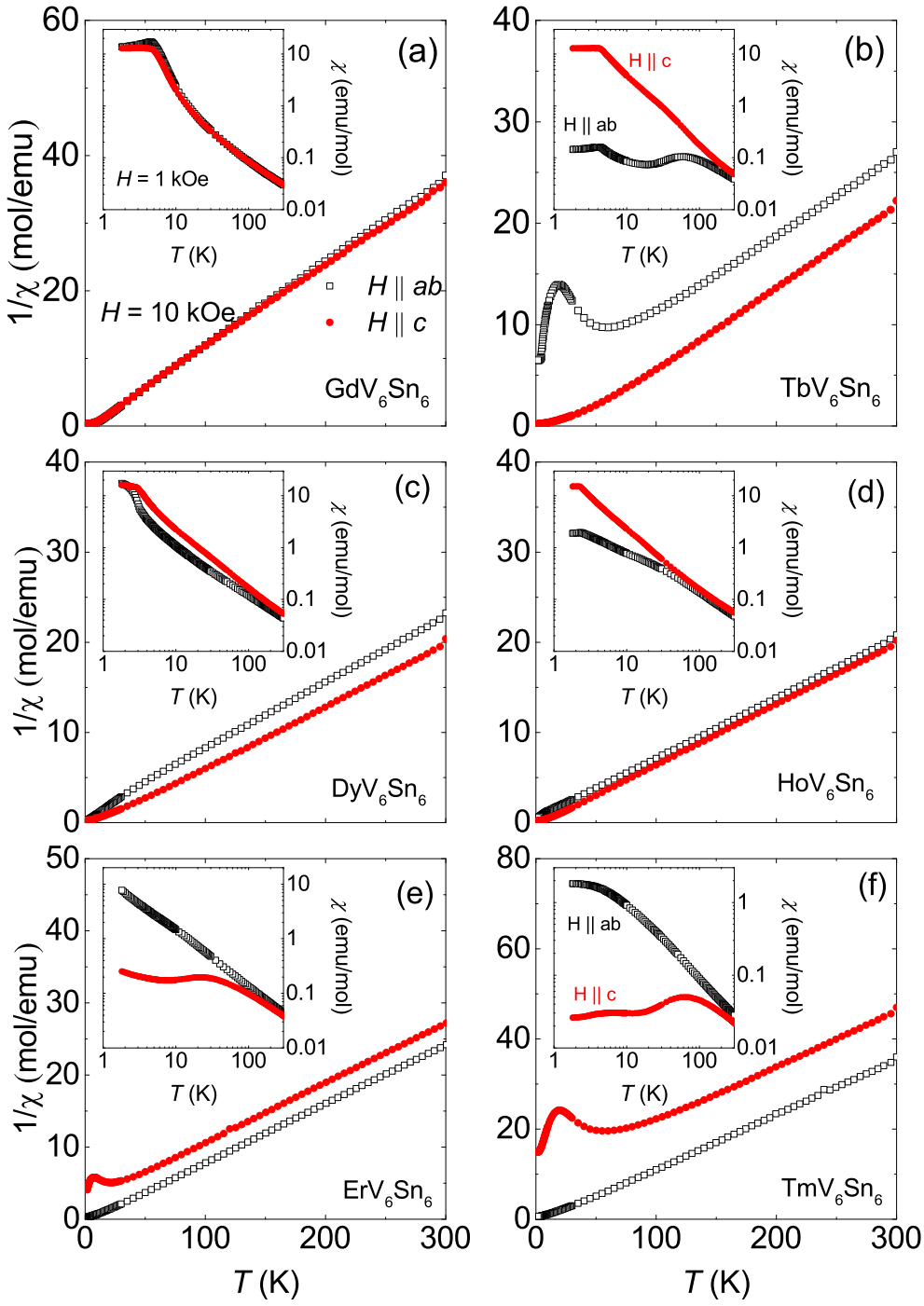

Figure 4.4: Inverse magnetic susceptibility curves of RV$_6$Sn$_6$ (R = Gd - Tm) at $H = 10$ kOe for $H \parallel ab$ (open squares) and $H \parallel c$ (closed circles). Insets show M/H curves at $H = 1$ kOe.

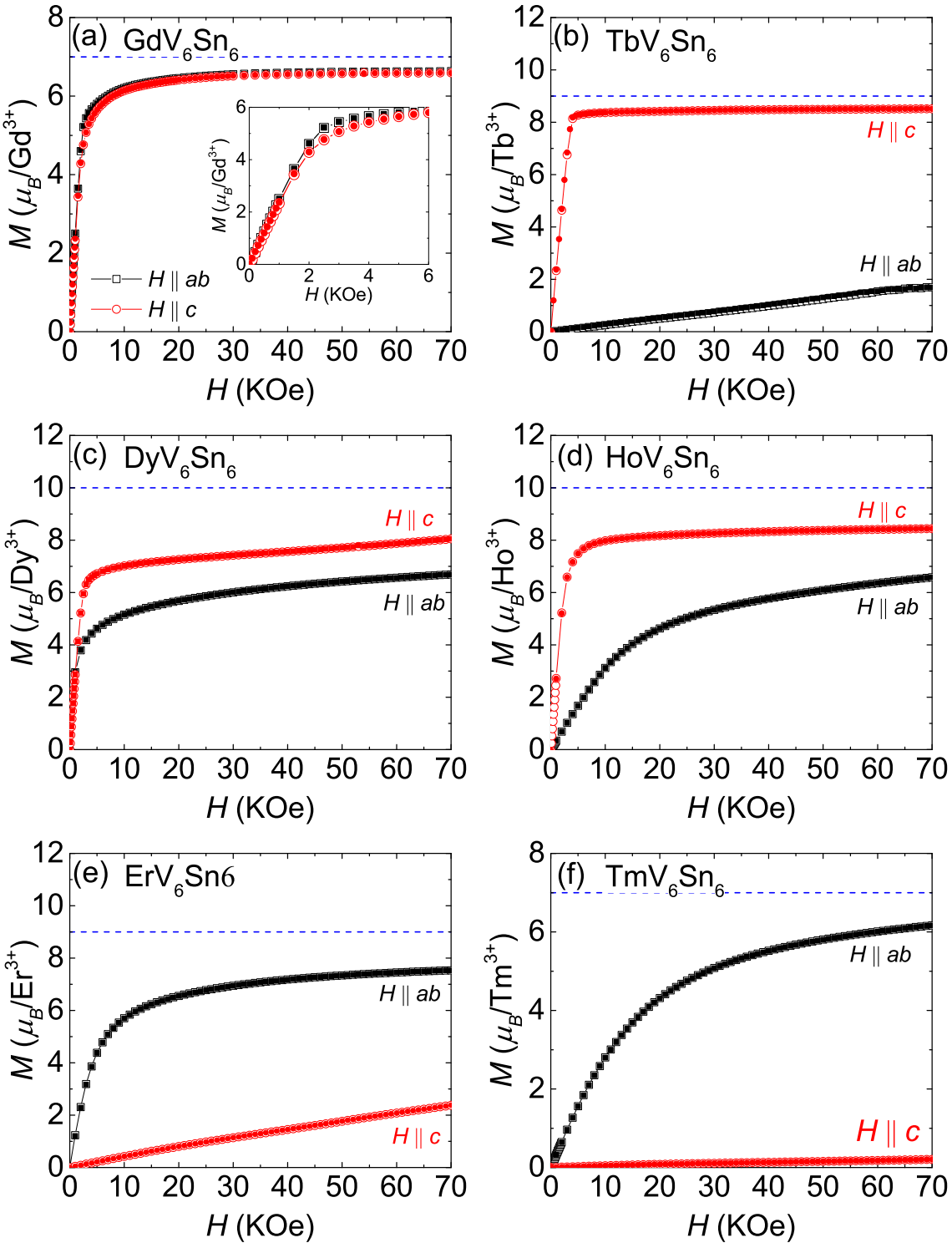

Figure 4.5: Magnetization isotherms of RV$_6$Sn$_6$ (R = Gd - Tm) at T = 2 K for $H \parallel ab$ (squares) and $H \parallel c$ (circles). Open and closed symbols are data taken while increasing and decreasing magnetic fields, respectively. Horizontal dotted lines indicate the saturated magnetization values (gJ) for free R^{3+} ions. Inset in (a) shows an expanded plot between 0 and 6 kOe.

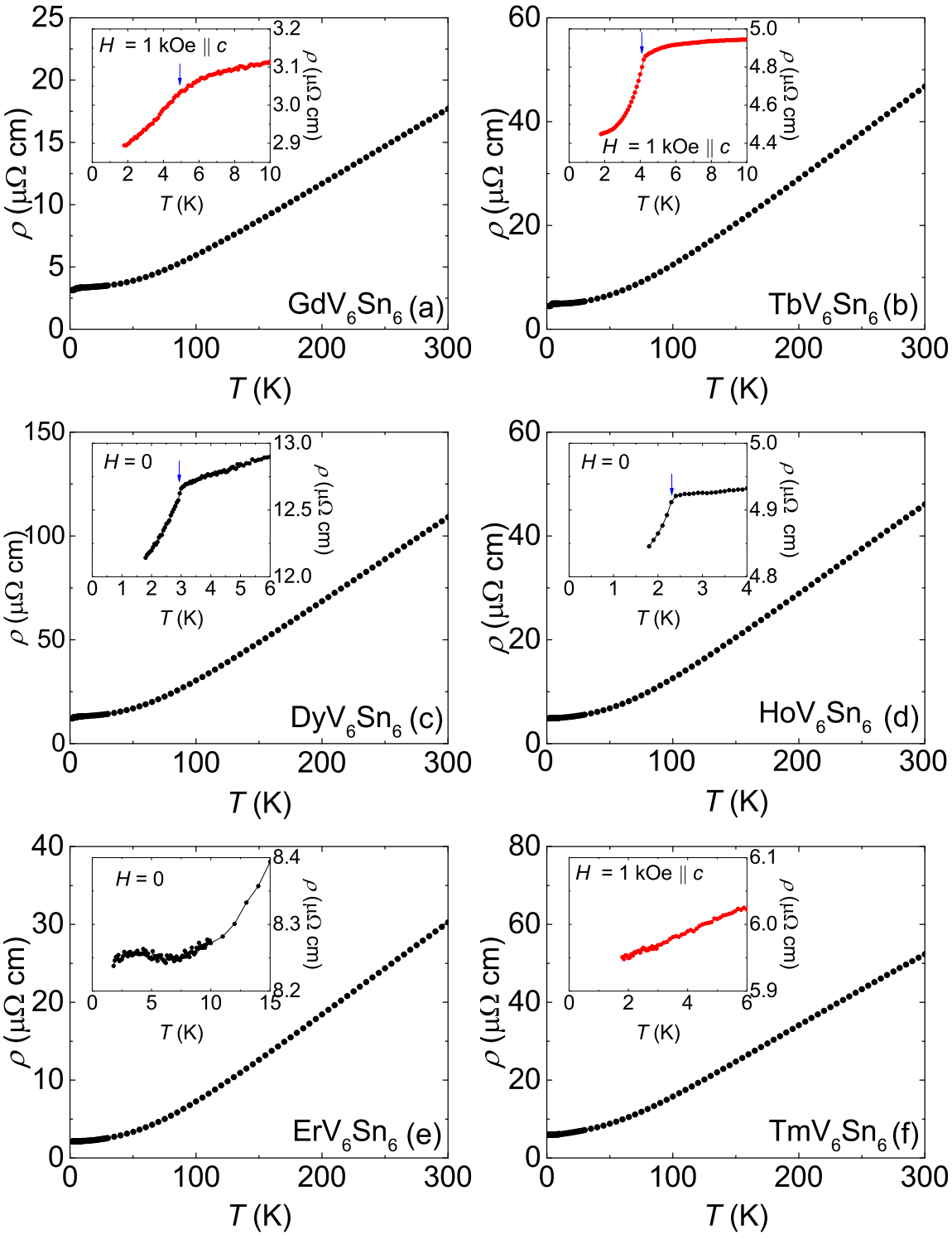

Figure 4.6: Electrical resistivity, $\rho(T)$, curves of RV$_6$Sn$_6$ (R = Gd - Tm). Insets show $\rho(T)$ at low temperatures, where vertical arrows indicate the magnetic ordering temperatures. For R = Gd, Tb, and Tm, $\rho(T)$ at H = 1 kOe is presented.

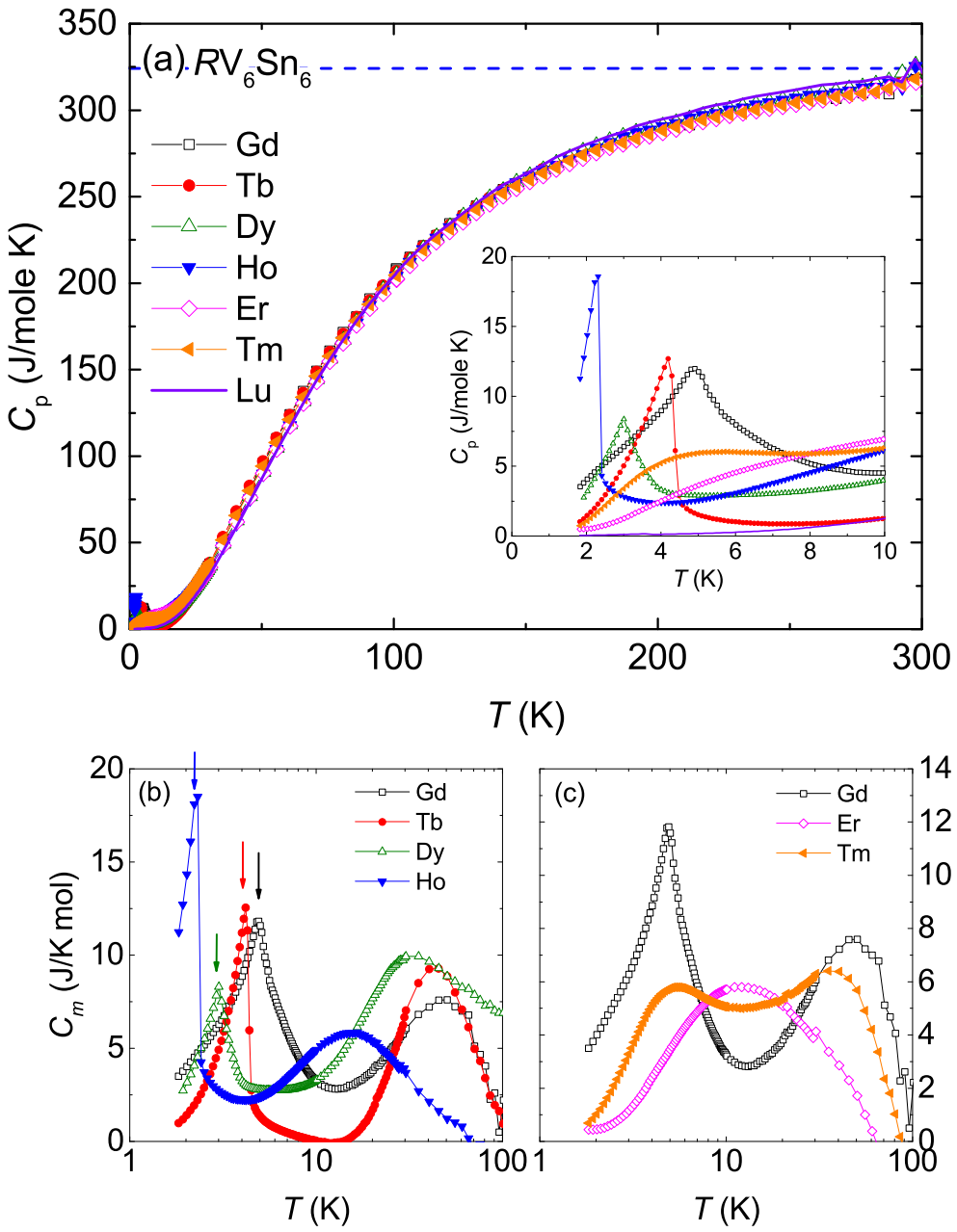

Figure 4.7: (a) Specific heat C_p curves of RV_6Sn_6 (R = Gd - Tm and Lu). The blue dashed line is the Dulong-Petit limit. Inset shows C_p below 10 K. (b) Magnetic part of the specific heat C_m for R = Gd - Ho. Vertical arrows indicate the magnetic ordering temperatures. (c) C_m for R = Gd, Er, and Tm.

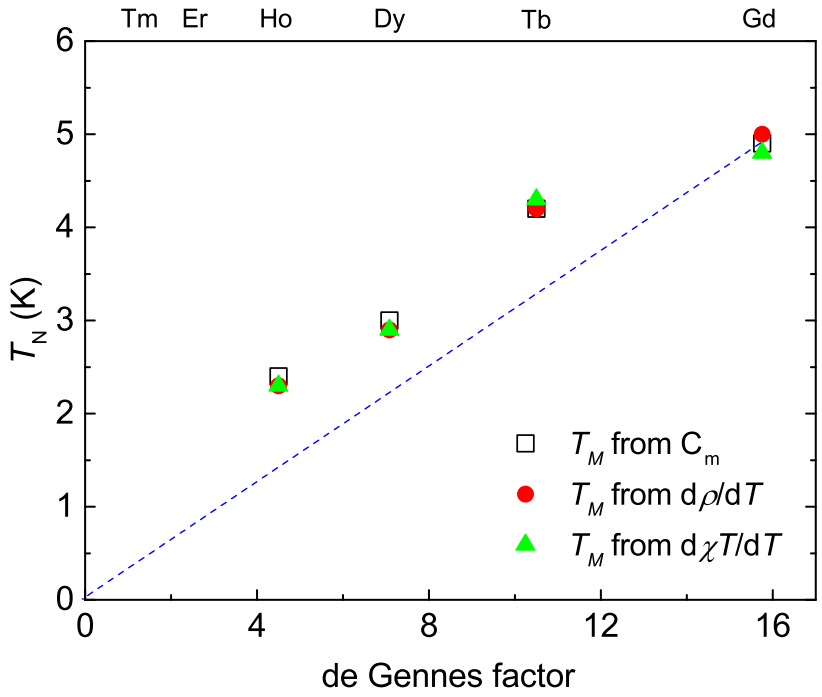

Figure 4.8: Magnetic ordering temperature, T_N, as a function of de Gennes factor. The blue dashed line represents expected ordering temperatures for R = Tb - Tm without CEF.

detected. Since the V ions possess no magnetic moments, the observed magnetic ordering is solely based on $4f$-moments, and thus a very low magnetic ordering temperature is seen.

When rare-earth ions are the only source of magnetism in an intermetallic compound, the magnetic ordering can be explained by indirect RKKY exchange interaction. In the molecular field approximation, the ordering temperature is proportional to de Gennes factor $(g_J-1)^2J(J+1)$ and can be defined as $T_N = 2/3\mathcal{J}(g_J-1)^2J(J+1)$, where $\mathcal{J}$ is the exchange parameter, g is the Landé g factor and J is the total angular momentum quantum number of Hund's rule ground state of R^{3+} ions. [18, 160] For the compounds with heavy rare-earths, T_N should decreases monotonically as R traverses from Gd to Yb. The ordering temperatures in many rare-earth-based intermetallic compounds follow this scaling [161, 162, 163, 164]. However, when there are strong CEF effects, a deviation from the linear de Gennes scaling has been observed for R = Tb - Yb [160, 165]. As shown in Fig. 4.8, the magnetic ordering temperature of RV_6Sn_6 indicates a slight deviation from the de Gennes scaling, expected to be due to the CEF effects. The observed anisotropic magnetic susceptibility and magnetization isotherm and broad maxima in specific heat clearly reflect the CEF effects on RV_6Sn_6 compounds. In addition, it has been shown a switch of easy magnetization direction from c-axis for R = Tb, Dy, and Ho to ab-plane for R = Er and Tm in many tetragonal and hexagonal rare-earth-based intermetallic compounds [160, 155, 156]. Typically, due to the change in sign of leading crystal field parameter, the switch

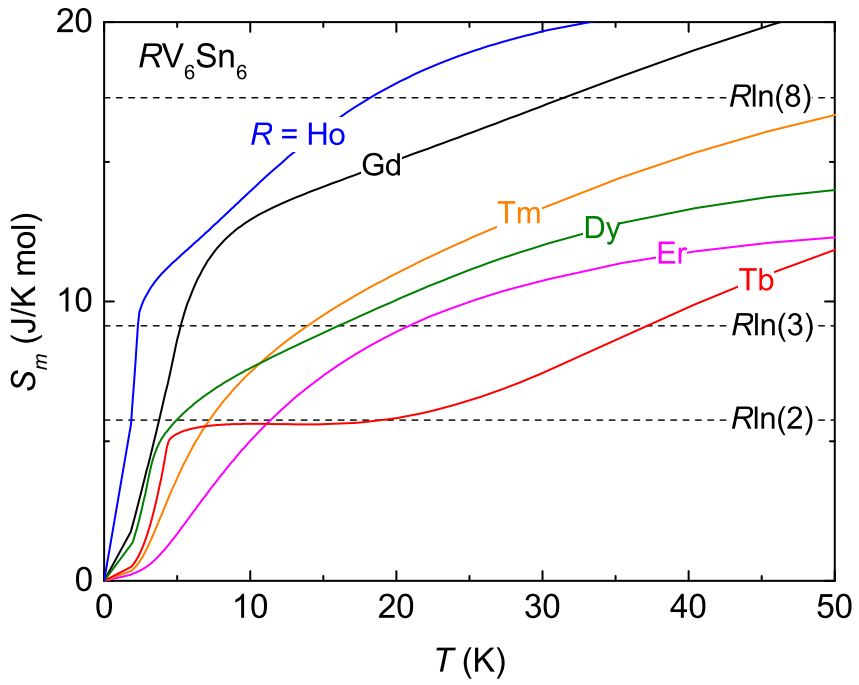

Figure 4.9: Magnetic entropy, S_m, curves of RV_6Sn_6 (R = Gd - Tm).

of easy magnetization direction occurs between Ho and Er. Based on the point charge model, the leading crystal field parameter B_2^0 in hexagonal symmetry can be obtained by $B_2^0 = \frac{10(\theta_p^{ab} - \theta_p^c)}{3(2J-1)(2J+3)}$ [11, 166]. The estimated B_2^0 values from the magnetic susceptibility results are summarized in Table 4.1. In RV_6Sn_6, the B_2^0 changes a sign between Ho and Er, suggesting that the detected magnetic anisotropy is mainly associated with CEF. When the strong CEF exchange interaction is present, the magnetic ordering temperature depends on B_2^0 and the large value of B_2^0 gives rise to enhance the magnetic ordering temperature, which breaks the simple de Gennes picture [160]. In RV_6Sn_6, although T_N for Tb - Ho is enhanced, the maximum ordering temperature occurs in GdV_6Sn_6 and T_N still follows the monotonic decrease from Gd to Ho. This implies that CEF interaction to enhance T_N for R = Tb - Ho is not large enough to exceed T_N for R = Gd [160, 167]. The B_2^0 value of TbV_6Sn_6 is greatest among c-axis ordering RV_6Sn_6 compounds, however $B_2^0 \sim -1.4$ K is much smaller than that of other rare-earth-based compounds showing the highest ordering temperature for R = Tb [160, 167].

The magnetic entropy, S_m, curves of RV_6Sn_6 are shown Fig. 4.9, where S_m is estimated by integrating C_m/T. Below 1.8 K, the missing entropy is estimated by assuming $C = 0$ at $T = 0$ K. S_m provides insight into the underlying CEF ground state of magnetic RV_6Sn_6. At T_N, S_m of TbV_6Sn_6 reaches a value close to $R\ln(2)$, suggesting a possible pseudo-doublet magnetic ground state (non-Kramers doublet, a singlet ground state with a singlet excited state). For DyV_6Sn_6, the value of S_m at T_N suggests a Kramers doublet ground state. For

HoV_6Sn_6, S_m at T_N reaches a value slightly above $R\ln(3)$, suggesting a possible triplet or pseudo-triplet ground state (a singlet ground state with either a doublet excited state or two more singlet excited states, all with close energies). Note that the ground state entropy must be properly confirmed by specific heat measurements below 1.8 K. Interestingly, only ∼50 % of the $R\ln(8)$ magnetic entropy for GdV_6Sn_6 is recovered at T_N. In general, Gd^{3+} ions in intermetallic compounds are in an $L = 0$ (S-state), no CEF effect is expected. Therefore, the full $R\ln(8)$ magnetic entropy is expected to be recovered at the ordering temperature. However, for GdV_6Sn_6 the full $R\ln(8)$ entropy is recovered at ∼30 K which is significantly higher than $T_N = 4.9$ K. Obviously the entropy is overestimated at high temperatures, where the entropy continues to increase beyond $R\ln(8)$ above 30 K, suggesting a subtraction error in the estimate of C_m. Since the obtained effective moment and saturation moment for GdV_6Sn_6 are close to the theoretical Gd^{3+} ion values, C_m is purely based on Gd magnetic contributions. When it is assumed that GdV_6Sn_6 has no additional magnetic transitions below 1.8 K, the reduced entropy at T_N cannot be simply related to the subtraction error. The reduced entropy may raise the possibility of a mixed magnetic structure, where both ordered and disordered sites coexist on an equivalent crystallographic site. This kind of magnetic structure has been evident in geometrically frustrated metallic systems [40, 41, 42]. It has also been shown theoretically and experimentally that the RKKY interaction in two dimensional hexagonal lattice gives rise to complex spin structures and potentially hosts a skyrmion phase in conjunction with geometrical frustration [168, 169, 38]. A recent study on GdV_6Sn_6 has suggested that Gd ions form noncollinear spin structure below the magnetic ordering temperature [149].

Peculiar electronic states have been observed in Fe_3Sn_2 [170, 171, 172], FeSn [173], and $Co_3Sn_2S_2$ [142], where the moment-bearing transition metals form a Kagome lattice. Recently AV_3Sb_5 (A = K, Rb Cs) systems have shown charge density wave (CDW), superconductivity, and anomalous Hall effect [174, 175, 176] all of which have opened up a new direction for exploring unconventional electronic properties associated with the non-magnetic Kagome layer. The V ions in RV_6Sn_6 possesses no magnetic moment and form the Kagome lattice. In particular, the Kagome layer in these compounds contain no other atoms in the quasi two dimensional Kagome network. Since RV_6Sn_6 (R = Gd, Y, and Sc) compounds showed non-linear Hall resistivity, topologically nontrivial band structure, and CDW [148, 149, 177], it is of great interest to check other rare-earth-based compounds (R = Tb - Tm and Lu) whether the unconventional electronic states exist in the whole family of materials.

4.4 Summary

Single crystals of RV_6Sn_6 (R = Y, Gd - Tm, Lu) are grown by Sn-flux and their physical properties are investigated by magnetization, specific heat, and resistivity measure-

ments. Powder X-ray diffraction patterns reveal that these compounds crystallize into the $HfFe_6Ge_6$-type structure, where V ions form a well isolated Kagome layer and rare-earth ions occupy on a well separated triangular lattice. Due to the CEF effects on rare-earth ions the magnetization as a function of temperature and magnetic field shows a large magnetic anisotropy, where the easy magnetization direction is c-axis for R = Tb - Ho and ab-plane for R = Er and Tm. At low temperatures, the antiferromagnetic ordering is observed below 5 K for R = Gd - Ho and no magnetic ordering is observed down to 1.8 K for R = Er and Tm. Since V ions possesses no magnetic moments, the magnetic properties of intermetallic RV_6Sn_6 compounds are solely governed by localized $4f$ electron moments.

Chapter 5

Suppression of molecular field by lattice contraction in face-centred cubic RNi$_4$Cd

5.1 Abstract

Single crystals of RNi$_4$Cd (R = Ce, Nd, Sm, and Gd−Tm) are grown by Cd flux and their physical properties are investigated by means of XRD, magnetization, electrical resistivity, and specific heat measurements. Except for R = Ce, the unit cell volume of RNi$_4$Cd follows a lanthanide contraction, implying a 3+ valence state of rare-earth ions in this series. At high temperatures, magnetic susceptibility curves for R = Nd and Gd−Tm follow the Curie-Weiss behavior. The obtained Weiss temperature (θ_p) for R = Gd−Tm is small and negative. The temperature dependence of the electrical resistivity shows a metallic behavior for all RNi$_4$Cd compounds. Thermodynamic and transport property measurements of GdNi$_4$Cd indicate an antiferromagnetic ordering below T_N = 4.5 K and the rest of the compounds show no signature of magnetic transition down to 1.8 K. The RKKY exchange mechanism is examined for its relevance to T_N and θ_p of isostructural metallic RT_4X (R = Gd−Tm) compounds. Although the variation in θ_p can be qualitatively explained by the RKKY sum, the values of θ_p in this family are highly dependent on the lattice parameter. Unlike the RCu$_4X$, the strength of the exchange interaction between molecular fields produced by rare-earth planes is strongly suppressed by the lattice contraction in RNi$_4X$ compounds.

5.2 Introduction

The RT_4X (R = rare-earth, T = Cu and Ni, and X = Cd, In, Mg, Pd, Ag, and Au) compounds adopt a MgCu$_4$Sn-type structure (F$\bar{4}$3m, No. 216), in which rare-earth atoms occupy a face-centred cubic (fcc) lattice forming a network of edge-sharing tetrahedra [178, 179, 39, 180, 181, 182, 183]. Since all three R, T, and X positions can be substituted without changing the underlying crystal structure, this family of materials is well-suited

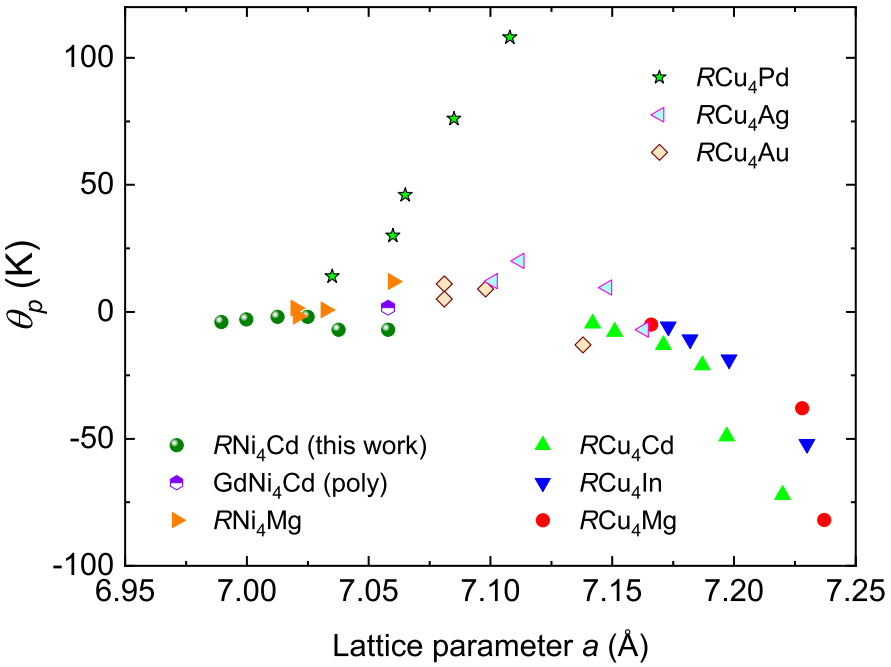

Figure 5.1: θ_p of RT_4X (R = Gd−Tm, T = Cu and Ni, and X = Cd, In, Mg, Pd, Ag, and Au) as a function of lattice parameter. Data are obtained from previous reports: GdNi$_4$Cd (polycrystalline) [178], RNi$_4$Mg [179], RCu$_4$Cd [39], RCu$_4$In [184], RCu$_4$Mg [180], RCu$_4$Pd [181], RCu$_4$Ag [182], RCu$_4$Au [183].

for studying the evolution of physical properties and their relationships through chemical substitutions. Within this family of materials, the low carrier-density semimetallic RCu$_4$In compounds exhibit large values of the magnetic frustration parameter ($f \sim 10$) which is defined as the ratio between the absolute value of the Weiss temperature $|\theta_p|$ and the magnetic ordering temperature T_N, i.e. $f = |\theta_p|/T_N$. It has been suggested that short-range superexchange interaction between rare-earths results in a low magnetic ordering temperature, giving rise to a large value of f ($T_N \ll |\theta_p|$) [184, 39]. Conversely, the good metallic RCu$_4$Cd compounds exhibit a much smaller f value [39]. When the carrier-density is increased, the frustration parameter becomes smaller ($f \sim 1$) [39]. The GdCu$_4$In$_{1-x}$Cd$_x$ system reveals a systematic change in the electrical resistivity from a semiconductor-like behavior ($x = 0$) to a metallic one ($x = 1$), resulting in an increase of T_N from 5.5 K to 38 K and θ_p from −52 K to −72 K, and thus, changing f from ~ 10 to ~ 2 [39]. In addition, replacing Cu with Ni in Gd(Cu$_{1-x}$Ni$_x$)$_4$In makes the system a good metal, changes θ_p from a large negative value to a small positive one, while maintaining T_N near 5 K [185].

The series RT_4X (R = heavy rare-earth) provides a way to compare the magnetism of highly localized $4f$ elements that share a similar crystal field environment. To gain insight into the evolution of θ_p in this series, θ_p values are plotted in Fig. 5.1 as a function of the lattice parameter for all isostructural RT_4X (R = Gd−Tm) compounds. For the

antiferromagnetic (AFM) compounds, θ_p weakly depends on the lattice parameter below 7.10 Å, while θ_p rapidly decreases above 7.15 Å toward a very large negative value. For the ferromagnetic RCu$_4$Pd compounds, θ_p deviate from this trend. The effective moment values of these compounds, obtained from magnetic susceptibility measurements, are consistent with theoretical values of free rare-earth ions, indicating a localized moment on R and no moment on T and X. The lattice parameter of GdNi$_4$Cd, obtained from the previously studied polycrystalline sample [178], locates a value near the 7.06 Å where θ_p starts to saturate close to zero as the lattice parameter decreases. When the Gd-ions are replaced by smaller rare-earths, it would be interesting to see whether θ_p of RNi$_4$Cd follows the same trend as the AFM RT_4X. Except for R = Yb and Y [186], the physical properties of RNi$_4$Cd compounds have not been previously reported. Thus, we grew single crystals of RNi$_4$Cd (R = Ce, Nd, Sm, Gd−Tm) and report their physical properties, characterized by power X-ray diffraction, magnetization, resistivity, and specific heat measurements. In particular, we compare the obtained θ_p of RNi$_4$Cd compounds with the previously reported θ_p of isostructural RT_4X (R = Gd−Tm, T = Cu and Ni, and X = Cd, In, Mg, Pd, Ag, and Au) compounds, where we attempt to qualitatively explain variations of θ_p and T_N in terms of Ruderman–Kittel–Kasuya–Yosida (RKKY) theory.

5.3 Experiments

Single crystals of RNi$_4$Cd (R = Ce, Nd, Sm, Gd−Tm) were grown by Cd flux [186]. High purity rare-earths, Ni, and Cd were loaded into an alumina crucible in the ratio of 1 : 4 : 25, and sealed into an amorphous silica tube. The ampoule was heated to 1050 °C and slowly cooled down to 750 °C at the rate of 2 °C/hr. Note that an attempt to grow single crystals for R = La and Pr was unsuccessful in this method. To verify the crystal structure of the title compound, powder X-ray diffraction (XRD) patterns of crushed single crystals were collected in a Rigaku MiniFlex diffractometer at room temperature and analyzed using a $FullProf$ software.

The analysis of powder XRD patterns confirms that RNi$_4$Cd crystallizes into the MgCu$_4$Sn-type structure (F$\bar{4}$3m, No. 216), which is an ordered variant of the AuBe$_5$-type structure [187]. The representative powder XRD patterns of DyNi$_4$Cd are shown in Fig. 5.2(a), where the open symbol and red line are observed and calculated XRD patterns, respectively. No other phases have been detected except minor Cd. In this crystal structure, Ni atoms form a network of corner-sharing tetrahedra (Wyckoff 16e-site) and leaves cavities, which are filled orderly by Cd (Wyckoff 4a-site) and R (Wyckoff 4c-site) as shown in the inset of Fig. 5.2(a) [178]. The cubic point symmetry (T_d) on rare-earth ions will make magnetic anisotropy minimal. Each Cd and R forms fcc sublattices, making a network of edge-sharing tetrahedra as shown in Fig. 5.2(c). The obtained lattice parameters (red solid circle) of RNi$_4$Cd single crystals are plotted in Fig. 5.2(b), in good agreement with previous polycrystalline sample

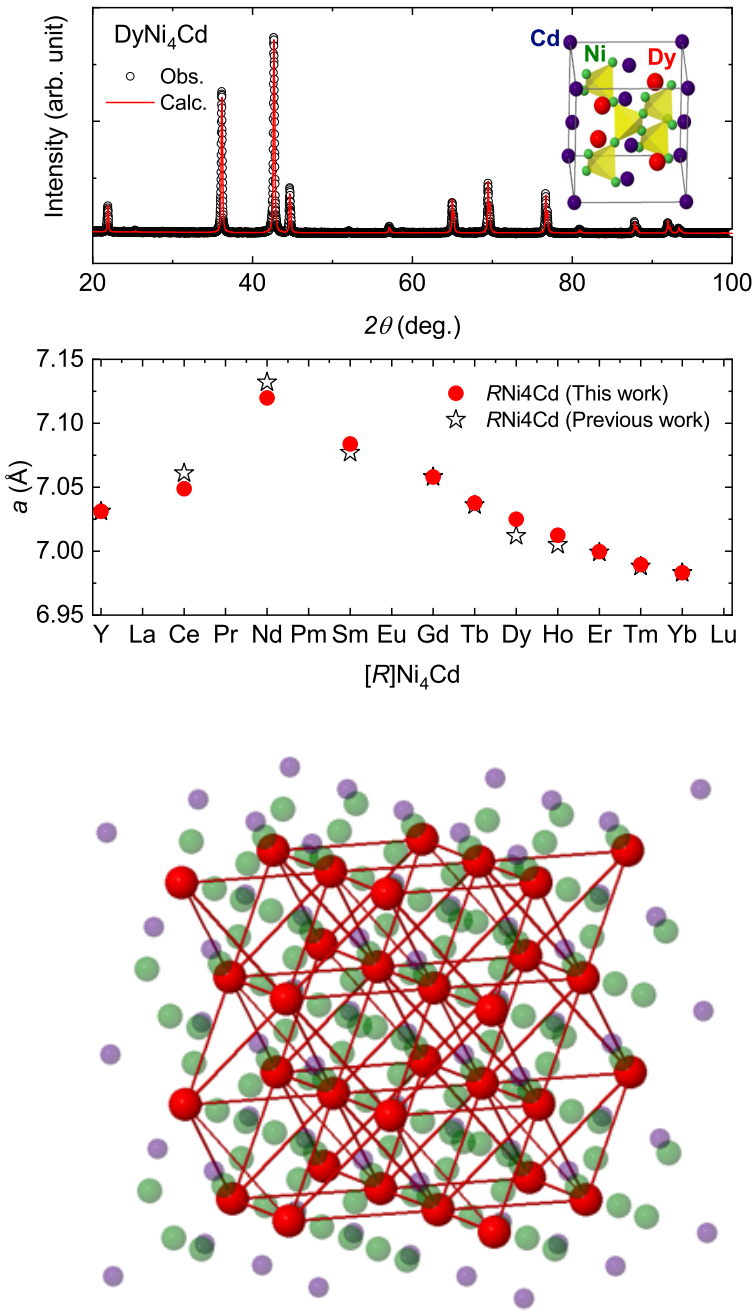

Figure 5.2: Crystallographic information about RNi$_4$Cd. Top, Middle, and bottom figures are numbered as (a), (b), and (c), respectively. (a) Observed (open symbol) and calculated (red line) powder X-ray diffraction patterns of crushed single crystals from DyNi$_4$Cd. (b) Lattice parameters of RNi$_4$Cd (R = Ce, Nd, Sm, Gd - Tm) obtained from this work (single crystals) and the previous single crystals for R = Y and Yb [186] and polycrystalline samples [178]. (c) Crystal structure of RNi$_4$Cd depicting a network of edge-sharing tetrahedra formed by rare-earth ions (red sphere).

study (open star) [178]. Except Ce, the lattice parameter of RNi$_4$Cd follows the lanthanide contraction, which indicates a 3+ valence state of rare-earth ions. For CeNi$_4$Cd a deviation from the lanthanide contraction implies a 4+ valence state of Ce ions.

All sample surfaces were polished before performing physical property measurements. dc magnetization, for temperature ranging from 1.8 K to 300 K and magnetic field up to 70 kOe applied along [111] crystallographic direction, was collected in a Quantum Design (QD) Magnetic Property Measurement System (MPMS). The standard four-probe resistivity measurements were performed from 300 K to 1.8 K in a QD Physical Property Measurement Systems (PPMS). Specific heat was measured by the relaxation method down to $T = 1.8$ K in a QD PPMS.

5.4 Results

5.4.1 Light rare-earth (R = Ce, Nd, Sm)

Figures 5.3(a) and (b) show magnetization measurements as a function of temperature and magnetic field, respectively, for R = Ce, Nd, and Sm. The magnetic susceptibility, $\chi(T) = M/H$, of CeNi$_4$Cd does not follow a Curie-Weiss (CW) law, $\chi(T) = C/(T-\theta_p)$, where $\chi(T)$ weakly depends on temperature at high temperatures. An upturn at low temperatures is probably due to magnetic impurities. The 4+ valence state of Ce ions can be clearly deduced from the deviation of CW law in magnetic susceptibility, the departure of the lanthanide contraction in lattice parameter, and the small residual magnetization at $T = 1.8$ K. For R = Nd, the inverse magnetic susceptibility, H/M, is linear in temperature above ~50 K, where the estimated effective moment, $\mu_{eff} = 4.24\ \mu_B$/Nd, is somewhat larger than the theoretical value of 3.62 μ_B/Nd. As shown in Fig. 5.3(b), the magnetization value at 1.8 K and 70 kOe is 2.3 μ_B/mole$_{Nd}$, which is smaller than the fully saturated moment value $gJ = 36/11$ probably due to the crystalline electric field effects. For R = Sm, it is well-known that the non-linearity in the plot of inverse magnetic susceptibility arises from the fact that the first excited state of the Hund's rule multiplet ($J = 7/2$) is very close to the ground state ($J = 5/2$). For this reason, the inverse magnetic susceptibility for R = Sm is fitted only at low temperatures by the modified CW formula $\chi(T) = \chi_0 + C/(T-\theta_p)$ to estimate its effective moment and θ_p. The estimated effective moment μ_{eff} ~0.95 μ_B/Sm with the Hund's rule ground state $J = 5/2$ is slightly larger than the theoretical value of 0.84 μ_B/Sm. The isothermal magnetization at 1.8 K and 70 kOe is smaller than its gJ value, as shown in Fig. 5.3(b). Electrical resistivity curves normalized at 300 K, $\rho(T)/\rho(300\ \text{K})$, of RNi$_4$Cd (R = Ce, Nd, Sm, and Y) are plotted in Fig. 5.3(c), where the resistivity curves indicate a metallic behavior. The low-temperature specific heat of RNi$_4$Cd (R = Ce, Nd, and Y) clearly confirms no phase transitions in these compounds as shown in Fig. 5.3(d). The electrical resistivity and specific heat of YNi$_4$Cd are consistent with the earlier report [186].

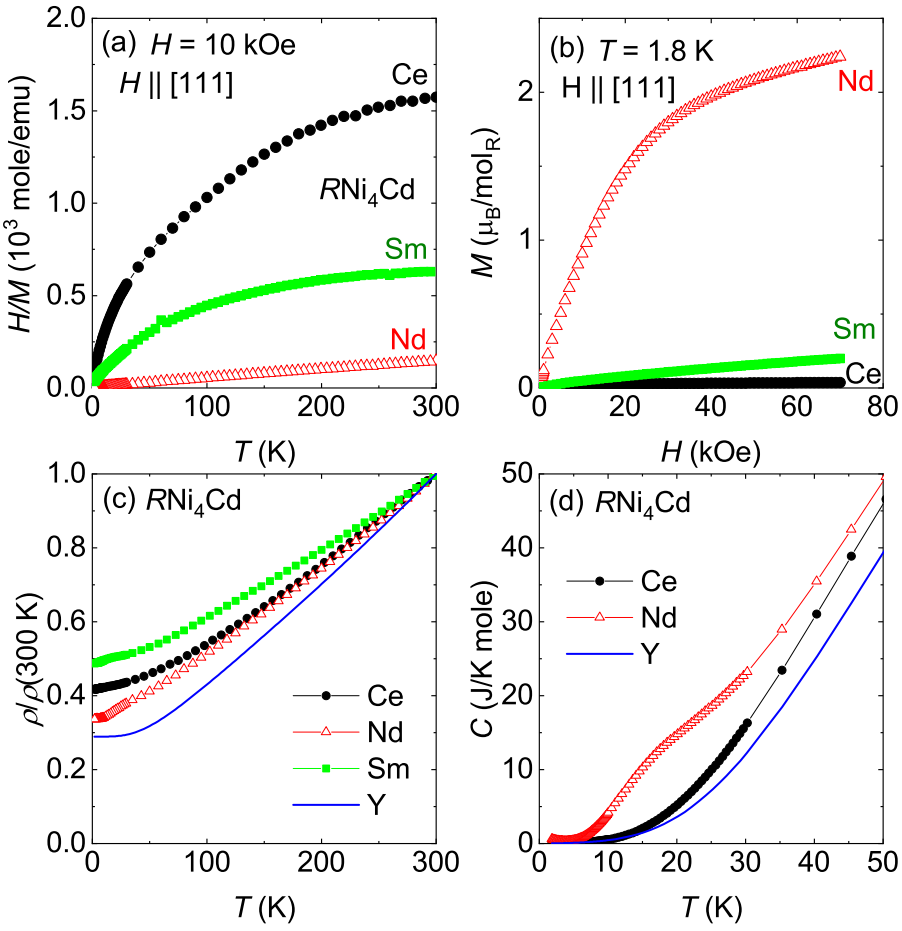

Figure 5.3: Magnetization measurements of RNi$_4$Cd for R = Ce, Nd, and Sm. (a) Inverse magnetic susceptibility at H = 10 kOe. (b) Isothermal magnetization at T = 1.8 K. (c) ρ/ρ(300 K) vs. T. (d) Specific heat at low temperatures.

Table 5.1: A summary of magnetic properties of RNi$_4$Cd obtained from magnetic susceptibility measurements. $\boldsymbol{M}$**(7 T)**: absolute value of magnetization in μ_B/R at $H = 7$ T and $T = 1.8$ K. $\boldsymbol{\mu_{eff}}$: effective moment in μ_B/R obtained from Curie-Weiss CW fit or modified Curie-Weiss (MCW) fit. Value inside the parenthesis is the theoretical value for trivalent R. $\boldsymbol{\Theta_p}$: paramagnetic Curie-Weiss temperature in K, $\boldsymbol{T_N}$: magnetic ordering temperature in K. Blank data means no magnetic ordering down to 1.8 K.

R	M(70 kOe)	μ_{eff}	Θ_p	T_N	Fit method
Ce	0.04 (2.1)	N/A (2.54)	N/A		N/A
Nd	2.24 (3.2)	4.24 (3.62)	-27		CW
Sm	0.20 (0.7)	0.95 (0.84)	3		MCW
Gd	6.76 (7)	7.93 (7.94)	-7	4.5	CW
Tb	8.39 (9)	10.17 (9.72)	-7		CW
Dy	9.39 (10)	10.63 (10.63)	-2		CW
Ho	8.34 (10)	9.66 (10.60)	-2		CW
Er	8.34 (9)	9.75 (9.59)	-3		CW
Tm	5.38 (7)	7.71 (7.51)	-4		CW

5.4.2 Heavy rare-earth (R = Gd−Tm)

The H/M curves of RNi$_4$Cd (R = Gd−Tm), measured at $H = 10$ kOe along $H \parallel [111]$, are plotted in Fig. 5.4(a). In contrast to the light rare-earth compounds, H/M curves of heavy rare-earth compounds follow the Curie-Weiss behavior at high temperatures. Thus, μ_{eff} and θ_p are estimated by fitting the curves with the CW formula from 150 K to 300 K. The obtained results are summarized in Tab. 5.1. The values of μ_{eff} are found to be consistent with that of respective trivalent rare-earth ions. The small and negative values of θ_p suggest a weak antiferromagnetic nature of the exchange interaction between rare-earth ions, and deviate from the de Gennes factor (dG) scaling [18]. At low temperatures, only GdNi$_4$Cd shows a peak at 4.5 K in the magnetic susceptibility as a signature of magnetic ordering. For the rest of rare-earths, the magnetic susceptibility measurement at $H = 1$ kOe indicate no magnetic transition down to 1.8 K. Note that YbNi$_4$Cd undergoes an antiferromagnetic ordering below $T_N = 0.97$ K [186]. The isothermal magnetization for R = Gd−Tm, plotted in Fig. 5.4(b), linearly increases with the field and indicates a tendency to saturate above 20 kOe. The magnetization values at 70 kOe are somewhat smaller than the theoretical gJ values.

The electrical resistivity, $\rho(T)$ curves, normalized at 300 K for R = Gd−Tm are plotted in Fig. 5.5. $\rho(T)$ for all compounds follows a typical metallic behavior. The absolute value of the resistivity at 300 K is shown in the inset. Note that the absolute resistivity value of RNi$_4$Cd is similar to that of RCu$_4$Cd [39].

The temperature dependence of the specific heat, C_p, curves for R = Gd−Tm and Y are shown in Fig. 5.6. Among RNi$_4$Cd compounds, only GdNi$_4$Cd shows a clear λ-like peak at

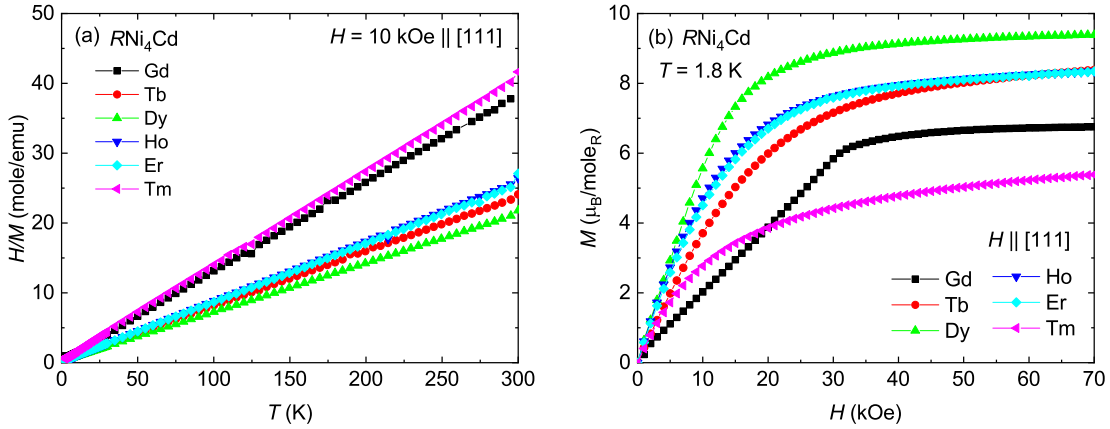

Figure 5.4: Magnetic properties of RNi$_4$Cd for R = Gd−Tm. (a) Inverse magnetic susceptibility at H = 10 kOe. (b) Isothermal magnetization at T = 1.8 K.

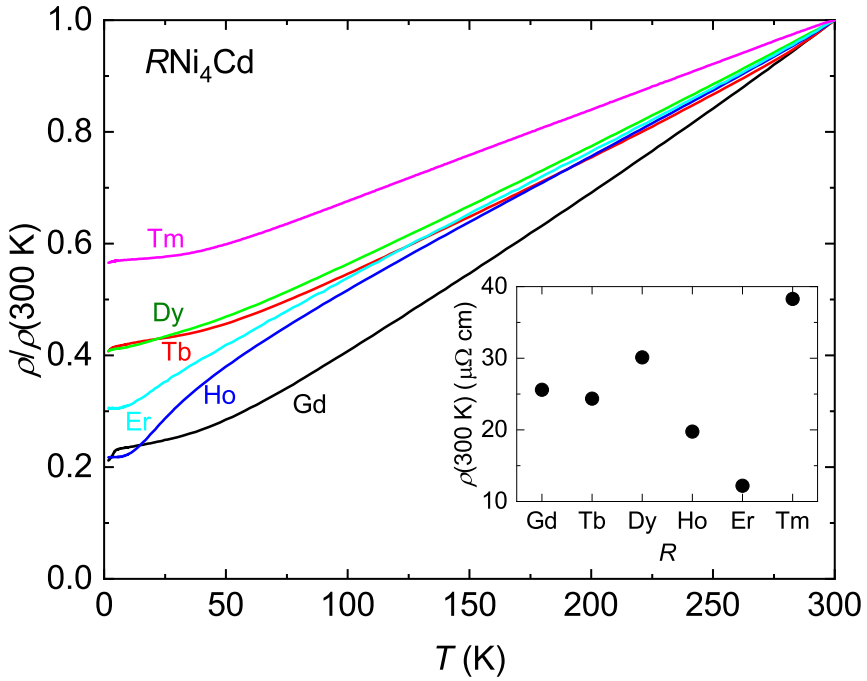

Figure 5.5: Normalized ρ/ρ(300 K) of RNi$_4$Cd at H = 0 kOe. Inset presents the absolute values of their room temperature resistivity.

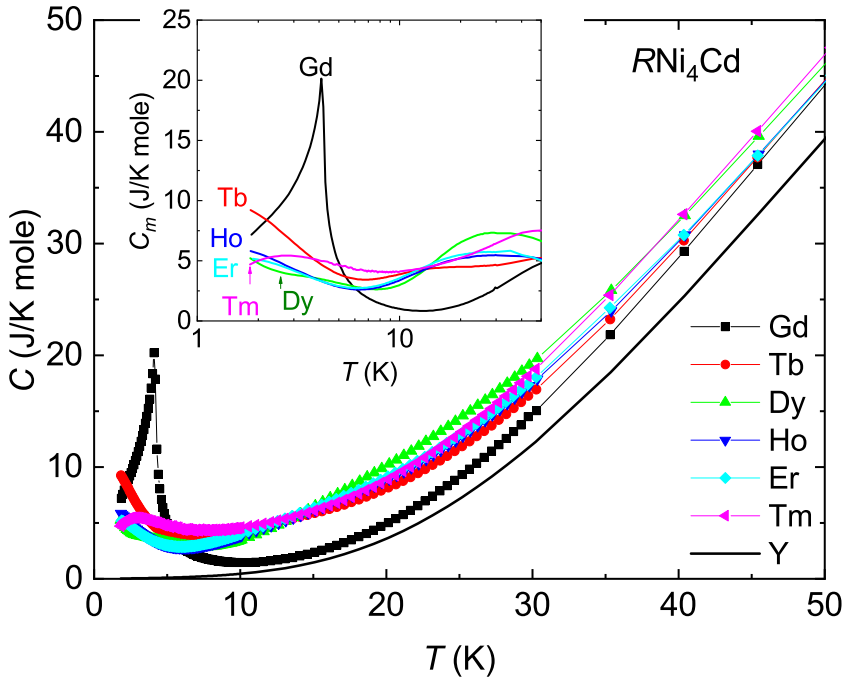

Figure 5.6: Specific heat of RNi$_4$Cd at low temperatures. The inset shows magnetic specific heat.

4.5 K, which is the onset of the antiferromagnetic ordering. C_p for R = Tb−Er indicates an upturn at low temperatures, where the rise in specific heat as temperature decreases may suggest a possible magnetic ordering below 1.8 K. It is necessary to measure specific heat below 1.8 K to confirm whether magnetic ordering exists. The specific heat for R = Tm shows a broad maximum around 3 K (better seen in the inset), which can be related to a Schottky anomaly due to low-lying CEF levels. The magnetic part of the specific heat (C_m) of RNi$_4$Cd (R = Gd−Tm) is estimated by subtracting the specific heat of YNi$_4$Cd and is plotted in the inset of Fig. 5.6. The C_m curves for R = Tb−Tm indicate broad maxima at high temperatures, which correspond to the Schottky contributions, as the R^{3+} ions are influenced by the CEF.

5.4.3 GdNi$_4$Cd

Since GdNi$_4$Cd indicates the magnetic ordering at 4.5 K, the magnetic properties of this compound are further investigated. M/H of GdNi$_4$Cd at H = 1 kOe shows a peak at 4.1 K and a hump near $T \sim$ 3.0 K, as shown in Fig. 5.7(a). The resistivity in zero field is also plotted in Fig. 5.7(a), showing a sharp drop below 4.5 K probably due to the loss of spin-disorder scattering. The observed ordering temperature in our single crystal sample is consistent with the previously reported polycrystalline sample study [178]. However, a

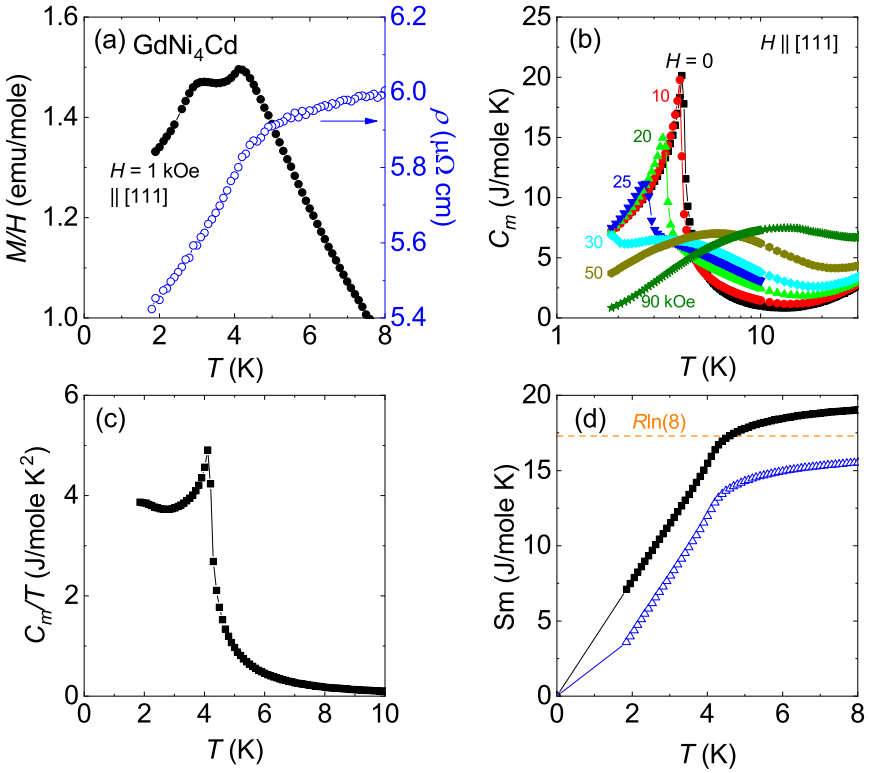

Figure 5.7: Low-temperature magnetic susceptibility, specific heat, and resistivity of $GdNi_4Cd$. (a) Magnetic susceptibility at $H = 1$ kOe (left axis) and resistivity in zero field (right axis). (b) Magnetic specific heat at various magnetic fields. (c) C_m/T vs. T. d) Estimated S_m. See details in the text.

ferromagnetic ordering at $T \sim 32$ K observed in the previous polycrystalline sample due to the binary $GdNi_5$ inclusion [178] is not detected in our single crystal sample.

The magnetic specific heat C_m in zero field also shows a clear λ-like transition at 4.5 K, as shown in Fig. 5.7(b). The magnetic ordering can be suppressed below 1.8 K by an external magnetic field less than ~50 kOe. A broad maximum in C_m is developed at $T \sim 3.5$ K at $H = 30$ kOe and this maximum moves to higher temperatures as magnetic field increases, which is probably due to the Zeeman splitting of $S = 7/2$ energy level. The magnetic specific heat divided by temperature, C_m/T, is plotted in Fig. 5.7(c). C_m/T does not go to zero below the magnetic ordering temperature, showing a slight upturn below 2.7 K. The upturn in C_m/T typically occurs in Gd-based compounds arising from the broken degeneracy of Gd ground state below the magnetic ordering temperature [188]. It should be noted that a nuclear Schottky anomaly is observed near $T = 0.25$ K in $HoCu_4In$ and $HoCu_4Cd$ [42]. We believe that the upturn just below T_N in our C_m/T of $GdNi_4Cd$ is not originated from the nuclear spin, but the contribution from the Schottky anomaly arising from broken degeneracy of the ground state J. Since C_m/T does not go to zero, the magnetic entropy (S_m) is estimated by two scenario. First, C_m/T below 1.8 K is linearly extrapolated to zero with the value of 3.8 J/mole K^2, which may reflect the upper limit of S_m. S_m in this limit (solid symbols) almost reaches the full $R\ln(8)$ entropy at T_N, as shown in Fig. 5.7(d). Second, C_p must be zero at zero temperature, thus we assume $C_m/T = 0$ at 0 K, which can be considered as the lower limit (underestimate of the magnetic entropy). The estimated S_m in this limit (open symbol) recovers 70 % of $R\ln(8)$ by T_N. It has been observed in this family of material that S_m value at T_N is 86 % of $R\ln(8)$ for $GdCu_4Cd$ [39] and 67 % of $R\ln(8)$ for $GdCu_4In$ [40]. In addition, the neutron diffraction experiments have revealed that Ho moments in $HoCu_4Cd$ are fully ordered [42] and Gd moments in $GdCu_4In$ are partially ordered [40]. It is expected that the similar S_m value of $GdNi_4Cd$ with that of $GdCu_4Cd$ may indicate that Gd moments in $GdNi_4Cd$ is also fully ordered without magnetic frustration. It has to be noted that the zero field C_m of $GdNi_4Cd$ shows an unusual Schottky-like anomaly above T_N, despite CEF splitting not being expected in Gd-based compounds. The full recovery of $R\ln(8)$ entropy at T_N for $GdNi_4Cd$ suggests that the broad feature above 10 K observed in C_m is due to the subtraction error.

5.5 Discussion

The RKKY exchange mechanism is examined for its relevance to T_N and θ_p of RT_4X compounds. In this family, the $4f$-moments of heavy rare-earths are well respected with their Hund's rule ground state J values, and their magnetic susceptibility curves are weakly affected by crystalline electric field (CEF) effects due to the small energy level splittings. In general, the strength of the molecular field λ can be estimated from θ_p value. When θ_p is positive, it indicates ferromagnetic (FM) interactions, while negative values indicate antifer-

romagnetic (AFM) interactions [189, 190]. The magnetic ordering temperature (T_m) reflects the exchange energy, which depends on the arrangement of magnetic moments on the lattice and the types of exchange interactions such as superexchange and RKKY interactions. In highly localized $4f$ moment materials, it is often observed that $T_c \sim \theta_p$ for ferromagnets and $T_N < \theta_p$ for antiferromagnets, due to the simplified molecular field interactions. In some cases, T_N can be further reduced by geometrically frustrated lattice structures such as fcc, Kagome, and pyrochlore. Comparing θ_p in this family can provide valuable insights into the relative strength of exchange interactions and the dominant parameters affecting the magnitude of both θ_p and T_m in isostructural settings. In particular, Gd-based compounds are suitable for this analysis because of $L = 0$ state.

For GdT_4X compounds, we investigate a correlation between the electrical resistivity at 300 K, ρ(300K), and other parameters such as the lattice parameter, T_N, and θ_p. ρ(300 K) for metallic GdT_4X compounds is plotted in Fig. 5.8(a) against their lattice parameter. Note that GdCu$_4$In is not plotted in the figure, where the resistivity value of the semimetallic RCu$_4$In series is much larger than that of other metallic compounds in this family [39]. As the lattice parameter increases, the value of ρ(300 K) increases. This relationship has been observed in the RCu$_4$In and RCu$_4$Cd series, where a larger R results in a significant increase in resistivity values [195, 39]. However, when R is varied from Gd to Tm in the RNi$_4$Cd series, the resistivity value at 300 K does not show a significant change (Fig. 5.5), despite the series exhibiting a similar degree of lattice contraction.

In a simple model, the electrical resistivity value is inversely proportional to the carrier-density n which is proportional to the density of states $N(E_F)$ at the Fermi level. Therefore, variations of ρ(300 K) can be used as an approximation for the relative change in $N(E_F)$ within this family of materials. Among this group, GdNi$_4$Cd exhibits the smallest resistivity value at 300 K, ρ(300 K) $\sim$ 25 $\mu\Omega$ cm, implying the largest $N(E_F)$. This result is supported by the observed values of electronic specific heat coefficient γ and susceptibility χ_0 in non-magnetic compounds, as γ and χ_0 values are proportional to $N(E_F)$. The γ and χ_0 values are 14 mJ/mol K^2 and 1×10^{-3} emu/mol for YNi$_4$Cd [186] and 2.91 mJ/mol K^2 [39] and 2.7×10^{-5} emu/mol [196] for LuCu$_4$In, respectively. To best our knowledge, YNi$_4$Cd has the highest χ_0 value among previously reported non-magnetic RT_4X compounds. Thus, YNi$_4$Cd is considered a good metal with ρ(300 K) $\sim$ 10 $\mu\Omega$ cm, while LuCu$_4$In is a low-carrier-density semimetal with a very large ρ(300 K) $\sim$ 1000 $\mu\Omega$ cm.

The T_N and θ_p values of metallic GdT_4X compounds are displayed in Figs. 5.8(b) and (c), respectively, as a function of ρ(300 K). It appears that both T_N and θ_p are approximately proportional to ρ(300 K). For metallic GdT_4X, the frustration parameter ranges $0.5 < f < 2$ as shown in Fig. 5.8(d). Compounds with large $|\theta_p|$, such as GdCu$_4$Cd and GdCu$_4$Mg, tend to have a frustration parameter between 1 and 2, while compounds with small $|\theta_p|$, such as GdNi$_4$Cd, GdNi$_4$In, and GdCu$_4$Ag, tend to have a frustration parameter less than 1. The observed f suggests a variation in the strength of the RKKY interaction between the

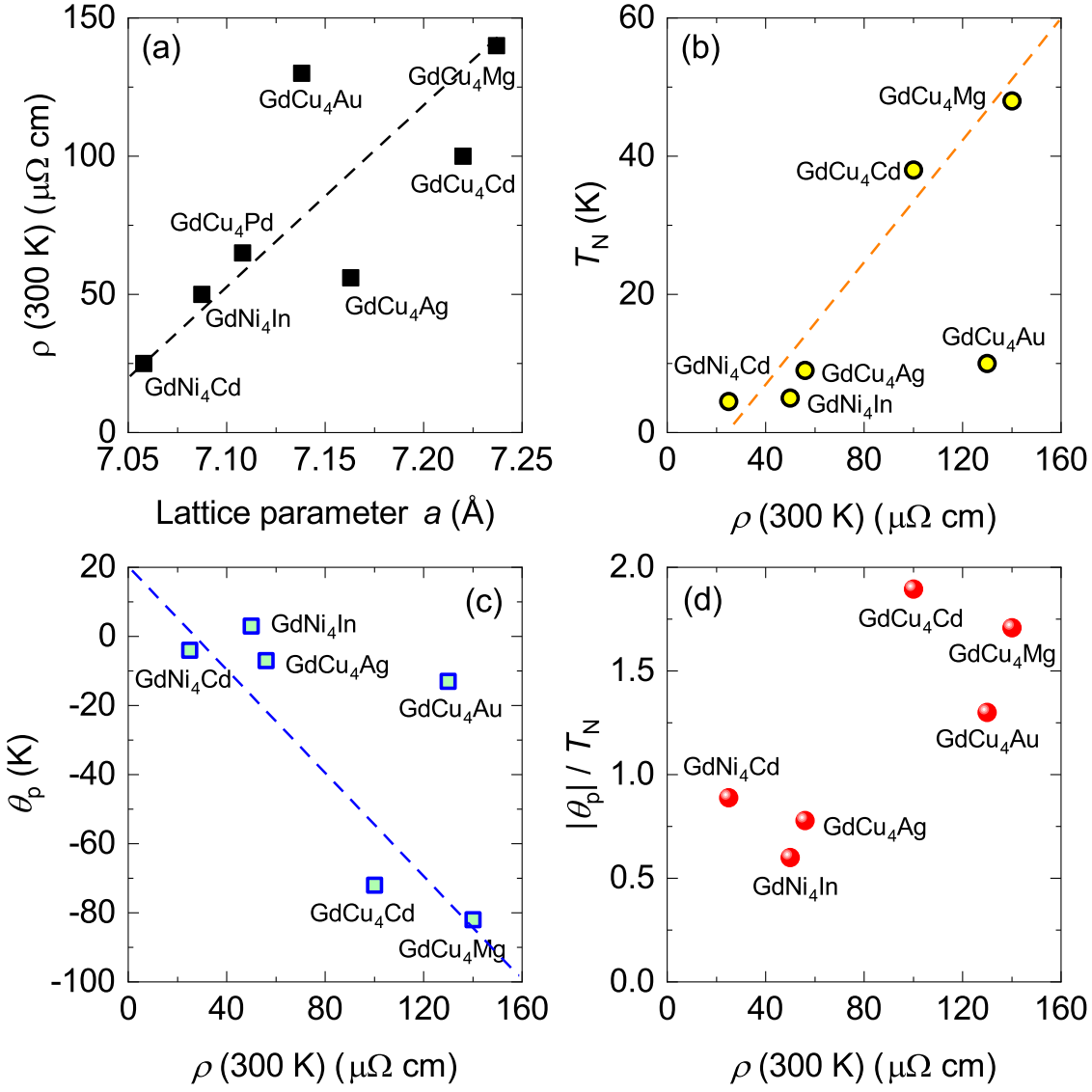

Figure 5.8: Relationship between lattice parameter, $\rho(300\ \mathrm{K})$, T_N, and θ_p in metallic GdT_4X. (a) $\rho(300\ \mathrm{K})$ vs. lattice parameter. (b) T_N vs. $\rho(300\ \mathrm{K})$. (c) θ_p vs. $\rho(300\ \mathrm{K})$. (d) $|\theta_p|/T_N$ vs. $\rho(300\ \mathrm{K})$. Since $\rho(300\ \mathrm{K})$ data for some Gd-based compounds are not available, $\rho(300\ \mathrm{K})$ is inferred from its analogous compound that differs by only R. Data source for $\rho(300\ \mathrm{K})$ are $GdNi_4Cd$ (this work), $GdNi_4In$ ($\rho(300\ \mathrm{K})$ averaged from $YbNi_4In$ and $NdNi_4In$ [191]), $GdCu_4Cd$ [39], $GdCu_4In$ [39], $GdCu_4Mg$ ($\rho(300\ \mathrm{K})$ from $SmCu_4Mg$ [180]), $GdCu_4Pd$ [192], $GdCu_4Ag$ ($\rho(300\ \mathrm{K})$ from $NdCu_4Ag$ [193]), $GdCu_4Au$ [194]. T_N and θ_p data are obtained from this work and previous reports: $GdNi_4Cd$ (this work), $GdNi_4Mg$ [179], $GdCu_4Mg$ [180], $GdCu_4Pd$ [181], $GdCu_4Ag$ [182], $GdCu_4Au$ [183], $GdCu_4(In_{1-x}Cd_x)$ [39], $Gd(Cu_{1-x}Ni_x)_4In$ [185].

various Gd-Gd pairs responsible for T_N and θ_p. It seems that the lattice parameter plays a significant role in tuning $N(E_F)$ and T_N and θ_p for metallic GdT_4X compounds.

It has been generally considered that the magnetic ordering temperature of $4f$-based metallic systems is proportional to the square of effective exchange interaction (j_{sf}^2) and $N(E_F)$ [39]: $T_N \propto j_{sf}^2 N(E_F)$. However, the metallic GdT_4X compounds seem to follow the opposite direction where the larger $N(E_F)$ does not necessarily enhance the T_N. According to Ref. [197], the variation and sign change of θ_p in Gd-based compounds can be explained by the RKKY mechanism. In the RKKY picture [12, 13, 14, 18], θ_p for both AFM and FM interactions can be expressed by

$$\theta_p = \frac{2(g-1)^2 J(J+1)\mathcal{J}(\mathbf{Q}=0)}{3k_B}, \tag{5.1}$$

$$\mathcal{J}(\mathbf{Q}=0) = -\frac{9\pi n_0^2}{4k_B E_F} j_{sf}^2 \sum_i F(2k_F R_i), \tag{5.2}$$

where $\mathcal{J}(\mathbf{Q})$ is the effective exchange interaction between f-electron spins mediated by conduction electrons, $(g-1)^2J(J+1)$ is the de Gennes factor (dG) for the angular momentum quantum number J, and n_0 is the average number of conduction electrons per unit cell. The RKKY sum varies between positive and negative values depending on a dimensionless quantity $k_F R_i$, leading to sign changes in θ_p. Hence, the observed behavior can be explained by considering the position and direction of the RKKY sum, where the increment of $k_F R_i$ leads to either an approach to or a departure from zero of RKKY sum.

For RCu$_4X$ (X = Cd, In, Pd, Ag, and Au), the RKKY sum has been calculated by assuming R and Cu atoms contribute three and one electron to the conduction band, respectively [182, 198, 39, 197]. When the magnitude of θ_p is large, this picture qualitatively explains the variation of θ_p, where the observed θ_p linearly scales with dG. However, when the θ_p value is small and locates near a sign change in the RKKY sum, the dG scaling breaks down as shown for the cases of RCu$_4X$ (X = Ag and Au) and RNi$_4$Cd. For RCu$_4X$ (X = Ag and Au), θ_p even shows a sign change when R is varied from Gd (dG = 15.8) to Tm (dG = 1.2), which should not occur in the conventional RKKY mechanism. Therefore, constant conduction electrons or exchange interactions j_{sf} upon isoelectric substitution, assumed in the simple RKKY interaction, cannot be applied to real materials, where proper band structures must be considered to evaluate $\mathcal{J}(\mathbf{Q})$.

The observed θ_p values of isostructural GdT_4X compounds are strongly dependent on the lattice parameter, implying a correlation with the interatomic spacing between the Gd ions. This relationship is demonstrated in Fig. 5.9, which plots θ_p values as a function of their lattice parameters. As seen in the figure, a decrease in the lattice parameter (i.e. a shorter Gd-Gd distance) leads to a shift of θ_p value toward a positive direction. Note for other rare-earth elements (R = Tb−Tm) that the lattice parameter of RT_4X closely follows

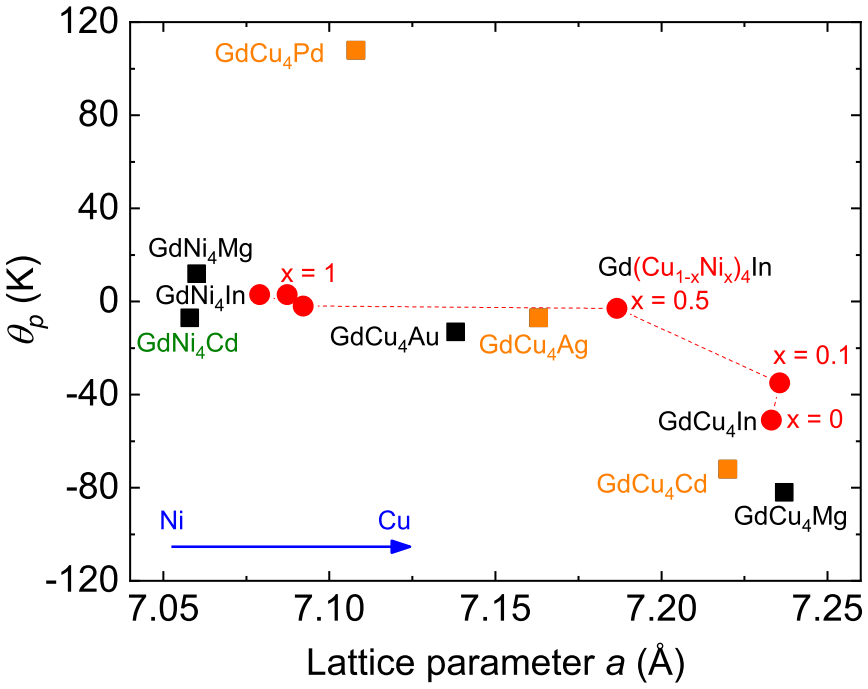

Figure 5.9: θ_p as a function of lattice parameter. θ_p data are obtained from this work and previous reports: $GdNi_4Cd$ (this work), $GdCu_4Cd$ [39], $GdNi_4Mg$ [179], $Gd(Cu_{1-x}Ni_x)_4In$ [185], $GdCu_4Mg$ [180], $GdCu_4Pd$ [181], $GdCu_4Ag$ [182], $GdCu_4Au$ [183].

the trend of the lanthanide contraction, regardless of R, T, and X, and θ_p indicates a similar trend as shown in Fig. 5.1.

We observe that the substitution of T and X in GdT_4X has two main effects: i) a lattice effect due to the substitution of ions with different ionic sizes and ii) an electronic effect due to the substitution of ions with different valence electrons [199]. Although the complete band structures are necessary to know the exact relationship between these two factors, we infer the dominant effect for given substitutions from the experimental observations. Figure 5.8(a) suggests that the lattice contraction has a tendency to increase k_F, as $\rho(300K)$ is proportional to $1/N(E_F) \propto 1/k_F$. For isoelectric substitution of Ag with Au in $GdCu_4X$, change in θ_p is small due to the small lattice contraction. Similarly, substituting Cd with Mg in $GdCu_4X$ results in insignificant variations of θ_p, possibly due to the negligible increase in $N(E_F)$ resulting from the small lattice expansion.

For Cd→Ag→Pd substitution, both the lattice and electronic effects are needed to be considered. Since the exact number of valence electrons contributing to the conduction band is unknown, we simply consider the electronic configurations of X atoms in $GdCu_4X$ (X = In, Cd, Ag, Pd): the outer electrons are progressively removed from $[Kr]4d^{10}5s^25p^1$ in In, followed by $[Kr]4d^{10}5s^2$ in Cd, $[Kr]4d^{10}5s^1$ in Ag, and $[Kr]4d^{10}$ in Pd. Note that Au has the electronic configuration of $[Kr]5d^{10}6s^1$, which is similar to Ag but with a higher energy

level. Ag has one less $5s$ electron than Cd, contributing one less electron to the conduction band and decreasing k_F. When X is varied from Cd to Ag, θ_p shows a very large jump from from -78 K to -7 K, suggesting a large electronic effect. When X is substituted from Ag to Pd, θ_p changes from -7 K to $+108$ K. The degree of lattice contraction in the Ag→Pd substitution is similar to that in the Cd→Ag substitution, implying the electronic effect has a greater impact on θ_p than the lattice effect. The removal of the outermost electrons in the s-orbital in $GdCu_4X$ (Cd, Ag, Pd) makes the compound more ferromagnetic, as indicated by the sign change of θ_p. A similar transition from a strong AFM to strong FM exchange interactions between Gd moments has been observed in Gd-monopnictides GdX_p (X_p = Bi, Sb, As, P, and N), which also form the fcc lattice by Gd moments. For GdX_p, the lattice parameter plays a crucial role in controlling θ_p [200, 201, 202]. When X_p is changed from Bi to N, which is an isoelectric substitution, the θ_p values change from -45 K to $+81$ K as the lattice parameter decreases by 20 %. The lattice contraction for GdX_p is much larger than that for $GdCu_4X$ case (-1.5 %). For GdX_p, the J_1 and J_2 model explains this transition, as the strong distance-dependent $d-f$ mixing interactions result in a strong FM J_1 and weak AFM J_2 via lattice contraction [201, 203].

For the case of In→Cd substitution, the trend is reversed in $GdCu_4X$. When an electron from the $5p$ orbital of In is removed, contributing one less electron to the conduction band, the θ_p value is expected to be decreased by reduced k_F. However, θ_p becomes more AFM as X changes from In to Cd. The same behavior is also observed in $GdNi_4X$. The In→Cd substitution involves p-orbital electrons contributing to the Fermi level, while the Cd→Ag→Pd substitution involves s-orbital electrons. It is plausible to conjecture that different types of electrons (s-like or p-like) have different effects on the conduction bands, leading to different exchange interactions. This observation suggests that the type of electron seems to matter to determine θ_p.

The Cu→Ni substitution has a relatively large lattice ($\Delta a/a \sim -3\%$) contraction, and it is expected to cause a shift of θ_p towards a large and positive value. However, the observed θ_p values for all Ni-based compounds are small. The Cu atom in these family has a closed d-shell with electronic configuration of $[Ar]3d^{10}4s^1$, which is confirmed from $YbCu_4X$ by Cu K-edge XAS experiments, and provides an electron from its s-orbital to the conduction band [204]. It has been suggested that Cu and Ni atoms provide the same number of s-electrons to the conduction band [205]. Since Ni has one less d-electron than Cu and there are four more Ni atoms than Gd and X atoms in the unit cell, the number of d-electrons contributing to the conduction band should be considered. It seems that, unlike the case for removing s-electrons, reducing the number of d-electrons does not induce a drastic effect, changing θ_p from large negative to large positive. This may be partly due to the electronic effect being partially offset by the lattice effect. Again, the type of electrons, d vs s, seems to be important to describe actual materials with RKKY interaction.

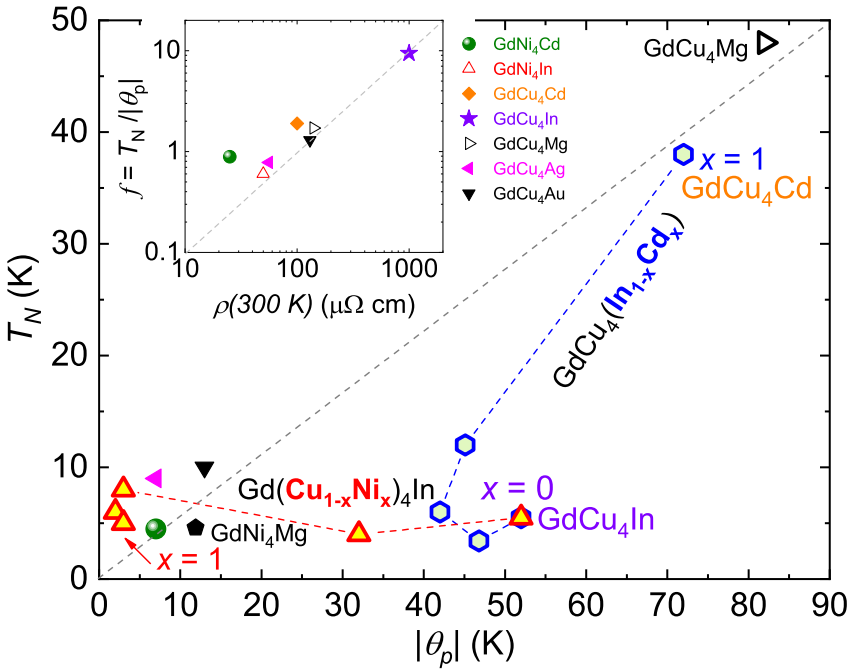

Figure 5.10: T_N as a function of $|\theta_p|$. The inset shows frustration parameter, $f = |\theta_p|/T_N$, as a function of room temperature resistivity $\rho(300\ \mathrm{K})$. Same $\rho(300\ \mathrm{K})$ data as in Fig 5.8(d) are used and additional $\rho(300\ \mathrm{K})$ value for $GdCu_4In$ (purple star) [39] is added. T_N and θ_p data are obtained from this work and previous reports: $GdNi_4Cd$ (this work), $GdNi_4Mg$ [179], $GdCu_4Mg$ [180], $GdCu_4Ag$ [182], $GdCu_4Au$ [183], $GdCu_4(In_{1-x}Cd_x)$ [39], $Gd(Cu_{1-x}Ni_x)_4In$ [185].

We now examine how the observed T_N values for GdT_4X vary in relation to θ_p and carrier-density upon substitution in T and X. In metallic RT_4X, the magnetic ordering temperature exhibits a strong correlation with θ_p; higher θ_p values result in higher T_N values as shown in Fig. 5.10. In antiferromagnets, the ordered state is characterized by a non-zero wave vector $\mathbf{Q}$, where the magnetic ordering temperature is given by the equation $T_m = 2(g-1)^2 J(J+1)\mathcal{J}(\mathbf{Q})/3k_B$. Thus, it has been often observed that T_N is lower than $|\theta_p|$. In addition, $T_N < |\theta_p|$ may indicates a sign of magnetic frustration. Note that the wave vector in ferromagnets is zero $\mathbf{Q} = 0$ in the ordered state. The small f values ranging from 0.5 to 2 in metallic RT_4X suggest that the effect of the magnetic frustration is not significant. Thus, the wave vector-dependent exchange interaction is responsible for $T_N < |\theta_p|$ in metallic RT_4X compounds. However, the large value of $f \sim 10$ observed in $GdCu_4In$ case implies the magnetic frustration in low carrier-density, semimetallic state which results from the Fermi level lying on the quasi-gap in the density of states [206]. It has been suggested that the magnetic frustration in Gd moments in $GdCu_4In$ or $HoCu_4In$ arises from short-range superexchange interactions due to the insufficient carrier-density, which prevents the formation of a long-range magnetic order. [40, 39].

In the J_1-J_2 model, the relative strength between nearest neighbor exchange interaction J_1 and next nearest neighbor exchange interaction J_2 gives rise to various magnetic structures in the fcc antiferromagnets, including type-I ($\alpha = J_2/J_1 \leq 0$), type-II ($1/2 \leq \alpha \leq \infty$), and type-III ($0 \leq \alpha \leq 0.5$) [207, 208]. For the low carrier-density systems, neutron diffraction experiments have confirmed that the magnetic structure of $GdCu_4In$ and $HoCu_4In$ is partially frustrated, where half of the rare earth moments are frustrated and the other half are ordered below T_N [40, 42]. This magnetic structure is intermediate between type-I and type-III and is realized only when J_2 is zero. We suspect that the absence of J_2 may result from the low carrier-density nature. Neutron diffraction experiments for the metallic case has shown that $HoCu_4Cd$ has a type-II magnetic structure. It is not unreasonable to assume that $GdCu_4Cd$ has the same type-II magnetic structure. In this assumption, as the concentration of Cd in $GdCu_4(In_{1-x}Cd_x)$ increases, the magnetic structure is expected to evolve from the partially frustrated to type-II. In this substitution, the lattice parameter changes a little, leading to a small change in θ_p. However, there is a significant enhancement of T_N probably due to a significant increase in the carrier-density and consequently greater contribution from J_2. On the other hand, although the carrier-density is significantly increased, T_N remains near 5 K for $Gd(Cu_{1-x}Ni_x)_4In$ case. Increasing x in $Gd(Cu_{1-x}Ni_x)_4In$ causes a large variation of θ_p due to a large change of the lattice parameter. Although the recovered metallic carrier-density induces a long-range RKKY interaction, T_N cannot exceed $|\theta_p|$ because it is bound by $|\theta_p|$ [189]. In these substitutions, the doping concentration x does not result in a continuous variation of θ_p, where θ_p changes abruptly at the critical concentration near $x \sim 0.75$ [39, 185]. A similar behavior has been observed from the carrier-density dependence of θ_p in semiconductors [209, 210]. The step-like change of θ_p

requires a modified RKKY model with a two-valence-band approximation and a finite mean free path for carriers [210]. Thus, more realistic band structures are necessary to explain the variation of θ_p in GdT_4X.

The observation of small T_N values in GdNi$_4X$ is not surprising because T_N is bounded by $|\theta_p|$. However, it is worth investigating what makes θ_p of Ni-based compounds small. According to the calculation of $\mathcal{J}(\mathbf{Q})$ for a fcc lattice [197], various magnetic structures are possible depending on k_F. The calculation shows that the FM structure is stabilized at low k_F and transitions into the type-II AFM structure as k_F increases. For GdCu$_4X$ (X = Cd, Ag, and Pd) cases, the variation of θ_p from a large negative to large positive may be related to the FM−AFM transition region in the $\mathcal{J}(\mathbf{Q})$ calculation. We conjecture for GdNi$_4X$ (X = Cd, Mg, and In) cases that the strength of the exchange interactions between molecular fields produced by rare-earth planes (θ_p) is suppressed by lattice contraction. Further electronic band structure calculations are necessary to determine the potential connection between the incomplete d-shell of Ni and the lack of strong ferromagnetism in GdNi$_4X$.

5.6 Summary

We have successfully grown single crystals of RNi$_4$Cd (R = Y, Ce, Nd, Sm, and Gd−Tm) using the Cd flux and determined that they have the MgCu$_4$Sn-type structure. Ce and Ni ions are non-magnetic, with Ce having a 4+ valence state. The other rare-earth magnetic ions have a 3+ valence state, and the magnetic behavior of these heavy rare-earth compounds is well described by Hund's rule ground state J. We have found that the Curie-Weiss temperature θ_p of isostructural metallic compounds RT_4X (R = Gd−Tm, T = Cu and Ni, and X = Cd, In, Mg, Ag, and Au) shifts towards a positive direction as the lattice parameter decreases, except for RCu$_4$Pd. This behavior can be qualitatively explained by RKKY theory. We have also investigated the parameters and conditions affecting θ_p and T_N in GdT_4X and their relationships. The substitution of T and X in GdT_4X has both lattice and electronic effects, with the dominant effect deduced from experimental observations. Lattice contraction tends to increase k_F, while removing the outermost electrons in the s-orbital in GdCu$_4X$ results in a more ferromagnetic compound. However, θ_p of GdNi$_4X$ compounds approaches zero as the lattice parameter decreases. Further investigation is necessary to elucidate this behavior.

Chapter 6

Physical properties of $Ce_{3+x}Ru_4Sn_{13-x}$

6.1 Introduction

The intermetallic compounds with a nominal stoichiometry $R_3T_4X_{13}$ (R = rare-earth or alkaline earth, T = transition metal, and X = p-block element) crystallize into the cubic $Yb_3Rh_4Sn_{13}$-type structure ($Pm\bar{3}n$) [211, 212] and show diverse phenomena such as superconductivity [213], heavy fermion behavior [214], and charge-density-wave transition [215, 216]. In addition, some Ce- and Yb-based $R_3T_4X_{13}$ compounds such as $Ce_3Rh_4Sn_{13}$ and $Yb_3Ir_4Ge_{13}$ show complex magnetic behavior with no clear signature of long-range magnetic order [217, 4]. In the $Yb_3Rh_4Sn_{13}$-type structure, a tilted three-dimensional network of corner-sharing $Rh(Sn)_6$ trigonal prisms forms the backbone of the crystal structure and two large cavities in cuboctahedra and icosahedra arrangements are filled by Yb (Wyckoff position 6d) and Sn (Wyckoff position 2a), respectively [218]. In some $R_3T_4X_{13}$ (3-4-13) compounds, the X atoms at the 2a site can be substituted by R atoms [219, 220], leading to the chemical formula $R_{3+x}T_4X_{13-x}$, where x is the occupancy of R at the 2a site. When the X atoms at the 2a site are fully substituted by R atoms (e.g., $x = 1$), compounds are known to adopt the cubic $LaRuSn_3$-type (1-1-3) structure ($Pm\bar{3}n$) [219]. For example, RPtIn$_3$ [221], $CeRuGe_3$ [222], RRhSn$_3$ [223], and RRuSn$_3$ [219] adopt the $LaRuSn_3$-type structure. However, in these compounds, the mixed occupancy at the 2a site has been observed and their 3-4-13 counterparts ($x = 0$) are also reported. Therefore the general formula $R_{3+x}T_4X_{13-x}$ can be used to describe the type of structure in this family of compounds.

Although the 3-4-13 ($x = 0$) and 1-1-3 ($x = 1$) compounds belong to the same space group $Pm\bar{3}n$, their observed physical properties show significant differences mostly due to the replacement of X atoms by R atoms at the 2a site. For example, the compound $Ce_3Rh_4Sn_{13}$ reveals no magnetic ordering down to 50 mK [224], whereas the compound $CeRhSn_3$ shows typical Kondo lattice behavior with a magnetic phase transition at 4 K [223]. The electrical resistivity of $La_3Rh_4Sn_{13}$ follows metallic behavior [217, 225, 226], but $LaRhSn_3$ shows

semiconductorlike behavior [223]. The heavy fermion $Ce_{3+x}Ru_4Sn_{13-x}$ system also shows a strong x-dependence in their physical properties [227, 228, 229, 230]. At low temperatures, the specific heat divided by temperature, C/T , of $Ce_3Ru_4Sn_{13}$ shows a diverging behavior as temperature decreases, reaching a value as high as 4 J mol_{Ce}^{-1} K^{-2} at $T = 0.4$ K [227], while C/T of $CeRuSn_3$ shows a broad maximum at $T \sim 0.6$ K with a value of 1.5 J mol_{Ce}^{-1} K^{-2} [230]. The magnetic susceptibility measurement of $CeRuSn_3$ also indicates a broad maximum at $T \sim 0.6$ K [230], where the origin of the maximum is suggested to be short-range magnetic fluctuations and (or) spin-glass dynamics [231, 230]. The electrical resistivity measurements of these compounds also show a clear distinction in that $Ce_3Ru_4Sn_{13}$ follows metallic Kondo lattice behavior [227] and $CeRuSn_3$ shows semiconductorlike behavior [230].

In this thesis, we demonstrate that physical properties of the $Ce_{3+x}Ru_4Sn_{13-x}$ system are very sensitive to the initial Ce/Sn loading compositions, eventually controlling the Ce occupancy at the $2a$ site. In order to control the occupancy of Ce at the $2a$ site, single crystals of $Ce_{3+x}Ru_4Sn_{13-x}$ ($0.05 \leq x \leq 0.34$) have been grown with Sn flux with various Ce/Sn ratios. A systematic variation of thermodynamic and transport properties is clearly observed as x increases from 0.05 to 0.34. The observed physical properties for the $x = 0.05$ and 0.34 single crystals are quite similar to those of earlier polycrystalline $Ce_3Ru_4Sn_{13}$ and $CeRuSn_3$ results, respectively.

6.2 Experiments

Single crystals of $Ce_{3+x}Ru_4Sn_{13-x}$ ($0.05 \leq x \leq 0.34$) were prepared with different initial Ce, Ru, and Sn ratios. High purity Ce, Ru, and Sn were loaded into an alumina crucible with the ratio described in Table 6.1. The crucible was sealed into an amorphous silica tube under partial Argon atmosphere. The ampoule was heated and cooled in a furnace with the temperature profile in Table 6.1. Right after the ampoule was removed from the furnace, the crystals were separated from the liquid by a centrifuge. The as-grown single crystals with the dimension of $\sim 6 \times 6 \times 6$ mm^3 ($\sim$0.6 g) show clear facets with Sn droplets on the surface, as shown in the inset of Fig. 6.2. The batch with 3 % Ce (Sample #0) yields only binary Ru_3Sn_7 and the batch with Ce 15 % (Sample #6) produces only $CeSn_3$. The decanting temperature of Sample #1 and #5 was set to 950 °C to avoid Ru_3Sn_7 and $CeSn_3$ binary phases. It has to be noted that when the decanting temperature is set to 900 °C for the batch with 3.75 % Ce (Sample #1) both binary and ternary phases are obtained. However, raising the decanting temperature from 900 to 950 °C does not significantly affect the electrical resistivity (see below results). The single crystals of $La_{3+x}Ru_4Sn_{13-x}$ were prepared with the same growth condition as Sample #5 in Table 6.1.

The composition of the grown single crystals was determined from Energy-dispersive X-ray (EDX) spectra, obtained from a FEI Helios NanoLab 650 FIB/SEM system equipped with a EDAX Octane 60 mm^2 EDX detector. The EDX spectra were collected by selecting

three 1500 μm $\times$ 500 μm areas with accelerating voltage of 30 kV for 100 seconds. To verify the crystal structure of the title compound, powder X-ray diffraction (XRD) patterns of crushed single crystals were collected in a Rigaku MiniFlex diffractometer at room temperature. Silicon powders as an internal standard were added to correct the instrument's zero shift (Fig. 6.2). Large single crystals were cut into appropriate sizes using a wire saw and all surfaces were polished before performing physical property measurements. The dc magnetization, for temperature ranging from 1.8 K to 300 K and magnetic field up to 70 kOe applied along [100] crystallographic direction, was measured in a Quantum Design (QD) Magnetic Property Measurement System (MPMS). Electrical resistivity measurement was performed down to 1.8 K in a QD Physical Property Measurement Systems (PPMS). Specific heat was measured by the relaxation method down to $T = 0.4$ K for Sample #5 and to $T = 1.8$ K for the rest of samples in a QD PPMS.

6.3 Results and analysis

6.3.1 Crystal structure and composition analysis of $R_{3+x}\mathbf{Ru_4Sn_{13-x}}$ (R = Ce and La)

Powder XRD patterns for Sample #5, as representative data, are shown in Fig. 6.2. The observed peak positions are well indexed by the $Yb_3Rh_4Sn_{13}$-type structure ($Pm\bar{3}n$). Except for a low intensity Sn peak at around $2\theta \sim 30.5°$, no unindexed peaks or impurity phases are detected. It should be noted that the obtained XRD pattern can also be indexed with the $LaRuSn_3$-type structure ($Pm\bar{3}n$). The only difference between these two structure types is the Ce/Sn occupancy at the 2a site. Due to the subtle difference in their relative intensities, we were not able to distinguish between these two structure types. Therefore, only the lattice parameter is calculated from the XRD patterns using the *FullProf* software [232]. The crystal structure of the two structure types is shown in Fig. 6.1. The 2a site is at the vertices and the center of the cube. Each Ce ion at the 2a site is encapsulated by Sn icosahedron (dark cyan).

Table 6.1: Summary of single crystal growth conditions and parameters obtained from EDX and XRD.

	ILC[1]			TP[2]	EDX[3] (at. %)			$R_{3+x}Ru_4Sn_{13-x}$.	LP[4]	Phase
#	Ce	Ru	Sn		Ce	Ru	Sn	x	a (Å)	
0	3	5	92	(1190, 900, 3)						Ru_3Sn_7
1	3.75	5	91.25	(1200, 950, 1)	14.3(2)	18.7(4)	67.0(6)	0.05(6)	9.7326(16)	$Ce_{3+x}Ru_4Sn_{13-x}$
2	5	5	90	(1190, 900, 3)	14.6(2)	18.8(2)	66.6(1)	0.12(3)	9.7302(16)	$Ce_{3+x}Ru_4Sn_{13-x}$
3	7.5	5	80.75	(1190, 900, 3)	14.9(3)	18.5(2)	66.6(5)	0.18(4)	9.7299(12)	$Ce_{3+x}Ru_4Sn_{13-x}$
4	10	5	85	(1190, 900, 3)	15.2(2)	18.9(2)	65.9(2)	0.23(3)	9.7277(17)	$Ce_{3+x}Ru_4Sn_{13-x}$
5	13	5	82	(1200, 950, 1)	15.6(2)	18.9(2)	65.5(2)	0.34(3)	9.7272(16)	$Ce_{3+x}Ru_4Sn_{13-x}$
6	15	5	80	(1190, 900, 3)						$CeSn_3$
	La	Ru	Sn							
7	13	5	82	(1190,950,1)	16.7(0)	18.3(1)	65.1(1)	0.65(3)	9.7664(16)	$La_{3+x}Ru_4Sn_{13-x}$

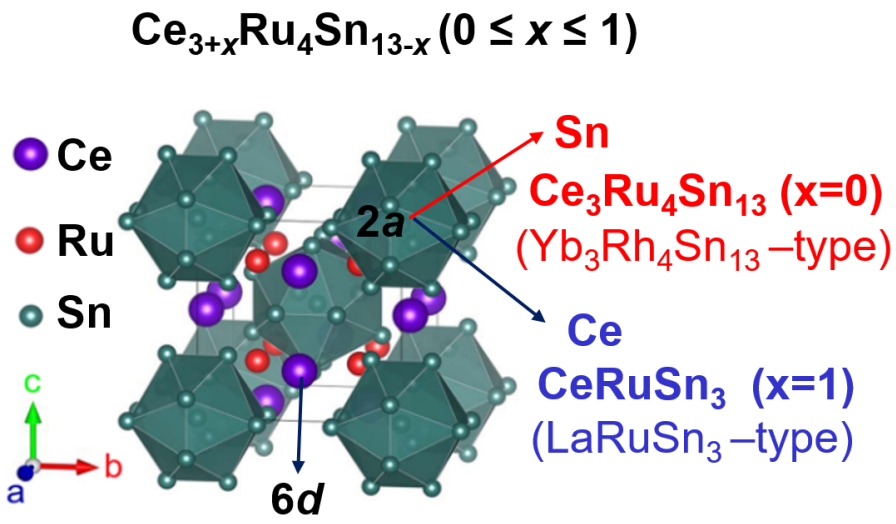

Figure 6.1: Crystal structure of $R_{3+x}Ru_4Sn_{13-x}$ with two different reported structure types. Figure is modified from [233].

The chemical compositions of the grown single crystals (Sample #1-5), obtained from EDX analysis, are plotted in Fig. 6.3 as a function of initial Ce loading composition (Ce load %). The obtained Ce composition increases as Ce load % increases, whereas the Sn composition decreases as Ce load % increases. The composition of Ru remains relatively constant for all measured samples, suggesting the full occupancy of Ru at the 8*e* Wyckoff position. An earlier study on RPtIn$_3$ shows full occupancy at the 8*e*, 6*d*, and 24*k* sites and mixed occupancy at the 2*a* site [221]. This structural feature is prevalent in this family of materials, including $Ca_{3+x}Co_4Sn_{13-x}$ [220] and $Ce_{3+x}Ru_4Ge_{13-x}$ [222], as revealed by X-ray and neutron diffractions. In addition, the full occupancy of rare-earth atoms at the 2*a* site is realized in RRuSn$_3$ (R = La, Ce, Pr, and Nd) [219] and the full occupancy of Sn at the 2*a* site is revealed in $Ce_3Ru_4Sn_{13}$ [234]. Therefore, we determined the chemical formula of the currently studied samples by fixing the averaged Ru composition of five samples to 4. When the mixed occupancy at the 2*a* site (Ce/Sn) and the full occupancy at the 8*e* (Ru), 6*d* (Ce), and 24*k* sites (Sn) are assumed, the obtained chemical formula are consistent with the general formula $Ce_{3+x}Ru_4Sn_{13-x}$. Based on this assumption we infer the Ce occupancy at the 2*a* site from x that is found to be 0.05 for the lowest Ce load % (Sample #1) and 0.34 for the highest Ce load % (Sample #5). Note that the EDX analysis doesn't provide the occupancy of atoms at their respective sites, and thus high resolution X-ray experiments with Rietveld refinements must be performed to obtain the actual occupancies at given sites. The estimated x values are summarized in Table 6.1, where x increases as Ce load % increases. The composition of the non-magnetic analog is also obtained using the same EDX analysis and x value is found to be $x \simeq 0.65$.

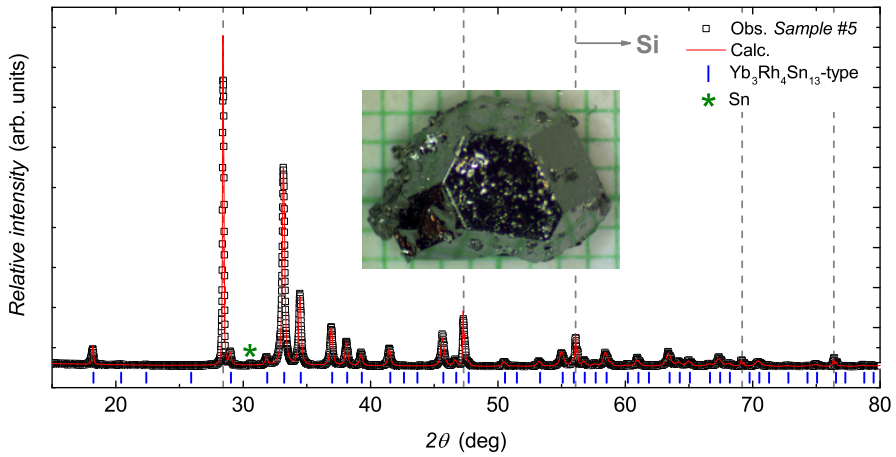

Figure 6.2: Powder X-ray diffraction patterns of Sample #5 together with Si powder. The black square symbols and red line denote the experimental data and calculated profiles, respectively. The vertical blue bars indicate the theoretical Bragg peak positions for the $Yb_3Rh_4Sn_{13}$-type structure. The Sn impurity phase is marked by the green asterisk. The vertical dashed lines represent the Si Bragg peak positions. Inset shows a photograph of Sample #5 on a 1 mm grid.

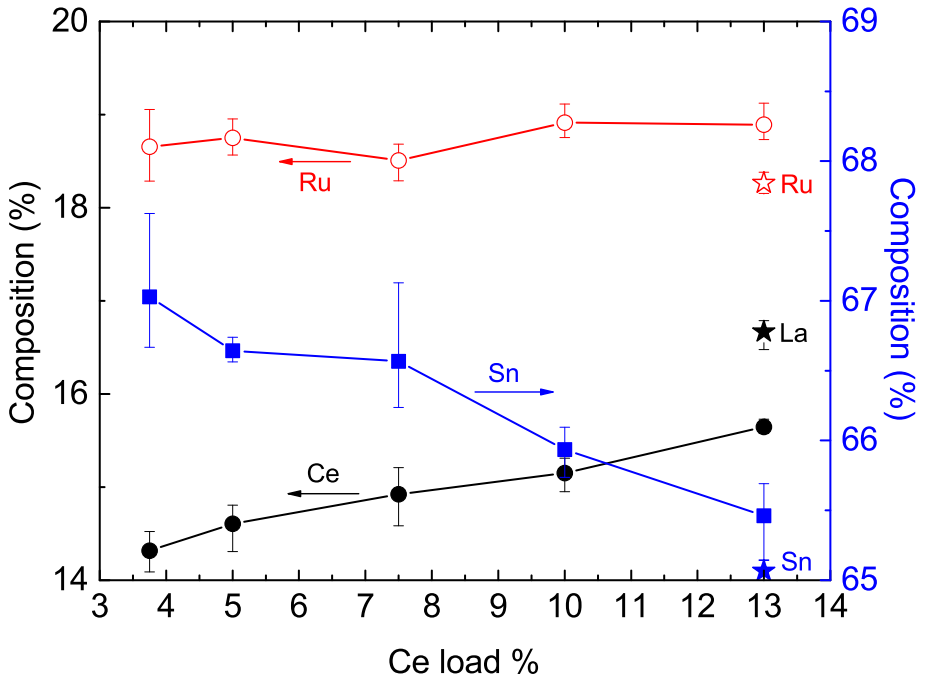

Figure 6.3: Chemical compositions (%) of $Ce_{3+x}Ru_4Sn_{13-x}$ obtained from EDX, plotted as a function of Ce load %. The left and right axes represent the composition of Ce and Ru and the composition of Sn, respectively. EDX analysis of the La-sample is presented by star symbols.

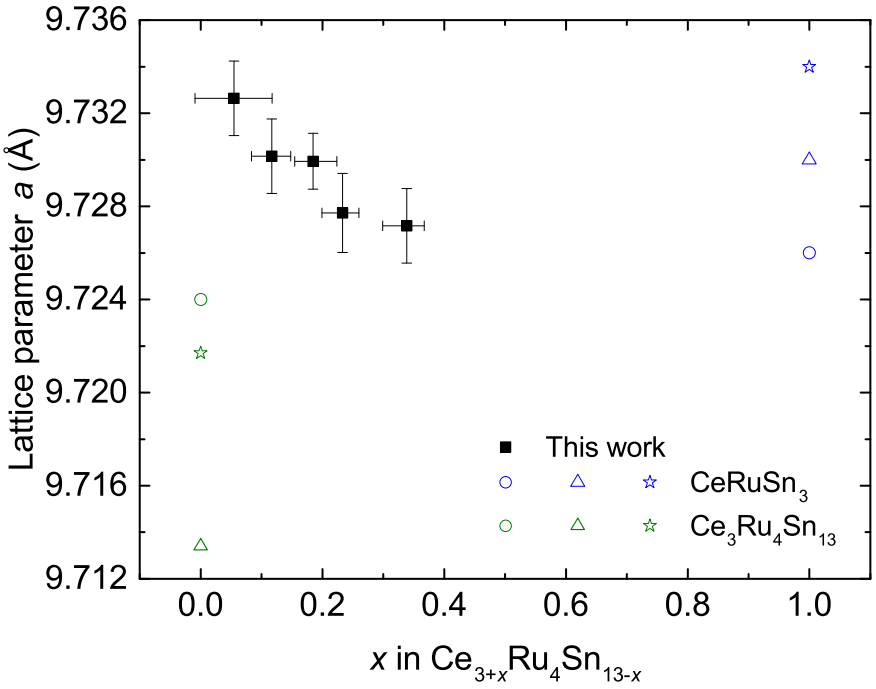

Figure 6.4: Lattice parameter a, plotted as a function of x. Open symbols for $x = 0$ and $x = 1$ are taken from Refs. [235, 236, 234] and from Refs. [231, 228, 219], respectively. Closed symbols for $0.05 < x < 0.34$ are obtained in this work.

The obtained lattice parameters are plotted in Fig. 6.4 as a function of x, together with earlier polycrystalline sample studies [235, 236, 234, 231, 228, 219]. The x-error bars are based on the lower and upper bounds of averaged Ru composition and the y-error bars are estimated from the deviation of the expected Si Bragg peak positions. The lattice parameter obtained in this study generally decreases with increasing x, which is opposite to what has been reported in earlier studies. In the earlier polycrystalline sample studies, lattice parameters for all reported $CeRuSn_3$ samples ($x = 1$) [231, 228, 219] are larger than that of all reported $Ce_3Ru_4Sn_{13}$ samples ($x = 0$) [235, 227, 234]. The XRD patterns of the compound $La_{3+x}Ru_4Sn_{13-x}$ can also be indexed with both the $Yb_3Rh_4Sn_{13}$-type and $LaRuSn_3$-type structures (not shown). The reported lattice parameter of $La_{3+x}Ru_4Sn_{13-x}$ compounds mostly ranges from $a = 9.766$ Å to 9.777 Å for $La_3Ru_4Sn_{13}$ [234, 236] and from $a = 9.773$ Å to 9.782 Å for $LaRuSn_3$ [219, 228, 237]. The obtained lattice parameter $a = 9.7664(16)$ Å for $x = 0.65$ is slightly smaller than that for $x = 1$. The large fluctuation in the lattice parameter is probably due to the different sample quality and inconsistent method applied to obtain it. Thus, the comparison of the lattice parameter is not conclusive and requires further investigation.

6.3.2 Physical properties of $La_{3+x}Ru_4Sn_{13-x}$

The observed physical properties of $La_{3.65}Ru_4Sn_{12.35}$ are consistent with a weakly diamagnetic intermetallic compound. The magnetization measurement at 1.8 K shows a very large diamagnetic signal below 5 kOe due to the superconducting phase and shows an increase in negative magnetization at high magnetic fields, as shown in Fig. 6.5(a). The magnetic susceptibility, $M(T)/H$, at 70 kOe (left inset) weakly depends on temperature with a very small average value. In the zero-field-cooled measurement at 1 kOe, the superconducting transition occurs at about 2 K (right inset). Since the flat region of the superconducting state does not appear in the magnetic susceptibility, the concentration of the superconducting phase is not possible to estimate. Figure 6.5(b) shows the electrical resistivity, $\rho(T)$, of $La_{3.65}Ru_4Sn_{12.35}$. $\rho(T)$ follows metallic behavior (e.g. dρ/dT >0) at high temperatures and indicates a superconducting transition at T_{SC} = 2.1 K (inset). Although the observed metallic behavior is consistent with an earlier polycrystalline $La_3Ru_4Sn_{13}$ sample [227], the absolute value of the resistivity is roughly four times smaller than that of the polycrystalline sample. In addition, T_{SC} of the single crystal is slightly higher than the reported transition temperature of ∼1.5 K [227]. The difference could be due to the sample quality. Note that semiconductor-like behavior is observed for the polycrystalline $LaRuSn_3$ sample [238].

The specific heat, C_p, of $La_{3.65}Ru_4Sn_{12.35}$ as a function of temperature is shown in Fig. 6.5(c). The C_p measurement clearly confirms the superconducting phase transition at $T \sim 2.1$ K, as shown in the inset, where the peak position of the maximum coincides with the resistivity signature. Since the resistivity value goes to zero in the superconducting state and the specific heat shows a jump at ∼2.1 K, the bulk superconducting phase transition is the ternary phase, not from an impurity or Sn phase. Above T_{SC} the electronic and phonon contributions are estimated by $C_p = \gamma T + \beta T^3$. The electronic contribution γ and Debye temperature Θ_D are obtained to be ∼16.95 mJ/mol K^2 and ∼170 K, respectively, from the C_p/T vs T^2 plot (inset). The obtained Debye temperature is consistent with the earlier study (Θ_D = 150 K [227]). By using the obtained γ value, the specific heat jump $\Delta C_p/(\gamma T_{SC})$ = 1.46 is found to be only slightly above 1.43, indicating that the superconductivity in the $La_{3.65}Ru_4Sn_{12.35}$ compound can be ascribed to the conventional isotropic BCS type.

6.3.3 Resistivity behavior of $Ce_{3+x}Ru_4Sn_{13-x}$

The $\rho(T)$ curves of $Ce_{3+x}Ru_4Sn_{13-x}$ for Samples #1 –#5 ($0.05 \leq x \leq 0.34$) are shown in Fig. 6.6. The absolute value of the electrical resistivity for the entire temperature range measured increases as x increases. For $x = 0.05$ [Fig. 6.6(b)], $\rho(T)$ follows Kondo lattice behavior with a resistivity minimum at $T_{min} \sim 45$ K. T_{min} gradually moves to higher temperature as x increases. For $x \geq 0.23$, the resistivity, upon cooling, continuously increases without the minimum. The evolution of $\rho(T)$ as a function of x can be seen better from the resistivity curves normalized at 300 K. To compare, the normalized resistivity curves

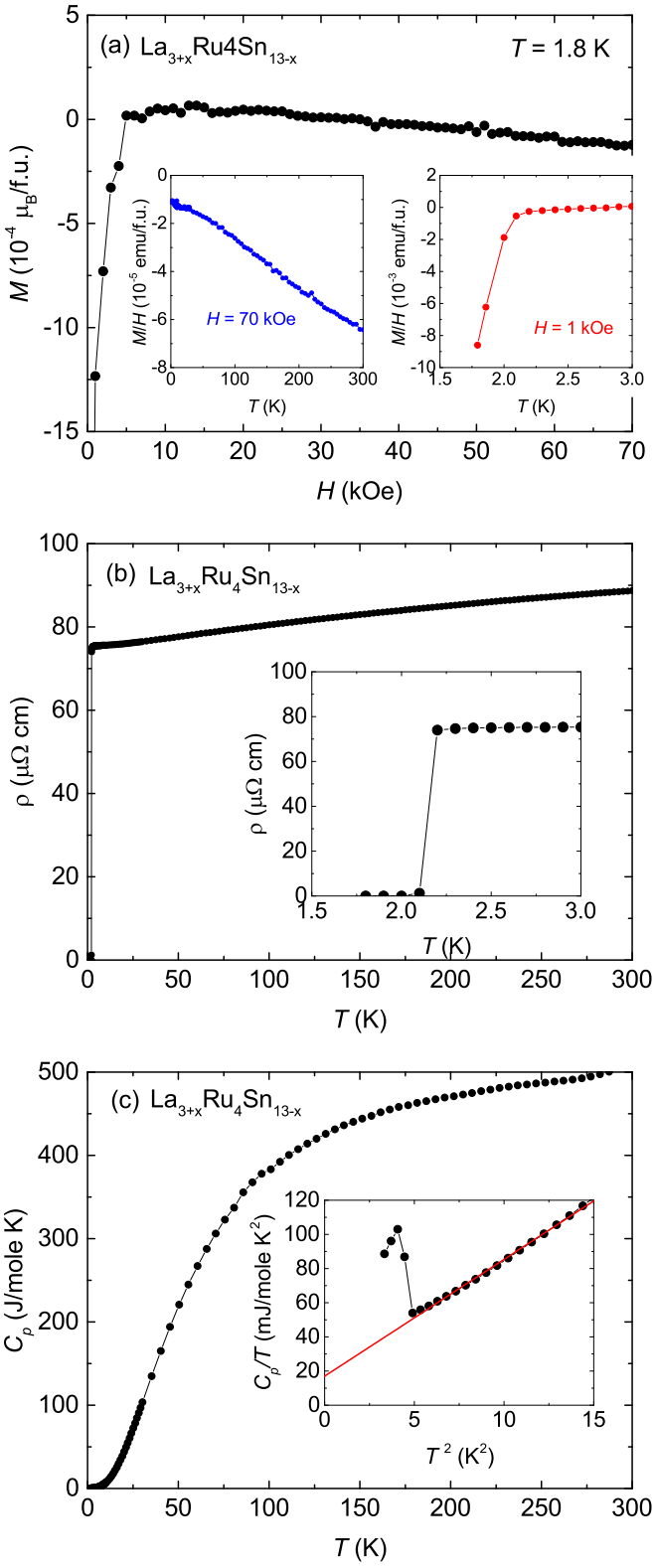

Figure 6.5: Physical properties of $La_{3+x}Ru_4Sn_{13-x}$ for $x = 0.65$. (a) $M(H)$ for $H \parallel [100]$ at $T = 1.8$ K. Insets show M/H at $H = 70$ kOe (left) below 300 K and at 1 kOe below 3 K (right). (b) $\rho(T)$ below 300 K. Inset shows the expanded plot below 3 K. (c) C_p per formula unit. Inset shows C/T vs. T^2 plot. Solid line represents the fit to $\gamma T + \beta T^3$.

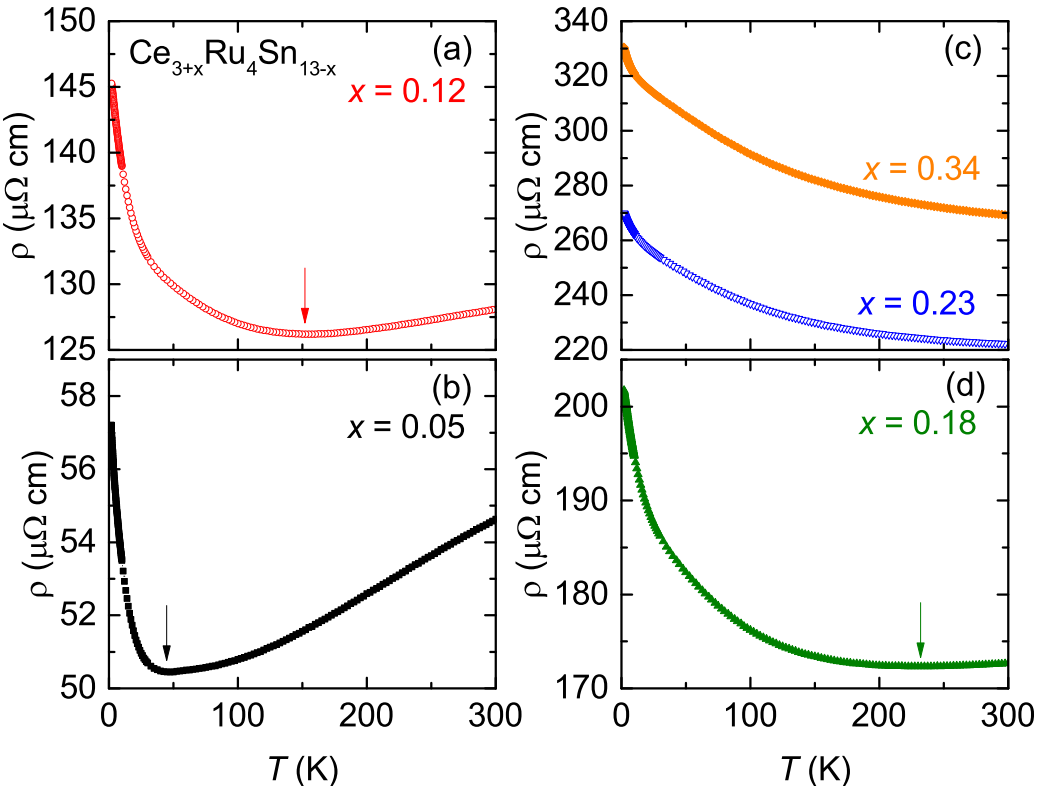

Figure 6.6: $\rho(T)$ of $Ce_{3+x}Ru_4Sn_{13-x}$ for (a) $x = 0.12$, (b) $x = 0.05$, (c) $x = 0.23$ and 0.34, and (d) $x = 0.18$. Vertical arrows indicate the position of the resistivity minimum T_{min}.

of polycrystalline $Ce_3Ru_4Sn_{13}$ ($x = 0$) [227] and $CeRuSn_3$ ($x = 1$) [230] are plotted together with the currently studied single crystals in Fig. 6.7. The normalized $\rho(T)$ curves of $Ce_{3+x}Ru_4Sn_{13-x}$ single crystals systematically vary between $x = 0$ and $x = 1$. The resistivity value at 300 K, $\rho(T = 300\ \text{K})$, and the observed T_{min} for various x are plotted in Fig. 6.9, where both $\rho(T = 300\ \text{K})$ and T_{min} increase quasi-linearly as x increases. It should be noted that $\rho(T = 300\ \text{K})$ for polycrystalline $Ce_3Ru_4Sn_{13}$ is much higher than that for samples with $x > 0$.

6.3.4 Growth condition dependence on resistivity behavior of $Ce_{3+x}Ru_4Sn_{13-x}$

$\rho(T)$ of the $Ce_{3+x}Ru_4Sn_{13-x}$ system is very sensitive to the initial stoichiometric ratios of the constituent elements. In addition, the cooling rates and decanting temperatures of the samples appear to be critical parameters for the absolute value of the electrical resistivity. We have grown multiple samples for $x = 0.05$ with different cooling rates (1 – 10 °C per hour) and slightly different decanting temperatures. Figure 6.8 shows the normalized resistivity curves of Sample #1, a sample with a 900 °C decanting temperature and cooling rate of 1 °C/h (Sample D900), and a sample with a 950 °C decanting temperature and cooling rate of 10 °C/h (Sample C10). The normalized resistivity curves of the three samples are almost

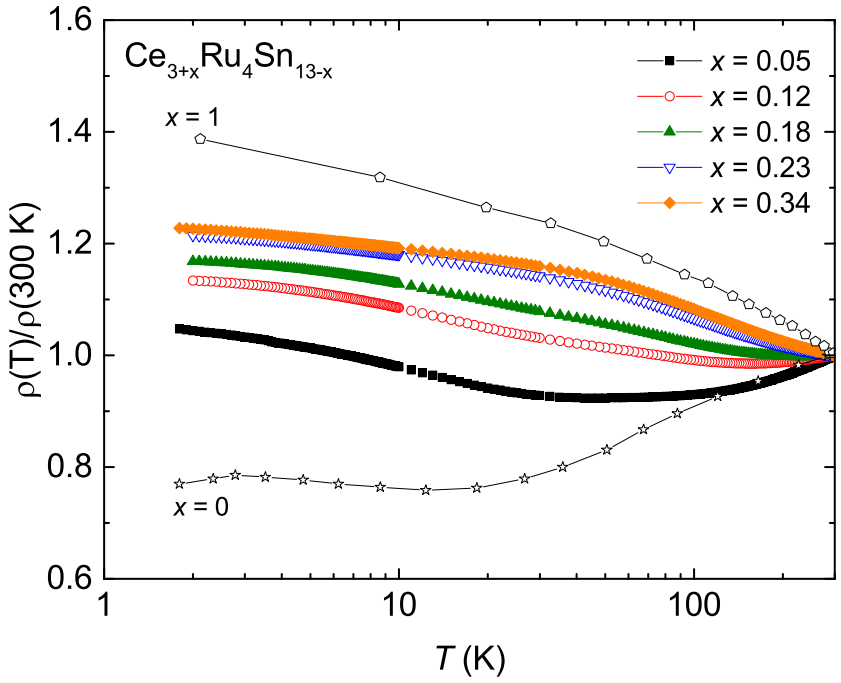

Figure 6.7: Normalized electrical resistivity, $\rho(T)/\rho(300\ \mathrm{K})$, curves for various x. Data for $Ce_3Ru_4Sn_{13}$ ($x = 0$) [227] and $CeRuSn_3$ ($x = 1$) [230] are taken by hand from the references and normalized at 300 K.

identical, with the temperature dependences and T_{min} remaining the same. However, the absolute value of the resistivity is affected by the temperature profiles, as shown in the inset of Fig. 6.8, which is probably driven by the large degree of grain boundary effects.

With varying the occupancy of Ce at the 2a site, the electrical resistivity of the $Ce_{3+x}Ru_4Sn_{13-x}$ system drastically changes from metallic Kondo lattice behavior ($x = 0$) to semiconductor-like behavior below 300 K ($x = 1$). Such sample-dependent electrical resistivity has been observed in earlier polycrystalline $CeRuSn_x$ ($2.85 \leq x \leq 3.15$) samples [239], where the absolute value of the resistivity becomes smaller when varying x from 3, and drastic changes in $\rho(T)$ are observed at low temperatures for both the Sn-excess case ($x > 3$) and Sn-deficient case ($x < 3$). Since the 2a site in $Ce_{3+x}Ru_4Sn_{13-x}$ is occupied by both Ce and Sn atoms, the systematic variation of the electrical resistivity can be related to the site disorder. It has been empirically demonstrated that a semiconductor-like enhancement of resistivity upon cooling in germanides with $Yb_3Rh_4Sn_{13}$-type structures is related to the large crystallographic disorder: the ratio of the atomic displacement parameter (ADP) between the 2a site atom and transition metal atom correlates well to the resistivity data [213]. Note that the ADP ratio of 3-4-13 germanides is generally greater than that for metallic stannides [213]. In the currently studied samples, the highest disorder is expected from $La_{3+x}Ru_4Sn_{13-x}$ with $x = 0.65$, however the resistivity shows metallic behavior. It is expected from the inset of Fig. 6.9 that the T_{min} value for $x > 0.18$ is higher than 300 K. Therefore, it is not unreasonable

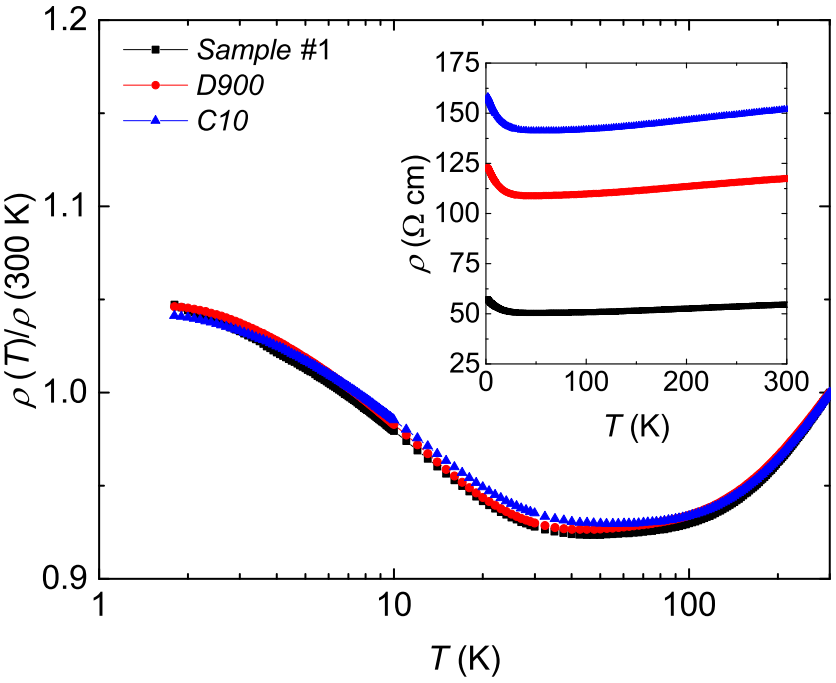

Figure 6.8: $\rho(T)/\rho(300\ \mathrm{K})$ curves of Sample #1, Sample D900, and Sample C10. (See the main text for details). Inset shows $\rho(T)$ of Sample #1, Sample D900, and Sample C10.

to assume that the semiconductor-like behavior ($\mathrm{d}\rho(T)/\mathrm{d}T < 0$) observed for $x > 0.18$ originates from Kondo scattering below T_{min}.

6.3.5 Magnetic field dependence on resistivity behavior of $Ce_{3+x}Ru_4Sn_{13-x}$

In the current study, the importance of Kondo scattering in conjunction with the crystalline electric field (CEF) effect complicates a straightforward interpretation of the resistivity data. In zero field, the combined Kondo and RKKY interactions qualitatively explain the resistivity of various Kondo lattice systems. Since no magnetic ordering has been observed in $Ce_{3+x}Ru_4Sn_{13-x}$ ($0 \leq x \leq 1$) compounds, the Kondo interaction overcomes the RKKY exchange interaction and thus a normal Fermi liquid should be realized in this system. The single-impurity Kondo-like resistivity in all samples at low temperatures and the absence of a T^2 Fermi liquid regime below the coherence temperature are puzzling. Therefore, the resistivity is measured under external magnetic fields that will suppress the contributions of both Kondo and RKKY scattering at different rates. The magnetoresistance (MR) of $Ce_{3+x}Ru_4Sn_{13-x}$ at 1.8 K for $H \parallel [100]$ is shown in Fig. 6.10(a). Although the relative variation of MR is small for all x, probably due to the disorder, the MR curves clearly show a systematic evolution, changing from negative to positive MR as x increases. MR for $x = 0.05$ is negative for all measured fields, suggesting that the $\rho(T)$ upturn below T_{min} could arise due to the Kondo interaction.

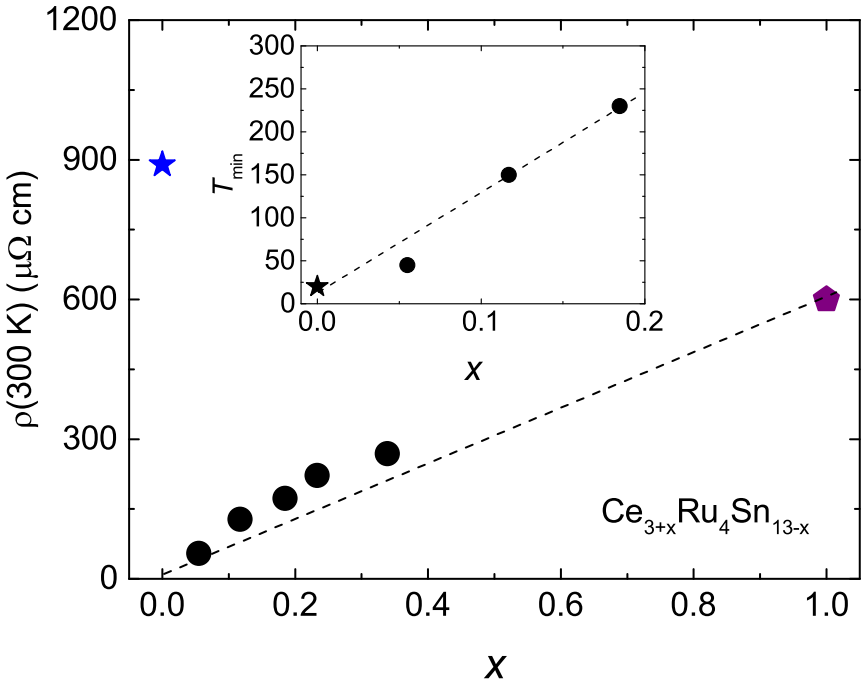

Figure 6.9: Resistivity value at 300 K, $\rho(300\ \mathrm{K})$, for various x. Inset shows the resistivity minimum, T_{min}, for $x < 0.2$. Star ($x = 0$) and pentagon ($x = 1$) symbols are taken from Ref. [227] and [230], respectively. Lines are guides to the eyes.

The $\rho(T)$ curves at various magnetic fields further support the Kondo effect. In zero field, a logarithmic increase of the resistivity with decreasing temperature, $\rho(T) \sim -\log(T)$, indicates incoherent Kondo scattering as shown in Fig. 6.10(b). At low temperatures, a magnetic field suppresses spin-flip scattering, causing the negative MR and the development of a maximum (coherence). The maximum moves to a higher temperature as magnetic field increases, which is consistent with the behavior observed in many heavy fermion (Kondo lattice) systems. The MR curve for $x = 0.34$ is positive at low fields but starts showing a negative trend as the field increases further. In zero field, $\rho(T) \propto -\log(T)$ behavior is dominant, however the resistivity measurements indicate a negligible MR as shown in Fig. 6.10(c). It will require a much higher magnetic field to observe the maximum in the resistivity. We conjecture that the evolution of MR as a function of x is caused by the combination of Kondo scattering at the $6d$ site and an increase in the randomness of f-electron scattering at the $2a$ site. It should be distinguished from the effect of dilution of f-sites (i.e., the Ce-ions are replaced by non-f-ions like La-ions). It has been shown that different Kondo systems exhibit positive or negative MR depending on the temperature regime, the number of occupied f-electrons per site, and the Kondo temperature. For the $Ce_{3+x}Ru_4Sn_{13-x}$ system, the disorder (especially related to the $2a$ site) increases as x increases, implying that the random f-electron scatterings become significant for higher x.

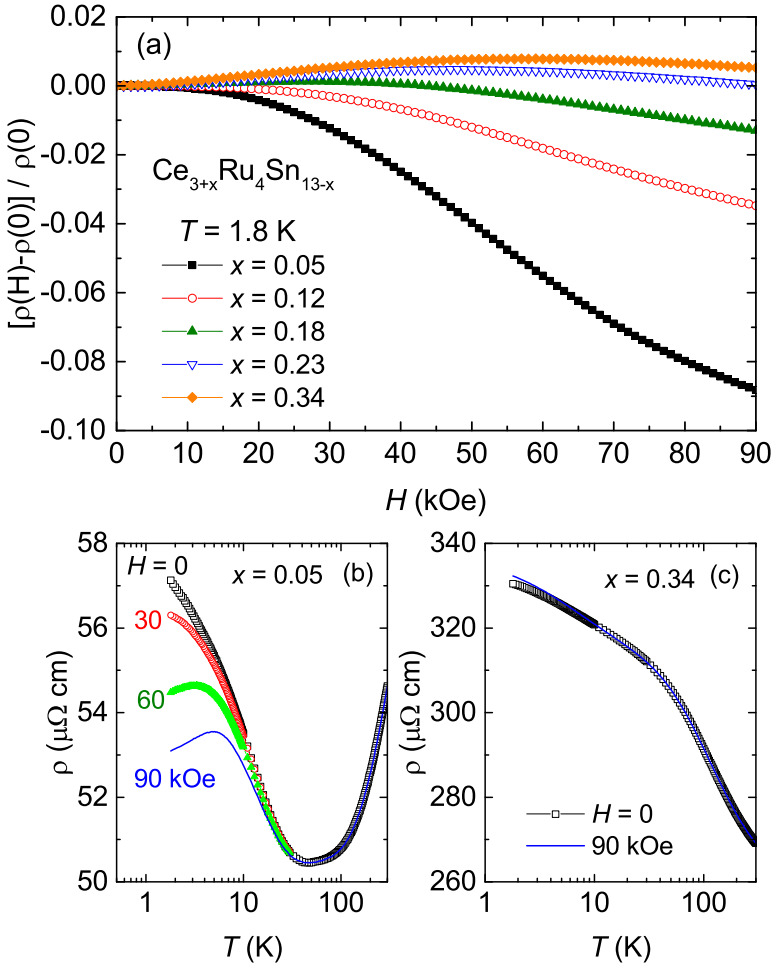

Figure 6.10: (a) Magnetoresistance, $[\rho(H)-\rho(0)]/\rho(0)$, at $T = 1.8$ K for various x. (b) $\rho(T)$ of $x = 0.05$ at $H = 0$, 30, 60, and 90 kOe. (c) $\rho(T)$ of $x = 0.34$ at $H = 0$ and 90 kOe.

We note that the enhancement of RKKY scattering for higher x may provide an alternate explanation of the positive MR contributions. Our results suggest the relative importance of disorder contributions that may have a strong influence on the electrical resistivity.

6.3.6 Magnetization measurements of $Ce_{3+x}Ru_4Sn_{13-x}$

Inverse magnetic susceptibility, $1/\chi(T) = H/M$, curves for $Ce_{3+x}Ru_4Sn_{13-x}$ single crystals are shown in Fig. 6.11(a). All curves show a slight deviation from the linear temperature dependence above ~150 K. Therefore, the effective moments, μ_{eff}, and Weiss temperatures, θ_p, are estimated by fitting $1/\chi(T)$ curves to modified Curie-Weiss (C-W) law: $\chi(T) = \chi_0 + C/(T-\theta_p)$. The obtained results are plotted in Fig. 6.11(b) together with values from the previous polycrystalline sample studies [234, 228, 230]. The μ_{eff} values of single crystal samples are close to the expected free Ce^{3+}-ion value (2.54 μ_B). Note that μ_{eff} values

for polycrystalline samples are slightly smaller than the theoretical value. The estimated θ_p values (~ -40 K) for single crystal samples are almost independent of x, but larger than those for polycrystalline $CeRuSn_3$ and $Ce_3Ru_4Sn_{13}$ samples. It has to be noted that the obtained paramagnetic χ_0 values are in the range of $\sim 1 \times 10^{-4}$ emu/f.u., which is somewhat bigger than the diamagnetic response of La-compound, plotted in the inset of Fig. 6.5(a). It is interesting to note that mixed valence behavior has been previously observed in 3-4-13 germanides $Ce_3Ru_4Ge_{13}$, $Ce_3Os_4Ge_{13}$, and $Ce_3Ir_4Ge_{13}$ [222, 240, 241]. Both μ_{eff} and θ_p values in $Ce_{3+x}Ru_4Sn_{13-x}$ show no correlation with x, suggesting that Ce-ions in these compounds retain the 3+ valence state at both the 6*d*- and 2*a*-sites. This result is consistent with the absence of the f^0 peak associated with tetravalent Ce-ions in core-level photoemission spectra in polycrystalline $CeRuSn_3$ and $Ce_3Ru_4Sn_{13}$ samples [242, 236].

Figure 6.11(c) shows magnetic susceptibility, M/H, curves for $Ce_{3+x}Ru_4Sn_{13-x}$ single crystals. Unlike the high temperature magnetic response, the low temperature M/H curves exhibit strong x dependence. The M/H curve for $x = 0.34$ continuously increases with decreasing temperature, whereas a clear broad maximum is detected at $\sim$3.5 K for the $x = 0.05$ sample. The observed maximum gradually disappears with increasing x. It has been shown that peaks are found in the magnetic susceptibility for $J > 3/2$ (degeneracy $N = (2J + 1) > 2$) and that these peaks become pronounced as the degeneracy increases [243]. Such peaks have been observed for many Ce- ($J = 5/2$) and Yb- ($J = 7/2$) based Kondo lattice compounds [244, 245, 246, 247, 248, 249, 250]. Note that a similar broad maximum in the magnetic susceptibility is also observed at a much lower temperature $T \sim 0.6$ K in a $CeRuSn_3$ polycrystalline sample [230], but no maximum is observed down to 1.8 K in a $Ce_3Ru_4Sn_{13}$ polycrystalline sample [227]. μSR and inelastic neutron scattering studies on the $CeRuSn_3$ compound suggest that the broad maximum at $T \sim$0.6 K observed in specific heat and magnetic susceptibility is related to either short-range magnetic fluctuations or spin-glass dynamics [230, 231].

The magnetization isotherms, $M(H)$, at $T = 1.8$ K for various x are plotted in Fig. 6.11(d). The $M(H)$ curves for $x = 0.34$ and 0.23 follow Brillouin function-like behavior, whereas the curves with lower x show an increasing slope up to $\sim$50 kOe. The magnetization value at 70 kOe for all x reaches $\sim$0.5 μ_B/Ce, which is much smaller than the saturated magnetization value of the free Ce^{3+}-ion (2.14 μ_B/Ce). This reduced magnetization value could be due to the Kondo effect in conjunction with the CEF effect. Since the magnetic susceptibility measurements for $Ce_{3+x}Ru_4Sn_{13-x}$ single crystals indicate no magnetic ordering down to 1.8 K, the slope change clearly observed in $M(H)$ for $x = 0.05$ cannot be related to a metamagnetic transition generally shown in antiferromagnets. We note that an abrupt nonlinear increase of magnetization has been observed in the heavy fermion metamagnet $CeRu_2Si_2$ [251].

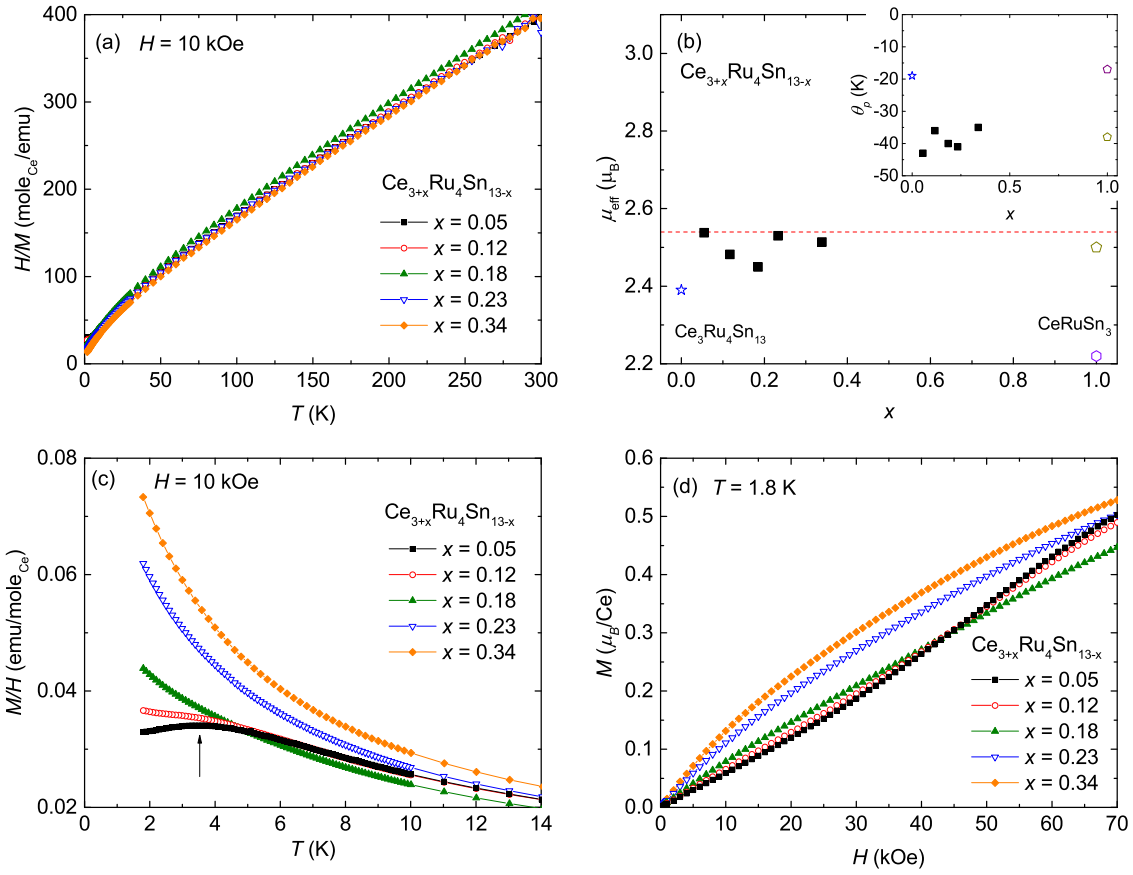

Figure 6.11: (a) Inverse magnetic susceptibility, H/M, of $Ce_{3+x}Ru_4Sn_{13-x}$ single crystals at $H = 10$ kOe along $H \parallel [100]$. (b) Effective moment μ_{eff} and Weiss temperature θ_p (inset) as a function of x. Open symbols are taken from previous studies of polycrystalline $Ce_3Ru_4Sn_{13}$ [234] and $CeRuSn_3$ [228, 230]. The dotted line is the theoretical value of the effective moment for the free Ce^{3+}-ion. (c) Magnetic susceptibility, M/H, of $Ce_{3+x}Ru_4Sn_{13-x}$ single crystals below 14 K. Vertical arrow indicates a broad maximum at ~3.5 K for $x = 0.05$. (d) Magnetization isotherms at 1.8 K along $H \parallel [100]$.

6.3.7 Specific heat measurements of $Ce_{3+x}Ru_4Sn_{13-x}$

Specific heat curves divided by temperature, C_p/T, for $Ce_{3+x}Ru_4Sn_{13-x}$ single crystals are plotted in Fig. 6.12(a). The curves display a minimum at ∼8 K with $C_p/T \sim 1$ J/mole$_{Ce}$-K^2, and show large enhancement below this minimum. The specific heat, C_p, curves below 10 K are shown in the inset of Fig. 6.12(a). A broad hump below 8 K is observed for all x, which corresponds to the enhancement of C_p/T. For $x = 0.05$, the observed C_p/T down to 1.8 K is consistent with the earlier polycrystalline $Ce_3Ru_4Sn_{13}$ sample [227]. For $x = 0.34$, a broad maximum with $C_p/T \sim 4$ J/mole-K^2 is detected around 0.5 K, which coincides with a maximum observed from the specific heat measurement of a polycrystalline $CeRuSn_3$ sample [229]. C_p/T of $La_{3.65}Ru_4Sn_{12.35}$ is comparable to that of $Ce_{3+x}Ru_4Sn_{13-x}$ above 100 K, whereas the difference between the La- and Ce-based compounds becomes significant below the minimum. Therefore, the upturn below the minimum suggests significant magnetic contributions.

The nature of the magnetic state of $Ce_{3+x}Ru_4Sn_{13-x}$ can be inferred by examining the magnetic contribution to the specific heat C_m. The C_m curves with various x are plotted in Fig. 6.12(b), where C_m is estimated by subtracting the specific heat of the nonmagnetic analog $La_{3.65}Ru_4Sn_{12.35}$. For $x = 0.05$, the C_m curve clearly shows two broad maxima at ∼3.5 K and at ∼50 K. With increasing x the absolute value of C_m becomes smaller for both maxima, while the broad peak on the high temperature side remains at almost the same temperature. For $x = 0.34$, C_m indicates no clear maximum in the low temperature regime. The electronic contribution to the specific heat is difficult to determine because C_m/T does not saturate below 8 K. We note that a large C/T value at low temperatures has been reported for the isostructural $Ce_{3+x}Ru_4Sn_{13-x}$ family and other compounds with the $Yb_3Rh_4Ge_{13}$-type structure [227, 230, 229, 217, 222, 252].

The magnetic entropy S_m of $Ce_{3+x}Ru_4Sn_{13-x}$ is estimated by integrating C_m/T, and is plotted in Fig. 6.12(c). Because of the upturn in C_m/T below 10 K, the extrapolation of the specific heat to $T = 0$ cannot be made without ambiguity. Thus, to compare the evolution of S_m as a function of x, the integration of C_m/T has been performed from 1.8 K for all x. For $x = 0.34$, the specific heat is measured from 0.4 K, and thus the entropy is also estimated by integrating C_m/T from 0.4 K and is plotted in the same figure with a solid line. As is clear from the case $x = 0.34$, the total S_m is underestimated by at least ∼1 J/mole$_{Ce}$-K. For $x = 0.05$, S_m reaches $R\ln(4)$ around 100 K, indicating that there are two doublets mainly influencing C_m, with the third doublet outside of this temperature window. Although the missing entropy below 1.8 K has to be considered, the magnetic entropy approaches $R\ln(2)$ around $30 - 40$ K for all x, suggesting that the low temperature maximum is mostly associated with either the ground state doublet or the combination of a doublet and quartet with small CEF splittings. The remaining entropy is removed far above this temperature.

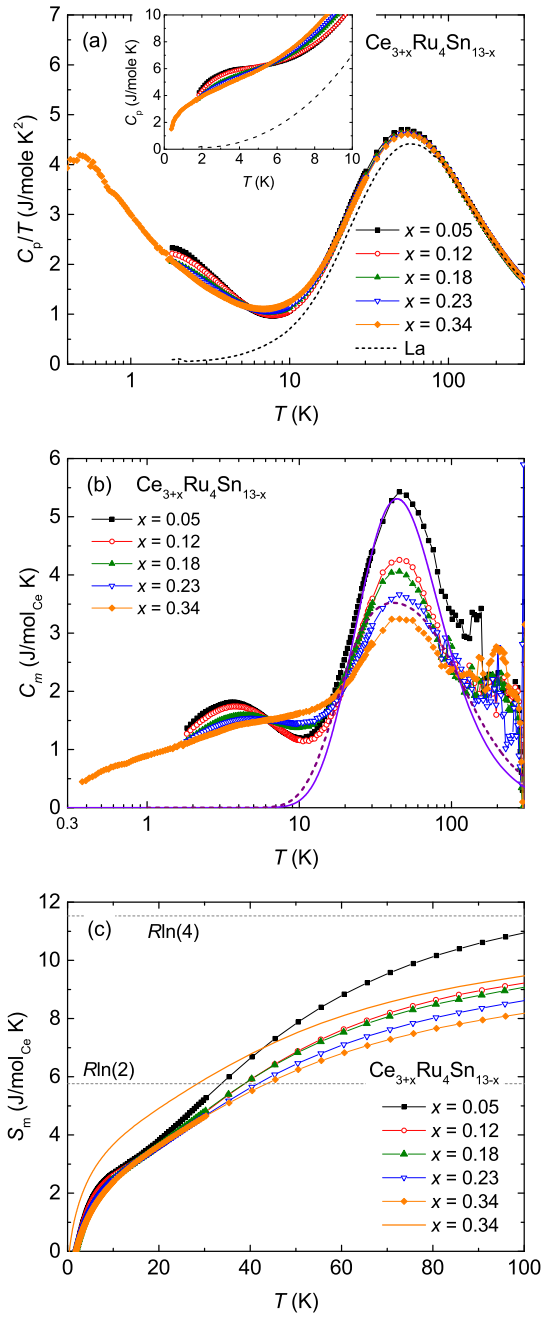

Figure 6.12: (a) C_p/T vs T plots for $Ce_{3+x}Ru_4Sn_{13-x}$ (symbols) and $La_{3+x}Ru_4Sn_{13-x}$ (dashed line). Inset shows C_p vs T below 10 K. (b) C_m for $Ce_{3+x}Ru_4Sn_{13-x}$. The solid line is the Schottky calculation with $\Delta_1 = 85$ K and $\Delta_2 = 165$ K. The dashed line represents the CEF contributions based on Ref. [231]. (c) Magnetic entropy S_m for $Ce_{3+x}Ru_4Sn_{13-x}$. The solid line is the magnetic entropy obtained by integrating C_m/T from 0.4 K for $x = 0.34$.

6.3.8 Origin of high temperature broad peak in C_m of $Ce_{3+x}Ru_4Sn_{13-x}$

The high temperature broad peak can be attributed to the Schottky anomaly. Such a maximum is typically shown in magnetic specific heat due to the splitting of the sixfold degenerate multiplet in Ce^{3+} ions. For the $x = 0$ case ($Ce_3Ru_4Sn_{13}$) the Ce^{3+}-ions occupy only the $6d$ site, and thus the tetragonal point symmetry at the Ce site splits the $J = 5/2$ Hund's rule multiplet of the Ce^{3+} ions into three doublets. For $Ce_{3+x}Ru_4Sn_{13-x}$ systems the analysis of the Schottky anomaly becomes more complex, as the actual occupancy of Ce-ions at both the $6d$ and $2a$ sites (cubic point symmetry) must be considered to properly account for CEF effects. In the present study ($0.05 < x < 0.34$) the variation in C_m curves between samples with lowest x and highest x is about $\sim$2 J/mole$_{Ce}$-K, which is comparable to the uncertainty in C_m estimation. The absolute value of C_m for $Ce_{3+x}Ru_4Sn_{13-x}$ compounds is dependent on the actual Ce-concentrations, and is also largely affected by the subtraction of the non-magnetic analog La-compound. Due to these uncertainties the absolute value of C_m can vary by as much as 1.4 J/mole$_{Ce}$-K. In particular, difficulty in accurately modelling the nonmagnetic contribution with $La_{3+x}Ru_4Sn_{13-x}$ at high temperatures prevents us from doing quantitative analysis of Schottky contributions as suggested in Ref. [231]. The Schottky contributions in $CeRuSn_3$, combined with inelastic neutron scattering data, are reproduced by considering a 25% contribution from cubic symmetry and 75% from tetragonal symmetry: the Ce ions at the $2a$ site have a quartet as a ground state and a doublet as an excited state with an energy gap $\Delta \sim 95$ K, and the Ce ions at the $6d$ site have three doublets with energy gaps $\Delta_1 \sim 72$ K and $\Delta_2 \sim 223$ K [231].

For $x = 0.05$, it is reasonable to assume that cubic CEF effects are negligible, and thus the C_m curve can be analyzed by considering Ce-ions at only the $6d$ site. The Schottky contribution is denoted by a solid line in Fig. 6.12 (b), involving three doublets separated by $\Delta_1 = 85$ K and $\Delta_2 = 165$ K. It is clear from the figure that the position of the broad maximum can be reproduced by the Schottky calculation. We expect that the difference between C_m and the Schottky calculation is probably due to subtraction error. The Schottky contribution based on Ref. [231] (dashed line) is also plotted in the same figure, accounting for CEF contributions from both the $2a$ and $6d$ sites. For $x > 0.05$, the position of the broad maximum at $\sim$50 K and the decrease in the absolute value of the C_m curves can be qualitatively explained by considering CEF contributions according to the multiplicities of both Ce-site point symmetries. It has to be noted for cubic symmetry sites that the systematic change in C_m while varying x cannot be reproduced by considering the doublet ground state. To perform more quantitative analysis it is necessary to have more reliable composition analysis to obtain actual Ce-ion occupancies between the $6d$ and $2a$ sites and subtract the nonmagnetic contributions accurately.

6.3.9 Origin of low temperature broad peak in C_m of $Ce_{3+x}Ru_4Sn_{13-x}$

At low temperatures, because the absolute value of C_m is not sensitive to subtracting the specific heat of La-based compound, it is reasonable to assume that C_m solely consists of Ce-ions' magnetic contributions. For $x = 0.05$, the broad peak in C_m at ∼3.5 K may have the same origin as the broad peak observed in the magnetic susceptibility, which is reminiscent of the Kondo effect with degenerate ground states. With increasing x, the height of the broad peak decreases and the peak becomes broader. The specific heat measurement of a previous polycrystalline $Ce_3Ru_4Sn_{13}$ sample shows a broad peak around ∼3 K, where a very large enhancement of C/T below 8 K accompanied with a broad feature around 2 K is explained by considering two low lying CEF doublets with $\Delta = 8$ K and the Kondo effect with $T_K = 2$ K [227]. Note that the absolute value of the specific heat of $Ce_3Ru_4Sn_{13}$ [227] is roughly twice bigger than that of $x = 0.05$. In the present study, both the width and height of the broad peak for all x cannot be reproduced by the Schottky anomaly, ruling out low lying CEF doublets as its origin. In addition, the entropy recovering $R\ln(2)$ at ∼30 K is inconsistent with two low lying CEF doublets with a small splitting.

For Ce- and Yb-based Kondo lattice compounds, the Kondo temperature T_K and the ground state degeneracy play important roles in the thermodynamic and transport properties [253]. The peak observed in $\chi(T)$ and $C_m(T)$ may be a result of the orbital effect of total angular momentum J larger than 1/2, as proposed by Coqblin and Schrieffer (C-S) [254]. In this model the multiplicity $N = 2J + 1$ of the total angular momentum plays an important role in stabilizing the Kondo state and raising the Kondo temperature T_K. The Kondo impurity problem in the Coqblin-Schrieffer model has been numerically calculated for several total angular momenta by Rajan [243]. Generally specific heat and magnetic susceptibility show a maximum for $N > 2$ and the temperature of the maximum is related to T_K [243]. The low temperature C_m curves for $x = 0.05$ and 0.34 are compared with Rajan's calculations as shown in Fig. 6.13(a). The maximum in C_m for $x = 0.05$ falls between the $J = 1/2$ and 3/2 curves, indicating that the Kondo effect combined with CEF splitting scheme will not allow this very simple type of analysis. By considering the entropy and the large C_m/T value at low temperatures it is expected that $T_K < \Delta$ for all x, where Δ is the energy gap between the ground and first excited states of CEF levels. Based on this, for $x = 0.05$, it is reasonable to assume that the maximum in C_m simply reflects the Kondo effect, with the doubly degenerate case corresponding to $N = 2$. For $x = 0.34$, the two extrema in the specific heat data associated with Kondo effects on the CEF ground states of both the $6d$ and $2a$ sites could be expected. However, only one broad peak structure is developed. We thus expect that a single broad maximum is produced by merging more than one peak structure associated with different Kondo temperatures for the $2a$ and $6d$ sites. A similar analysis can be made by performing a fit to the magnetic susceptibility over a wide temperature range. As shown in Fig. 6.13(b) the magnetic susceptibility curves for both $x = 0.05$

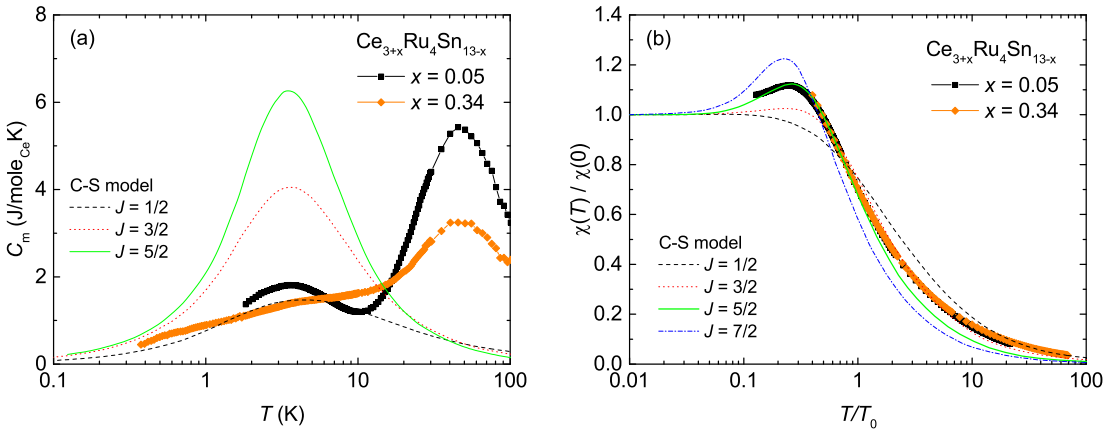

Figure 6.13: (a) C_m for $x = 0.05$ and 0.34. Lines represent the prediction of the Coqblin-Schrieffer model for $J = 1/2$, $3/2$, and $5/2$ and $T_0 = 5$, 8, and 12 K, respectively. (b) $\chi(T)/\chi(0)$ for $x = 0.05$ and 0.34. Lines represent the prediction of the Coqblin-Schrieffer model for $J = 1/2$, $3/2$, $5/2$, and $7/2$.

and $x = 0.34$ cannot be explained by the C-S model with any J value over the entire temperature range measured. Therefore, we compare the height of the maximum with the C-S model. When the magnetic susceptibility for $x = 0.05$ is scaled with $\chi_0 = 0.031$ emu/mole and $T_0 = 14$ K, the broad maximum can be described by the $J = 5/2$ case, implying that the state with $N = 6$ is Kondo screened and $T_K > \Delta$. However, in the high temperature regime, the susceptibility curve follows the C-S model with $J = 3/2$. This is in contrast with the magnetic specific heat analysis. Interestingly, when the susceptibility curve for $x = 0.34$ is scaled with $\chi_0 = 0.068$ emu/mole and $T_0 = 4.5$ K, it follows the $\chi(T)$ curve of $x = 0.05$, implying that there might be a maximum below 1.8 K in $\chi(T)$ for $x = 0.34$. Given the above analysis, the CEF splitting scheme with doublet and quartet ground states will not allow this very simple type of analysis with the Kondo interaction. It has to be noted that the maximum in $\chi(T)$ and the metamagnetic-like transition can be developed with Kramers doublet ($N = 2$) as evidenced from $CeRu_2Si_2$ [251], where the anisotropic hybridization is suggested to be the origin [255, 256]. Further studies are necessary to understand the origin of the maximum in $\chi(T)$ and the metamagnetic-like transition in $M(H)$ for $x = 0.05$.

6.3.10 Other perspectives on physical properties observed in $Ce_{3+x}Ru_4Sn_{13-x}$

The electrical resistivity, specific heat, and magnetic susceptibility data suggest that $Ce_{3+x}Ru_4Sn_{13-x}$ compounds are heavy fermion Kondo lattice systems with complex CEF schemes. However, it shouldn't be discarded the possibilities that the low temperature physical properties result from magnetic fluctuations, disorder, or spin glass. Neutron scattering and μSR studies on $CeRuSn_3$ suggest that the low temperature broad peak is related to short-range magnetic fluctuations or spin-glass dynamics [230, 231]. Although no hysteresis is observed for all

samples in this study, the low temperature specific heat and magnetic susceptibility may result from the spin glass. The key ingredients for spin glass behavior are frustration and disorder (randomness). When Ce atoms at $6d$ site are considered, the Ce sublattice forms icosahedra, but distorted. Within each icosahedron, the Ce atoms are located on isosceles triangles with a distance ∼4.86 Å from the nearest Ce atoms and ∼5.95 Å from the next nearest Ce atoms. When three Ce-spins are placed on isosceles triangle (not placed on equilateral triangle), the frustration is not expected in this system. Therefore, the spin glass behavior observed in earlier studies might be caused by the disorder.

With regard to the disorder, the formation of superstructure mostly related to the distorted icosahedra in the $Yb_3Rh_4Sn_{13}$-type structure is evidenced [257] and the Ce occupancies at both the $6d$ and $2a$ sites are critical to interpret the physical properties on $Ce_{3+x}Ru_4Sn_{13-x}$ system [230]. In addition, the electrical resistivity of $Ce_3Co_4Sn_{13}$ [252] and $Ce_3Rh_4Sn_{13}$ [258] show anomalous behavior below the structural phase transition which is due to a small distortion of trigonal Sn prisms around transition metal ions. Interestingly, the Weyl semimetal state is suggested in these compounds, where the crystal structure becomes a chiral space group $I2_13$ below the structural phase transition [259, 224]. Although thermodynamic and transport property measurements of $Ce_{3+x}Ru_4Sn_{13-x}$ indicate no noticeable structural phase transition below 300 K, a weak superlattice formation shouldn't be neglected because a polycrystalline $Ce_3Ru_4Sn_{13}$ sample shows signs of a weak structural change in XRD and XPS measurements [236].

6.4 Summary

We have grown single crystals of $Ce_{3+x}Ru_4Sn_{13-x}$ ($0.05 \leq x \leq 0.34$) with varying Ce/Sn loading compositions, and investigated their physical properties through measurements of EDX, powder X-ray diffraction, electrical resistivity, magnetization, and specific heat. The compound $La_{3.65}Ru_4Sn_{12.35}$ shows typical metallic behavior down to 2.1 K and undergoes the BCS-type superconducting transition below 2.1 K. For $Ce_{3+x}Ru_4Sn_{13-x}$, the magnetic susceptibility measurements show that the $4f$-electrons of the Ce^{3+}-ions are well localized. The electrical resistivity of $Ce_{3+x}Ru_4Sn_{13-x}$ follows typical Kondo lattice behavior. Upon increasing x from 0.05 to 0.34, the absolute value of the resistivity increases and the observed minimum temperature moves to higher temperature. While the structural disorder can lead to a significant change in resistivity value as well as the observed temperature dependence, it cannot explain the Kondo lattice behavior observed in this study. At low temperatures, magnetic susceptibility and specific heat show a pronounced broad maximum at $T \sim 3.5$ K for compounds with small x, and the broad maximum disappears as x increases. The maximum cannot be explained by the very simple type of analysis with the Kondo interaction in conjunction with CEF effects. To understand the observed thermodynamic and transport

properties of the $Ce_{3+x}Ru_4Sn_{13-x}$ system, the disordered Ce ions at the $2a$ site and fully ordered Ce ions at the $6d$ site must be considered.

Chapter 7

Summary

This thesis has undertaken a comprehensive exploration of four distinct systems: $CeCd_3P_3$, RV_6Sn_6, RNi_4Cd and $Ce_{3+x}Ru_4Sn_{13-x}$. Each of these systems possesses unique characteristics, providing insights into the effects of magnetic frustration and low-carrier density on $4f$ magnetic systems.

Both $CeCd_3P_3$ and RV_6Sn_6 (R = Gd−Tm) crystallize into a hexagonal structure, where the rare-earth ions form hexagonal layers separated by non-magnetic layers. This structural arrangement leads to strong magnetic anisotropy due to the closer proximity of the nearest neighboring rare-earth ions within the plane compared to along the c-axis, resulting in the $4f$ moments being pseudo-2D-layered systems. $CeCd_3P_3$ is a low-carrier density metallic system exhibiting an emergent spin-orbit entangled doublet ground state at low temperatures, effectively behaving as a spin-1/2 system. Despite exhibiting antiferromagnetic ordering below T_N of 0.41 K, the significant electronic specific heat above T_N suggests the presence of magnetic frustration. Interestingly, $CeCd_3P_3$ deviates from the typical behaviour observed in Kondo lattice systems, indicating negligible hybridization with conduction electrons. This observation highlights the importance of carrier density in heavy fermion systems and emphasizes the role it plays in complex magnetic phenomena.

In contrast, RV_6Sn_6 presents sufficient carrier density expected of a typical metal. The heavy rare-earth ions in RV_6Sn_6 also exhibit strong magnetic anisotropy, with an easy magnetization direction along the c-axis for R = Tb−Ho and in the ab-plane for R = Er and Tm. This behaviour is a consequence of the crystal electric field effects on the rare-earth ions. The magnetic ordering temperature for R = Gd is $T_N = 5$ K, and it decreases as expected according to the de Gennes factor, which is an indication of RKKY exchange interactions. When an anisotropic RKKY interaction, together with the Dzyaloshinskii–Moriya interaction, is considered, $4f$ moments on geometrically frustrated lattices are known to form stabilized chiral magnetic structures, such as skyrmions. Hence, building upon the knowledge gained from RV_6Sn_6, the discovery of more metallic systems with $4f$ moments on geometrically frustrated lattices is necessary to understand the effects of geometrically frustrated lattice on exotic phenomena associated with various spin structures.

The magnetic properties of RNi$_4$Cd, as well as the previously reported RT_4X, were studied regarding their geometrical frustration. In RT_4X, R atoms form a face-centred cubic lattice. The $RT4X$ family comprises several isostructural compounds with varying T_N and θ_p values upon substitution in the R, T and X positions, enabling exploration of the relationship between parameters affecting magnetic properties. It was observed that θ_p in GdT_4X was suppressed by strong antiferromagnetism with lattice contraction, except for GdCu$_4$Pd. The suggested magnetic frustration in RCu$_4$In, where θ_p is much larger than T_N ($f > 10$), is due to the low-carrier densities. For metallic GdT_4X, the frustration parameter is near 1, and the variation of θ_p is associated with the distance between rare-earth atoms and the number of electrons contributing to the conduction band. It was observed that substituting different X in GdCu$_4X$ may cause θ_p to change from a large negative to a large positive value due to the completely filled d-shell in Cu and the progressive removal of the s-electron in X, which was accompanied by a decrease in the lattice parameter. In contrast, the incomplete d-shell in Ni-based GdNi$_4X$ resulted in a trivial θ_p, necessitating further investigation into the role of d-electrons in the $4f$–$4f$ exchange interaction manifested by θ_p. When substituting R from Gd to Tm in RNi$_4$Cd, we observed that θ_p remained close to zero. Based on this finding, we anticipate that θ_p of YbNi$_4$Cd would also be close to zero if no other contributions existed. However, the moderate value of θ_p (-17 K) observed in contrast to T_N (1 K) in YbNi$_4$Cd likely resulted from the hybridization between the $4f$ and conduction electrons, thereby eliminating geometrical frustration as a driving factor for the large $|\theta_p/T_N|$. At this point, it is premature to conclude that there is negligible magnetic frustration in YbNi$_4$Cd. Drawing from studies of the heavy rare-earth series, it is possible that the d-electrons contributing to the conduction band in Ni-based RNi$_4X$ compounds may have played a role in the unconventional quantum criticality observed in YbNi$_4$Cd. Therefore, it is essential to find supporting theoretical and experimental evidence to validate this hypothesis.

Finally, to gain insights into the anomalous magnetic behaviour exhibited by $Ce_{3+x}Ru_4Sn_{13-x}$, the ground state of this compound was investigated, particularly focusing on the role of low-carrier density. The presence of a broad maximum in specific heat is a common characteristic observed not only in this system but also in the isostructural $R_{3+x}T_4X_{13-x}$ compounds (where R = Ce and Yb, T = Ru and Ir and X = Ge and Sn). In $Ce_{3+x}Ru_4Sn_{13-x}$, Ce ions occupy the $6d$ and $2a$ sites, with full and mixed occupancies, respectively. The initial loading compositions of Ce and Sn can control the occupancy of Ce at the $2a$ site, which significantly influences the physical properties of the compound. The electrical resistivity of $Ce_{3+x}Ru_4Sn_{13-x}$ undergoes a transition from Kondo lattice behaviour to semiconductor-like behaviour as x increases. Moreover, the broad maximum observed in magnetic susceptibilities and specific heat at around 3 K disappears with increasing x. Our analysis indicates that these broad peaks can be qualitatively explained by considering the Kondo interaction and CEF degeneracy for any J. Notably, the slight discrepancy between the calculated and

observed peaks suggests that the observed broad peak may arise from the merging of the two peak structures associated with different Kondo temperatures for the $2a$ and $6d$ sites. The absence of clear long-range magnetic ordering in these systems could be attributed to weak RKKY interactions due to low-carrier density, but it also raises the possibility of Ce experiencing relatively different Kondo interactions at these Ce sites. Hence, the $R_{3+x}T_4X_{13-x}$ system, where R = Ce and Yb, exhibits complex magnetic properties influenced by the relative energy scales of the RKKY and Kondo interactions, which are further affected by low-carrier density and disorder at the $2a$ site. Further experimental investigations are necessary to fully comprehend the nature of magnetism arising from the $6d$ and $2a$ sites, particularly by utilizing the S-state of Gd. For instance, investigating $Gd_{3+x}T_4X_{13-x}$ can help eliminate the influence of both the CEF and Kondo effects.

Based on the findings obtained from the intermetallic systems studied in this thesis, it was observed that the effect of the geometrically frustrated lattice on the magnetic properties of metallic systems was not as pronounced as in the frustrated $4f$ lattices of insulators. This is likely due to the conduction electrons playing a role in stabilizing the ordering of $4f$ moments over long ranges. Clear indications of magnetic frustration are challenging to observe in high-carrier-density metals, as seen in the cases of $R\mathrm{V_6Sn_6}$ and $R\mathrm{Ni_4Cd}$. We also observed a weakening of RKKY interactions, destabilizing the long-range coupling of $4f$ moments in $\mathrm{Ce_{3+x}Ru_4Sn_{13-x}}$, as well as the absence of Kondo interactions in $\mathrm{CeCd_3P_3}$ when there were few available carriers. Therefore, a more comprehensive phase diagram accounting for lattice geometry and carrier density is required for heavy fermion systems to generalize these observations.

Bibliography

[1] J. Lee, A. Rabus, N. R. Lee-Hone, D. M. Broun, and E. Mun. The two-dimensional metallic triangular lattice antiferromagnet $CeCd_3P_3$. *Physical Review B*, 99(24):245159, 2019.

[2] S. R. Dunsiger, J. Lee, J. E. Sonier, and E. D. Mun. Long-range magnetic order in the anisotropic triangular lattice system $CeCd_3As_3$. *Physical Review B*, 102(6):064405, 2020.

[3] J. Lee and E. Mun. Anisotropic magnetic property of single crystals RV_6Sn_6 (R = Y, Gd - Tm, Lu). *Phys. Rev. Materials*, 6:083401, 2022.

[4] B. K. Rai, I. W. H. Oswald, W. Ban, C-L. Huang, V. Loganathan, A. M. Hallas, M. N. Wilson, G. M. Luke, L. Harriger, Q. Huang, et al. Low-carrier density and fragile magnetism in a Kondo lattice system. *Physical Review B*, 99(8):085120, 2019.

[5] J. Lee and E. Mun. Physical properties of $Ce_{3+x}Ru_4Sn_{13-x}$ single crystals. *Physical Review Materials*, 6(4):043401, 2022.

[6] S. Blundell. Magnetism in condensed matter, 2003.

[7] E. Bauer and M. Rotter. Magnetism of complex metallic alloys: Crystalline electric field effects. In *Properties and Applications of Complex Intermetallics*, pages 183–248. World Scientific, 2010.

[8] A. J. Freeman and R. E. Watson. Theoretical investigation of some magnetic and spectroscopic properties of rare-earth ions. *Physical Review*, 127(6):2058, 1962.

[9] W. Nolting and A. Ramakanth. *Quantum theory of magnetism*. Springer Science & Business Media, 2009.

[10] J. Jensen and A. R. Mackintosh. *Rare earth magnetism*. Clarendon Press Oxford, 1991.

[11] Y.-L. Wang. Crystal-field effects of paramagnetic curie temperature. *Physics Letters A*, 35(5):383–384, 1971.

[12] M. A. Ruderman and C. Kittel. Indirect exchange coupling of nuclear magnetic moments by conduction electrons. *Physical Review*, 96(1):99, 1954.

[13] T. Kasuya. A theory of metallic ferro-and antiferromagnetism on Zener's model. *Progress of theoretical physics*, 16(1):45–57, 1956.

[14] K. Yosida. Magnetic properties of Cu-Mn alloys. *Physical Review*, 106(5):893, 1957.

[15] R. E. Watson, S. Koide, M. Peter, and A. J. Freeman. Effective Conduction-Electron-Local-Moment Exchange Interaction in Metals: Rare-Earth Interband Mixing. *Physical Review*, 139(1A):A167, 1965.

[16] R. E. Watson, Arthur J. Freeman, and S. Koide. Role of interband mixing in exchange coupling and conduction-electron polarization in metals. *Physical Review*, 186(3):625, 1969.

[17] K. N. Taylor and M. I. Darby. Physics of Rare Earth Solids. 1972.

[18] P. G. De Gennes. Interactions indirectes entre couches 4f dans les métaux de terres rares. *Journal de Physique et le Radium*, 23(8-9):510–521, 1962.

[19] J. Kondo. Resistance minimum in dilute magnetic alloys. *Progress of theoretical physics*, 32(1):37–49, 1964.

[20] A. A. Abrikosov. Electron scattering on magnetic impurities in metals and anomalous resistivity effects. *Physics Physique Fizika*, 2(1):5, 1965.

[21] P. W. Anderson. A poor man's derivation of scaling laws for the Kondo problem. *Journal of Physics C: Solid State Physics*, 3(12):2436, 1970.

[22] K. G. Wilson. The renormalization group: Critical phenomena and the Kondo problem. *Reviews of modern physics*, 47(4):773, 1975.

[23] A. Sumiyama, Y. Oda, H. Nagano, Y. Ōnuki, K. Shibutani, and T. Komatsubara. Coherent Kondo State in a Dense Kondo Substance: $Ce_xLa_{1-x}Cu_6$. *Journal of the Physical Society of Japan*, 55(4):1294–1304, 1986.

[24] P. Misra. Heavy-fermion systems. 2007.

[25] B. Cornut and B. Coqblin. Influence of the crystalline field on the kondo effect of alloys and compounds with cerium impurities. *Physical Review B*, 5(11):4541, 1972.

[26] H.-U. Desgranges. Crystal fields and kondo effect: Specific heat for cerium compounds. *Physica B: Condensed Matter*, 454:135–140, 2014.

[27] H.-U. Desgranges. Crystal fields and kondo effect: New results for the magnetic susceptibility. *Physica B: Condensed Matter*, 473:93–100, 2015.

[28] S. Doniach. The kondo lattice and weak antiferromagnetism. *physica B+ C*, 91:231–234, 1977.

[29] G. H. Wannier. Antiferromagnetism. the triangular ising net. *Physical Review*, 79(2):357, 1950.

[30] A. P. Ramirez. Strongly geometrically frustrated magnets. *Annual Review of Materials Science*, 24(1):453–480, 1994.

[31] L. Balents. Spin liquids in frustrated magnets. *Nature*, 464(7286):199–208, 2010.

[32] C. Broholm, R. J. Cava, S. A. Kivelson, D. G. Nocera, M. R. Norman, and T. Senthil. Quantum spin liquids. *Science*, 367(6475):eaay0668, 2020.

[33] S. Yamashita, Y. Nakazawa, M. Oguni, Y. Oshima, H. Nojiri, Y. Shimizu, K. Miyagawa, and K. Kanoda. Thermodynamic properties of a spin-1/2 spin-liquid state in a κ-type organic salt. *Nature Physics*, 4(6):459–462, 2008.

[34] M. R. Norman. Colloquium: Herbertsmithite and the search for the quantum spin liquid. *Reviews of Modern Physics*, 88(4):041002, 2016.

[35] A. Banerjee, Ji. Yan, J. Knolle, C. A. Bridges, M. B. Stone, M. D. Lumsden, D. G. Mandrus, D. A. Tennant, R. Moessner, and S. E. Nagler. Neutron scattering in the proximate quantum spin liquid α-$RuCl_3$. *Science*, 356(6342):1055–1059, 2017.

[36] J. A. M. Paddison, M. Daum, Z. Dun, G. Ehlers, Y. Liu, M. B. Stone, H. Zhou, and M. Mourigal. Continuous excitations of the triangular-lattice quantum spin liquid $YbMgGaO_4$. *Nature Physics*, 13(2):117–122, 2017.

[37] J. G. Rau and M. J. P. Gingras. Frustrated quantum rare-earth pyrochlores. *Annual Review of Condensed Matter Physics*, 10:357–386, 2019.

[38] Y. Tokura and N. Kanazawa. Magnetic skyrmion materials. *Chemical Reviews*, 121(5):2857–2897, 2020.

[39] V. Fritsch, J. D. Thompson, J. L. Sarrao, H.-A. Krug von Nidda, R. M. Eremina, and A. Loidl. Correlation between magnetic frustration and electrical conductivity in $R\mathrm{InCu}_4$ compounds (R = Gd- Tm). *Physical review B*, 73(9):094413, 2006.

[40] H. Nakamura, N. Kim, M. Shiga, R. Kmiec, K. Tomala, E. Ressouche, J. P. Sanchez, and B. Malaman. The partially disordered state of the frustrated face-centred cubic antiferromagnet. *Journal of Physics: Condensed Matter*, 11(4):1095, 1999.

[41] S. A. M. Mentink, A. Drost, G. J. Nieuwenhuys, E. Frikkee, A. A. Menovsky, and J. A. Mydosh. Magnetic Ordering and Frustration in Hexagonal UNi_4B. *Physical review letters*, 73(7):1031, 1994.

[42] O. Stockert, J.-U. Hoffmann, M. Mühlbauer, A. Senyshyn, M. M. Koza, A. A. Tsirlin, F. M. Wolf, S. Bachus, P. Gegenwart, R. Movshovich, et al. Magnetic frustration in a metallic fcc lattice. *Physical Review Research*, 2(1):013183, 2020.

[43] Y. Tokiwa, J. J. Ishikawa, S. Nakatsuji, and P. Gegenwart. Quantum criticality in a metallic spin liquid. *Nature materials*, 13(4):356–359, 2014.

[44] P. Gegenwart, F. Steglich, C. Geibel, and M. Brando. Novel types of quantum criticality in heavy-fermion systems. *The European Physical Journal Special Topics*, 224(6):975–996, 2015.

[45] T. Senthil, S. Sachdev, and M. Vojta. Fractionalized fermi liquids. *Physical review letters*, 90(21):216403, 2003.

[46] T. Senthil, M. Vojta, and S. Sachdev. Weak magnetism and non-fermi liquids near heavy-fermion critical points. *Physical Review B*, 69(3):035111, 2004.

[47] M. Vojta. From itinerant to local-moment antiferromagnetism in kondo lattices: Adiabatic continuity versus quantum phase transitions. *Physical Review B*, 78(12):125109, 2008.

[48] P. Coleman and A. H. Nevidomskyy. Frustration and the kondo effect in heavy fermion materials. *Journal of Low Temperature Physics*, 161(1):182–202, 2010.

[49] E. Mun, S. L. Bud'ko, C. Martin, H. Kim, M. A. Tanatar, J.-H. Park, T. Murphy, G. M. Schmiedeshoff, N. Dilley, R. Prozorov, et al. Magnetic-field-tuned quantum criticality of the heavy-fermion system YbPtBi. *Physical Review B*, 87(7):075120, 2013.

[50] Y. Tokiwa, M. Garst, P. Gegenwart, S. L. Bud'ko, and P. C. Canfield. Quantum bicriticality in the heavy-fermion metamagnet YbAgGe. *Physical review letters*, 111(11):116401, 2013.

[51] S. Nakatsuji, Y. Machida, Y. Maeno, T. Tayama, T. Sakakibara, J. Van Duijn, L. Balicas, J. N. Millican, R. T. Macaluso, and Julia Y. Chan. Metallic spin-liquid behavior of the geometrically frustrated Kondo lattice $Pr_2Ir_2O_7$. *Physical review letters*, 96(8):087204, 2006.

[52] J. Custers, P. Gegenwart, C. Geibel, F. Steglich, P. Coleman, and S. Paschen. Evidence for a non-Fermi-liquid phase in Ge-substituted $YbRh_2Si_2$. *Physical Review Letters*, 104(18):186402, 2010.

[53] S. Nakatsuji, K. Kuga, Y. Machida, T. Tayama, T. Sakakibara, Y. Karaki, H. Ishimoto, S. Yonezawa, Y. Maeno, E. Pearson, et al. Superconductivity and quantum criticality in the heavy-fermion system β-$YbAlB_4$. *Nature physics*, 4(8):603–607, 2008.

[54] A. N. Tahvildar-Zadeh, M. Jarrell, and J. K. Freericks. Protracted screening in the periodic anderson model. *Physical Review B*, 55(6):R3332, 1997.

[55] J. M. Lawrence, P. S. Riseborough, C. H. Booth, J. L. Sarrao, J. D. Thompson, and R. Osborn. Slow crossover in $YbXCu_4$ (X = Ag, Cd, In, Mg, Tl, Zn) intermediate-valence compounds. *Physical Review B*, 63(5):054427, 2001.

[56] Y. Luo, F. Ronning, N. Wakeham, X. Lu, T. Park, Z.-A. Xu, and J. D. Thompson. Pressure-tuned quantum criticality in the antiferromagnetic Kondo semimetal $CeNi_{2-\delta}As_2$. *Proceedings of the National Academy of Sciences*, 112(44):13520–13524, 2015.

[57] J. Chen, Z. Wang, Y. Li, C. Feng, J. Dai, Z. Xu, and Q. Si. Heavy fermion quantum criticality at dilute carrier limit in $CeNi_{2-\delta}(As_{1-x}P_x)_2$. *Scientific Reports*, 9(1):1–10, 2019.

[58] Z. Fisk, J. L. Sarrao, J. D. Thompson, D. Mandrus, M. F. Hundley, A. Miglori, B. Bucher, Z. Schlesinger, G. Aeppli, E. Bucher, et al. Kondo insulators. *Physica B: Condensed Matter*, 206:798–803, 1995.

[59] P. S. Riseborough. Heavy fermion semiconductors. *Advances in Physics*, 49(3):257–320, 2000.

[60] S. Dzsaber, L. Prochaska, A. Sidorenko, G. Eguchi, R. Svagera, M. Waas, A. Prokofiev, Q. Si, and S. Paschen. Kondo insulator to semimetal transformation tuned by spin-orbit coupling. *Physical Review Letters*, 118(24):246601, 2017.

[61] M. Dzero, K. Sun, V. Galitski, and P. Coleman. Topological kondo insulators. *Physical review letters*, 104(10):106408, 2010.

[62] X.-Y. Feng, H. Zhong, J. Dai, and Q. Si. Dirac-kondo semimetals and topological kondo insulators in the dilute carrier limit. *arXiv preprint arXiv:1605.02380*, 2016.

[63] H.-H. Lai, S. E. Grefe, S. Paschen, and Q. Si. Weyl–kondo semimetal in heavy-fermion systems. *Proceedings of the National Academy of Sciences*, 115(1):93–97, 2018.

[64] X.-Y. Feng, J. Dai, C.-H. Chung, and Q. Si. Competing topological and kondo insulator phases on a honeycomb lattice. *Physical Review Letters*, 111(1):016402, 2013.

[65] P. C Canfield and Z. Fisk. Growth of single crystals from metallic fluxes. *Philosophical magazine B*, 65(6):1117–1123, 1992.

[66] C. Lacroix, P. Mendels, and F. Mila. *Introduction to frustrated magnetism: materials, experiments, theory*, volume 164. Springer Science & Business Media, 2011.

[67] O. A. Starykh. Unusual ordered phases of highly frustrated magnets: a review. *Reports on Progress in Physics*, 78(5):052502, 2015.

[68] P. A. Lee. An end to the drought of quantum spin liquids. *Science*, 321(5894):1306–1307, 2008.

[69] L. Savary and L. Balents. Quantum spin liquids: a review. *Reports on Progress in Physics*, 80(1):016502, 2016.

[70] Yi. Zhou, K. Kanoda, and T.-K. Ng. Quantum spin liquid states. *Reviews of Modern Physics*, 89(2):025003, 2017.

[71] N. D. Mermin and H. Wagner. Absence of ferromagnetism or antiferromagnetism in one-or two-dimensional isotropic heisenberg models. *Physical Review Letters*, 17(22):1133, 1966.

[72] P. W. Anderson. Resonating valence bonds: A new kind of insulator? *Materials Research Bulletin*, 8(2):153–160, 1973.

[73] S. Teitel and C. Jayaprakash. Phase transtions in frustrated two-dimensional xy models. *Physical Review B*, 27(1):598, 1983.

[74] S. Miyashita and H. Shiba. Nature of the phase transition of the two-dimensional antiferromagnetic plane rotator model on the triangular lattice. *Journal of the Physical Society of Japan*, 53(3):1145–1154, 1984.

[75] H. Kawamura and S. Miyashita. Phase transition of the two-dimensional heisenberg antiferromagnet on the triangular lattice. *Journal of the Physical Society of Japan*, 53(12):4138–4154, 1984.

[76] D. H. Lee, J. D. Joannopoulos, J. W. Negele, and D. P. Landau. Discrete-symmetry breaking and novel critical phenomena in an antiferromagnetic planar (xy) model in two dimensions. *Physical review letters*, 52(6):433, 1984.

[77] M. Yosefin and E. Domany. Phase transitions in fully frustrated spin systems. *Physical Review B*, 32(3):1778, 1985.

[78] D. H. Lee, J. D. Joannopoulos, J. W. Negele, and D. P. Landau. Symmetry analysis and monte carlo study of a frustrated antiferromagnetic planar (xy) model in two dimensions. *Physical Review B*, 33(1):450, 1986.

[79] J. Knolle and J. Knolle. Dynamic spin correlations: Mapping to a quantum quench. *Dynamics of a Quantum Spin Liquid*, pages 37–57, 2016.

[80] W.-J. Hu, S.-S. Gong, W. Zhu, and D. N. Sheng. Competing spin-liquid states in the spin-1 2 heisenberg model on the triangular lattice. *Physical Review B*, 92(14):140403, 2015.

[81] Y.-D. Li, X. Wang, and G. Chen. Anisotropic spin model of strong spin-orbit-coupled triangular antiferromagnets. *Physical Review B*, 94(3):035107, 2016.

[82] Y. Iqbal, W.-J. Hu, R. Thomale, D. Poilblanc, and F. Becca. Spin liquid nature in the Heisenberg J_1-J_2 triangular antiferromagnet. *Physical Review B*, 93(14):144411, 2016.

[83] S.-S. Gong, W. Zhu, J.-X. Zhu, D. N. Sheng, and K. Yang. Global phase diagram and quantum spin liquids in a spin-1 2 triangular antiferromagnet. *Physical Review B*, 96(7):075116, 2017.

[84] Z. Zhu, P. A. Maksimov, S. R. White, and A. L. Chernyshev. Topography of spin liquids on a triangular lattice. *Physical review letters*, 120(20):207203, 2018.

[85] J. G. Rau and M. J. P. Gingras. Frustration and anisotropic exchange in ytterbium magnets with edge-shared octahedra. *Physical Review B*, 98(5):054408, 2018.

[86] H. Kawamura and S. Miyashita. Phase transition of the heisenberg antiferromagnet on the triangular lattice in a magnetic field. *Journal of the Physical Society of Japan*, 54(12):4530–4538, 1985.

[87] A. V. Chubukov and D. I. Golosov. Quantum theory of an antiferromagnet on a triangular lattice in a magnetic field. *Journal of Physics: Condensed Matter*, 3(1):69, 1991.

[88] L. Seabra, T. Momoi, P. Sindzingre, and N. Shannon. Phase diagram of the classical heisenberg antiferromagnet on a triangular lattice in an applied magnetic field. *Physical Review B*, 84(21):214418, 2011.

[89] D. Yamamoto, G. Marmorini, and I. Danshita. Quantum Phase Diagram of the Triangular-Lattice X X Z Model in a Magnetic Field. *Physical Review Letters*, 112(12):127203, 2014.

[90] B. Schmidt and P. Thalmeier. Frustrated two dimensional quantum magnets. *Physics Reports*, 703:1–59, 2017.

[91] A. Ochiai, T. Inukai, T. Matsumura, A. Oyamada, and K. Katoh. Spin Gap State of $S = 1/\ 2$ Heisenberg Antiferromagnet $YbAl_3C_3$. *Journal of the Physical Society of Japan*, 76(12):123703–123703, 2007.

[92] Y. Kato, M. Kosaka, H.i Nowatari, Y. Saiga, A. Yamada, T. Kobiyama, S. Katano, K. Ohoyama, H. S. Suzuki, N. Aso, et al. Spin-singlet ground state in the two-dimensional frustrated triangular lattice: $YbAl_3C_3$. *Journal of the Physical Society of Japan*, 77(5):053701–053701, 2008.

[93] A. Ochiai, K. Hara, F. Kikuchi, T. Inukai, E. Matsuoka, H. Onodera, S. Nakamura, T. Nojima, and K. Katoh. Quantum spin system in f-electron compounds-$YbAl_3C_3$ and its related compounds. In *Journal of Physics: Conference Series*, volume 200, page 022040. IOP Publishing, 2010.

[94] K. Hara, S. Matsuda, E. Matsuoka, K. Tanigaki, A. Ochiai, S. Nakamura, T. Nojima, and K. Katoh. Quantum spin state in the rare-earth compound $YbAl_3C_3$. *Physical Review B*, 85(14):144416, 2012.

[95] Y. Li, H. Liao, Z. Zhang, S. Li, F. Jin, L. Ling, L. Zhang, Y. Zou, L. Pi, Z. Yang, et al. Gapless quantum spin liquid ground state in the two-dimensional spin-1/2 triangular antiferromagnet $YbMgGaO_4$. *Scientific reports*, 5(1):16419, 2015.

[96] Y. Li, G. Chen, W. Tong, L. Pi, J. Liu, Z. Yang, X. Wang, and Q. Zhang. Rare-earth triangular lattice spin liquid: a single-crystal study of $YbMgGaO_4$. *Physical review letters*, 115(16):167203, 2015.

[97] Y. Shen, Y.-D. Li, H. Wo, Y. Li, S. Shen, B. Pan, H. C. Wang, Q.and Walker, P. Steffens, M. Boehm, et al. Evidence for a spinon fermi surface in a triangular-lattice quantum-spin-liquid candidate. *Nature*, 540(7634):559–562, 2016.

[98] Y. Li, D. Adroja, P. K. Biswas, P. J. Baker, Q. Zhang, J. Liu, A. A Tsirlin, P. Gegenwart, and Q. Zhang. Muon spin relaxation evidence for the U(1) quantum spin-liquid ground state in the triangular antiferromagnet $YbMgGaO_4$. *Physical review letters*, 117(9):097201, 2016.

[99] M. Baenitz, P. Schlender, J. Sichelschmidt, Y. A. Onykiienko, Z. Zangeneh, K. M. Ranjith, R. Sarkar, L. Hozoi, H. C. Walker, J.-C. Orain, et al. $NaYbS_2$: A planar spin-1 2 triangular-lattice magnet and putative spin liquid. *Physical Review B*, 98(22):220409, 2018.

[100] J. Sichelschmidt, P. Schlender, B. Schmidt, M. Baenitz, and T. Doert. Electron spin resonance on the spin-1/2 triangular magnet $NaYbS_2$. *Journal of Physics: Condensed Matter*, 31(20):205601, 2019.

[101] S. Higuchi, Y. Noshima, N. Shirakawa, M. Tsubota, and J. Kitagawa. Optical, transport and magnetic properties of new compound $CeCd_3P_3$. *Materials Research Express*, 3(5):056101, 2016.

[102] Y. Q. Liu, S. J. Zhang, J. L. Lv, S. Su, T. Dong, G. Chen, and N. L. Wang. Revealing a Triangular Lattice Ising Antiferromagnet in a Single-Crystal $CeCd_3As_3$. *arXiv preprint arXiv:1612.03720*, 2016.

[103] G. R. Stewart. Heavy-fermion systems. *Reviews of Modern Physics*, 56(4):755, 1984.

[104] Q. Si. Quantum criticality and global phase diagram of magnetic heavy fermions. *physica status solidi (b)*, 247(3):476–484, 2010.

[105] P. Coleman. Quantum criticality and novel phases: A panel discussion. *physica status solidi (b)*, 247(3):506–512, 2010.

[106] J. Custers, K. A. Lorenzer, M. Müller, A. Prokofiev, A. Sidorenko, H. Winkler, A. M. Strydom, Y. Shimura, T. Sakakibara, R. Yu, et al. Destruction of the Kondo effect in the cubic heavy-fermion compound $Ce_3Pd_{20}Si_6$. *Nature materials*, 11(3):189–194, 2012.

[107] M. S. Kim and M. C. Aronson. Spin liquids and antiferromagnetic order in the Shastry-Sutherland-lattice compound Yb_2Pt_2Pb. *Physical review letters*, 110(1):017201, 2013.

[108] V. Fritsch, N. Bagrets, G. Goll, W. Kittler, M. J. Wolf, K. Grube, C.-L. Huang, and H. v. Löhneysen. Approaching quantum criticality in a partially geometrically frustrated heavy-fermion metal. *Physical Review B*, 89(5):054416, 2014.

[109] A. T. Nientiedt and W. Jeitschko. The Series of Rare Earth Zinc Phosphides $R\mathrm{Zn}_3\mathrm{P}_3$ (R = Y, La–Nd, Sm, Gd–Er) and the Corresponding Cadmium Compound $\mathrm{PrCd}_3\mathrm{P}_3$. *Journal of Solid State Chemistry*, 146(2):478–483, 1999.

[110] S. S. Stoyko and A. Mar. Ternary Rare-Earth Arsenides $RE\mathrm{Zn}_3\mathrm{As}_3$ (RE = La–Nd, Sm) and $RE\mathrm{Cd}_3\mathrm{As}_3$ (RE = La–Pr). *Inorganic Chemistry*, 50(21):11152–11161, 2011.

[111] J. Banda, B. K. Rai, H. Rosner, E. Morosan, C. Geibel, and M. Brando. Crystalline electric field of Ce in trigonal symmetry: $\mathrm{CeIr}_3\mathrm{Ge}_7$ as a model case. *Physical Review B*, 98(19):195120, 2018.

[112] A. Yamada, N. Hara, K. Matsubayashi, K. Munakata, C. Ganguli, A. Ochiai, T. Matsumoto, and Y. Uwatoko. Effect of pressure on the electrical resistivity of $\mathrm{CeZn}_3\mathrm{P}_3$. In *Journal of Physics: Conference Series*, volume 215, page 012031. IOP Publishing, 2010.

[113] J. Kitagawa. Possible phase transition and band gap closing in photoexcited semiconductor $\mathrm{cezn_3p_3}$. *Journal of the Physical Society of Japan*, 82(12):125001, 2013.

[114] J. Kitagawa, D. Kitajima, and H. Shimokawa, K.and Takaki. Photoinduced Kondo effect in $\mathrm{CeZn}_3\mathrm{P}_3$. *Physical Review B*, 93(3):035122, 2016.

[115] M. T. Hutchings. Point-charge calculations of energy levels of magnetic ions in crystalline electric fields. In *Solid state physics*, volume 16, pages 227–273. Elsevier, 1964.

[116] A. C. Hewson. *The Kondo problem to heavy fermions*. Number 2. Cambridge university press, 1997.

[117] Z. Wang, K. Barros, G.-W. Chern, D. L. Maslov, and C. D. Batista. Resistivity minimum in highly frustrated itinerant magnets. *Physical review letters*, 117(20):206601, 2016.

[118] H. Takatsu, H. Yoshizawa, S. Yonezawa, and Y. Maeno. Critical behavior of the metallic triangular-lattice Heisenberg antiferromagnet $PdCrO_2$. *Physical Review B*, 79(10):104424, 2009.

[119] J. S. White, C. Niedermayer, G. Gasparovic, C. Broholm, J. M. S. Park, A. Y. Shapiro, L. A. Demianets, and M. Kenzelmann. Multiferroicity in the generic easy-plane triangular lattice antiferromagnet $RbFe(MoO_4)_2$. *Physical Review B*, 88(6):060409, 2013.

[120] S. E. Korshunov. Phase diagram of the antiferromagnetic XY model with a triangular lattice in an external magnetic field. *Journal of Physics C: Solid State Physics*, 19(29):5927, 1986.

[121] E. H. Boubcheur, D. Loison, and H. T. Diep. Phase diagram of XY antiferromagnetic stacked triangular lattices. *Physical Review B*, 54(6):4165, 1996.

[122] N. A. Fortune, S. T. Hannahs, Y. Yoshida, T. E. Sherline, T. Ono, H. Tanaka, and Y. Takano. Cascade of magnetic-field-induced quantum phase transitions in a spin-1 2 triangular-lattice antiferromagnet. *Physical review letters*, 102(25):257201, 2009.

[123] E. Ohmichi, Y. Yoshida, S. I. Ikeda, N. V. Mushunikov, T. Goto, and T. Osada. Double metamagnetic transition in the bilayer ruthenate $Sr_3Ru_2O_7$. *Physical Review B*, 67(2):024432, 2003.

[124] T. Matsumura, T. Inami, M. Kosaka, Y. Kato, T. Inukai, A. Ochiai, H. Nakao, Y. Murakami, S. Katano, and H. S. Suzuki. Structural phase transition in the spin gap system $YbAl_3C_3$. *Journal of the Physical Society of Japan*, 77(10):103601–103601, 2008.

[125] E. Parker and L. Balents. Finite-temperature behavior of a classical spin-orbit-coupled model for $YbMgGaO_4$ with and without bond disorder. *Physical Review B*, 97(18):184413, 2018.

[126] I. Kimchi, A. Nahum, and T. Senthil. Valence bonds in random quantum magnets: theory and application to $YbMgGaO_4$. *Physical Review X*, 8(3):031028, 2018.

[127] B. Chafik El Idrissi, G. Venturini, and B. Malaman. Crystal structures of $R Fe_6 Sn_6$ (R = Sc, Y, Gd = Tm, Lu) rare-earth iron stannides. *Materials Research Bulletin*, 26(12):1331–1338, 1991.

[128] G. Venturini, B. Chafik El Idrissi, and B. Malaman. Magnetic properties of $R Mn_6 Sn_6$ (R = Sc, Y, Gd−Tm, Lu) compounds with $HfFe_6Ge_6$ type structure. *Journal of magnetism and magnetic materials*, 94(1-2):35–42, 1991.

[129] G. Venturini, R. Welter, and B. Malaman. Crystallographic data and magnetic properties of $R T_6 Ge_6$ compounds (R = Sc, Y, Nd, Sm, Gd−Lu; T = Mn, Fe). *Journal of alloys and compounds*, 185(1):99–107, 1992.

[130] J. H. V. J. Brabers, V. H. M. Duijn, F. R. De Boer, and K. H. J. Buschow. Magnetic properties of rare-earth manganese compounds of the $R Mn_6 Ge_6$ type. *Journal of alloys and compounds*, 198(1-2):127–132, 1993.

[131] J. H. V. J. Brabers, K. H. J. Buschow, and F. R. De Boer. Magnetic properties of $R\mathrm{Cr}_6\mathrm{Ge}_6$ compounds. *Journal of alloys and compounds*, 205(1-2):77–80, 1994.

[132] J. M. Cadogan and D. H. Ryan. Independent magnetic ordering of the rare-earth (R) and Fe sublattices in the $R\mathrm{Fe}_6\mathrm{Ge}_6$ and $R\mathrm{Fe}_6\mathrm{Sn}_6$ series. *Journal of alloys and compounds*, 326(1-2):166–173, 2001.

[133] G. Venturini. Filling the CoSn host-cell: the $\mathrm{HfFe}_6\mathrm{Ge}_6$-type and the related structures. *Zeitschrift für Kristallographie-Crystalline Materials*, 221(5-7):511–520, 2006.

[134] G. Venturini, H. Ihou-Mouko, C. Lefevre, S. Lidin, B. Malaman, T. Mazet, J. Tobola, and A. Verniere. Structures and crystal chemistry of MT_6X_6 phases, filled derivatives of the CoSn-B35 structure. *Chemistry of metals and alloys*, (1,№ 1):24–33, 2008.

[135] A. Weiland, L. J. Eddy, G. T. McCandless, H. Hodovanets, J. Paglione, and J. Y. Chan. Refine Intervention: Characterizing Disordered $\mathrm{Yb}_0.5\mathrm{Co}_3\mathrm{Ge}_3$. *Crystal Growth & Design*, 20(10):6715–6721, 2020.

[136] K. H. J. Buschow. Intermetallic compounds of rare-earth and 3d transition metals. *Reports on Progress in Physics*, 40(10):1179, 1977.

[137] B. Malaman, G. Venturini, R. Welter, J. P. Sanchez, P. Vulliet, and E. Ressouche. Magnetic properties of $R\mathrm{Mn}_6\mathrm{Sn}_6$ (R= Gd−Er) compounds from neutron diffraction and Mössbauer measurements. *Journal of magnetism and magnetic materials*, 202(2-3):519–534, 1999.

[138] F. M. Mulder, R. C. Thiel, J. H. V. J. Brabers, F. R. De Boer, and K. H. J. Buschow. 155Gd Mössbauer effect and magnetic properties of $\mathrm{GdMn}_{6-x}\mathrm{Cr}_x\mathrm{Ge}_6$. *Journal of alloys and compounds*, 198(1-2):L1–L3, 1993.

[139] P. Schobinger-Papamantellos, J. Rodrıguez-Carvajal, and K. H. J. Buschow. Magnetic order in the $\mathrm{tbco}_6\mathrm{ge}_6$ and $\mathrm{tbco}_2\mathrm{ge}_2$ compounds: A neutron study. *Journal of alloys and compounds*, 274(1-2):83–89, 1998.

[140] A. Szytuła, E. Wawrzyńska, and A. Zygmunt. Crystal structure and magnetic properties of GdCo_6X_6 (X = Ge, Sn) and $\mathrm{TbCo}_6\mathrm{Ge}_6$. *Journal of alloys and compounds*, 366(1-2):L16–L18, 2004.

[141] L. Ye, M. Kang, J. Liu, F. Von Cube, C. R. Wicker, T. Suzuki, C. Jozwiak, A. Bostwick, E. Rotenberg, D. C. Bell, et al. Massive dirac fermions in a ferromagnetic kagome metal. *Nature*, 555(7698):638–642, 2018.

[142] Q. Wang, Y. Xu, R. Lou, Z. Liu, M. Li, Y. Huang, D. Shen, H. Weng, S. Wang, and H. Lei. Large intrinsic anomalous Hall effect in half-metallic ferromagnet $\mathrm{Co}_3\mathrm{Sn}_2\mathrm{S}_2$ with magnetic Weyl fermions. *Nature communications*, 9(1):3681, 2018.

[143] J.-X. Yin, W. Ma, T. A. Cochran, X. Xu, S. S. Zhang, H.-J. Tien, N. Shumiya, G. Cheng, K. Jiang, B. Lian, et al. Quantum-limit Chern topological magnetism in $\mathrm{TbMn}_6\mathrm{Sn}_6$. *Nature*, 583(7817):533–536, 2020.

[144] Y. Ishii, H. Harima, Y. Okamoto, and Z. Yamaura, J.-I.and Hiroi. $\mathrm{YCr}_6\mathrm{Ge}_6$ as a candidate compound for a kagome metal. *Journal of the Physical Society of Japan*, 82(2):023705, 2013.

[145] N. J. Ghimire, R. L. Dally, L. Poudel, D. C. Jones, D. Michel, N. T. Magar, M. Bleuel, M. A. McGuire, J. S. Jiang, J. F. Mitchell, et al. Competing magnetic phases and fluctuation-driven scalar spin chirality in the kagome metal YMn_6Sn_6. *Science Advances*, 6(51):eabe2680, 2020.

[146] W. Ma, X. Xu, J.-X. Yin, H. Yang, H. Zhou, Z.-J. Cheng, Y. Huang, Z. Qu, F. Wang, M. Z. Hasan, et al. Rare Earth Engineering in RMn_6Sn_6 (R = Gd−Tm, Lu) Topological Kagome Magnets. *Physical review letters*, 126(24):246602, 2021.

[147] S. Peng, Y. Han, G. Pokharel, J. Shen, Z. Li, M. Hashimoto, D. Lu, B. R. Ortiz, Y. Luo, H. Li, et al. Realizing Kagome Band Structure in Two-Dimensional Kagome Surface States of RV_6Sn_6 (R = Gd, Ho). *Physical review letters*, 127(26):266401, 2021.

[148] H. Ishikawa, T. Yajima, M. Kawamura, H. Mitamura, and K. Kindo. GdV_6Sn_6: A Multi-carrier Metal with Non-magnetic 3d-electron Kagome Bands and 4f-electron Magnetism. *Journal of the Physical Society of Japan*, 90(12):124704, 2021.

[149] G. Pokharel, S. M. L. Teicher, B. R. Ortiz, P. M. Sarte, G. Wu, S. Peng, J. He, R. Seshadri, and S. D. Wilson. Electronic properties of the topological kagome metals YV_6Sn_6 and GdV_6 Sn_6. *Physical Review B*, 104(23):235139, 2021.

[150] L. Romaka, Y. Stadnyk, V. V. Romaka, P. Demchenko, M. Stadnyshyn, and M. Konyk. Peculiarities of component interaction in {Gd, Er}–V–Sn Ternary systems at 870 K and crystal structure of RV_6Sn_6 stannides. *Journal of alloys and compounds*, 509(36):8862–8869, 2011.

[151] B. H. Toby and Robert B. Von D. GSAS-II: the genesis of a modern open-source all purpose crystallography software package. *Journal of Applied Crystallography*, 46(2):544–549, 2013.

[152] B. A. Hatt, J. K. R. Page, and V. G. Rivlin. The structure and superconducting transitions of some pseudobinary 'β-W'alloys. *Journal of Low Temperature Physics*, 10:285–298, 1973.

[153] M. Tian, J. Wang, J. Snyder, J. Kurtz, Y. Liu, P. Schiffer, T. E. Mallouk, and M. H. W. Chan. Synthesis and characterization of superconducting single-crystal Sn nanowires. *Applied Physics Letters*, 83(8):1620–1622, 2003.

[154] A. S. Sefat, S. L. Bud'ko, and P. C. Canfield. Magnetization, resistivity and heat capacity of the anisotropic $RVSb_3$ crystals (R = La−Nd, Sm, Gd−Dy). *Journal of magnetism and magnetic materials*, 320(3-4):120–141, 2008.

[155] K. D. Myers, S. L. Bud'ko, I. R. Fisher, Z. Islam, H. Kleinke, A. H. Lacerda, and P. C. Canfield. Systematic study of anisotropic transport and magnetic properties of $RAgSb_2$ (R = Y, La−Nd, Sm, Gd−Tm). *Journal of magnetism and magnetic materials*, 205(1):27–52, 1999.

[156] S. L. Bud'ko, Z. Islam, T. A. Wiener, I. R. Fisher, A. H. Lacerda, and P. C. Canfield. Anisotropy and metamagnetism in the RNi_2Ge_2 (R = Y, La−Nd, Sm−Lu) series. *Journal of magnetism and magnetic materials*, 205(1):53–78, 1999.

[157] M. Reehuis, A. Krimmel, N. Büttgen, A. Loidl, and A. Prokofiev. Crystallographic and magnetic structure of ZnVO: Structural phase transition due to spin-driven Jahn-Teller distortions. *The European Physical Journal B-Condensed Matter and Complex Systems*, 35(3):311–316, 2003.

[158] H. Kadowaki, K. Ubukoshi, K. Hirakawa, J. L. Martínez, and G. Shirane. Experimental study of new type phase transition in triangular lattice antiferromagnet VCl_2. *Journal of the Physical Society of Japan*, 56(11):4027–4039, 1987.

[159] W. H. Blades, Ar. C. Reber, S. N. Khanna, L. López-Sosa, P. Calaminici, and A. M. Köster. Evolution of the Spin Magnetic Moments and Atomic Valence of Vanadium in $VCu^x{}_+$, $VAg^x{}_+$, and $VAu^x{}_+$ Clusters ($x = 3-14$). *The Journal Of Physical Chemistry A*, 121(15):2990–2999, 2017.

[160] D. R. Noakes and G. K. Shenoy. The effect of a crystalline electric field on the magnetic transition temperatures of rare-earth rhodium borides. *Physics Letters A*, 91(1):35–36, 1982.

[161] E. Morosan, S. L. Bud'ko, and P. C. Canfield. Magnetic ordering and effects of crystal electric field anisotropy in the hexagonal compounds RPtIn (R = Y, Gd−Lu). *Physical Review B*, 72(1):014425, 2005.

[162] M. Falkowski, B. Andrzejewski, and A. Kowalczyk. Magnetic properties of hexagonal RNi$_4$Si (R = rare earth) compounds. *Journal of alloys and compounds*, 442(1-2):155–157, 2007.

[163] A. Szytuła, S. Baran, Ł Gondek, A. Arulraj, B. Penc, and N. Stüsser. Magnetic Properties of Hexagonal RTIn Rare-Earth Intermetallics with Frustration. *Acta Physica Polonica A*, 117(4):590–594, 2010.

[164] A. Marcinkova, C. de la Cruz, J. Yip, L. L. Zhao, J. K. Wang, E. Svanidze, and E. Morosan. Strong magnetic coupling in the hexagonal R_5Pb_3 compounds (R = Gd−Tm). *Journal of Magnetism and Magnetic Materials*, 384:192–203, 2015.

[165] N. Van H., T. Takeuchi, H. Shishido, C. Tonohiro, T. Yamada, H. Nakashima, K. Sugiyama, R. Settai, T. D. Matsuda, Y. Haga, et al. Magnetic properties and crystalline electric field scheme in RRhIn5 (R: Rare Earth). *Journal of the Physical Society of Japan*, 76(6):064702–064702, 2007.

[166] P. Boutron. Exact calculation of the paramagnetic susceptibility of a single crystal with arbitrary crystal field and exchange interactions. *Physical Review B*, 7(7):3226, 1973.

[167] H. Zhou, S. E. Lambert, M. B. Maple, and B. D. Dunlap. Magnetic anisotropy and crystalline electric field effects in RRh$_4$B$_4$ single crystals. *Philosophical Magazine*, 89(22-24):1861–1879, 2009.

[168] T. Kurumaji, T. Nakajima, M. Hirschberger, A. Kikkawa, Y. Yamasaki, H. Sagayama, H. Nakao, Y. Taguchi, T.-H. Arima, and Y. Tokura. Skyrmion lattice with a giant topological Hall effect in a frustrated triangular-lattice magnet. *Science*, 365(6456):914–918, 2019.

[169] H. Zhang, Q. Huang, L. Hao, J. Yang, K. Noordhoek, S. Pandey, H. Zhou, and J. Liu. Anomalous magnetoresistance in centrosymmetric skyrmion-lattice magnet Gd_2PdSi_3. *New Journal of Physics*, 22(8):083056, 2020.

[170] L. A. Fenner, A. A. Dee, and A. S. Wills. Non-collinearity and spin frustration in the itinerant kagome ferromagnet fe_3sn_2. *Journal of Physics: Condensed Matter*, 21(45):452202, 2009.

[171] T. Kida, L. A. Fenner, A. A. Dee, I. Terasaki, M. Hagiwara, and A. S. Wills. The giant anomalous Hall effect in the ferromagnet Fe_3Sn_2—a frustrated kagome metal. *Journal of Physics: Condensed Matter*, 23(11):112205, 2011.

[172] H. Li, B. Ding, J. Chen, Z. Li, Z. Hou, E. Liu, H. Zhang, X. Xi, G. Wu, and W. Wang. Large topological Hall effect in a geometrically frustrated kagome magnet Fe_3Sn_2. *Applied Physics Letters*, 114(19):192408, 2019.

[173] M. Kang, L. Ye, S. Fang, J.-S. You, A. Levitan, M. Han, J. I. Facio, C. Jozwiak, A. Bostwick, E. Rotenberg, et al. Dirac fermions and flat bands in the ideal kagome metal fesn. *Nature materials*, 19(2):163–169, 2020.

[174] B. R. Ortiz, S. M. L. Teicher, Y. Hu, J. L. Zuo, P. M. Sarte, E. C. Schueller, A. M. Milinda Abeykoon, M. J. Krogstad, S. Rosenkranz, R. Osborn, et al. CsV_3Sb_5: A $*mathbbZ_2* topological kagome metal with a superconducting ground state. *Physical Review Letters*, 125(24):247002, 2020.

[175] B. R. Ortiz, P. M. Sarte, E. M. Kenney, M. J. Graf, S. M. L. Teicher, R. Seshadri, and S. D. Wilson. Superconductivity in the $*mathbbZ_2* kagome metal KV_3Sb_5. *Physical Review Materials*, 5(3):034801, 2021.

[176] Q. Yin, Z. Tu, C. Gong, Y. Fu, S. Yan, and H. Lei. Superconductivity and normal-state properties of kagome metal RbV_3Sb_5 single crystals. *Chinese Physics Letters*, 38(3):037403, 2021.

[177] H. W. S. Arachchige, W. R. Meier, M. Marshall, T. Matsuoka, R. Xue, M. A. McGuire, R. P. Hermann, H. Cao, and D. Mandrus. Charge Density Wave in Kagome Lattice Intermetallic ScV_6Sn_6. *Physical Review Letters*, 129(21):216402, 2022.

[178] F. Tappe, C. Schwickert, and R. Pöttgen. Ternary ordered Laves phases $RE$$Ni_4Cd$. *Intermetallics*, 24:33–37, 2012.

[179] S. Linsinger, M. Eul, C. Schwickert, R. Decourt, B. Chevalier, U. C. Rodewald, J.-L. Bobet, and R. Pöttgen. Structure, homogeneity ranges, magnetic, and electrical properties of the ordered Laves phases $RE$$Ni_4Mg$ with $MgCu_4Sn$ type structure. *Intermetallics*, 19(10):1579–1585, 2011.

[180] S. Stein, L. Heletta, T. Block, and R. Pöttgen. Rare earth-copper-magnesium intermetallics: crystal structure of CeCuMg, magnetocaloric effect of GdCuMg and physical properties of the Laves phases $RE$$Cu_4Mg$ (RE = Sm, Gd, Tb, Tm). *Zeitschrift für Naturforschung B*, 73(12):987–997, 2018.

[181] S. Abe, H. Nakazawa, T. Kaneko, H. Yoshida, K. Kamigaki, Y. Nakagawa, and S. Miura. Magnetic Properties of Cubic Intermetallic Compounds RCu$_4$Pd (R = Gd, Tb, Dy, Ho and Er). *Journal of the Physical Society of Japan*, 58(9):3328–3333, 1989.

[182] T. Takeshita, S. K. Malik, A. A. El-Atttar, and W. E. Wallace. Crystal Structure and Magnetic Properties of RCu$_4$Ag (R = Rare Earth) Intermetallic Compounds. In *AIP Conference Proceedings*, volume 34, pages 230–232. American Institute of Physics, 1976.

[183] T. Kaneko, S. Arai, S. Abe, and K. Kamigaki. Magnetic Properties of Cubic RAuCu$_4$ (R = Gd, Tb, Dy, Ho and Er) Intermetallic Compounds. *Journal of the Physical Society of Japan*, 55(12):4441–4447, 1986.

[184] V. Fritsch, J. D. Thompson, and J. L. Sarrao. Spin and orbital frustration in RInCu$_4$ (R = Gd, Dy, Ho, and Er). *Physical Review B*, 71(13):132401, 2005.

[185] S. G. Mercena, E. C. Mendonça, C. T. Meneses, L. S. Silva, J. G. S. Duque, C. B. R. Jesus, J. C. Souza, and P. G. Pagliuso. Complex magnetic behavior along the GdIn(Ni$_x$Cu$_{1-x}$)$_4$($0.00 \leq x \leq 1.00$) series of compounds. *Journal of Applied Physics*, 125(6):063903, 2019.

[186] J. Lee, H. Park, N. R. Lee-Hone, D. M. Broun, and E. Mun. Thermodynamic and transport properties of YbNi$_4$Cd. *Physical Review B*, 97(19):195144, 2018.

[187] K. Kadir, D. Noreus, and I. Yamashita. Structural determination of AMgNi$_4$ (where A = Ca, La, Ce, Pr, Nd and Y) in the AuBe$_5$ type structure. *Journal of Alloys and Compounds*, 345(1-2):140–143, 2002.

[188] M. Bouvier, P. Lethuillier, and D. Schmitt. Specific heat in some gadolinium compounds. i. experimental. *Physical Review B*, 43(16):13137, 1991.

[189] J. S. Smart. *Effective field theories of magnetism*. Number 2. Saunders, 1966.

[190] S. Mugiraneza and A. M. Hallas. Tutorial: a beginner's guide to interpreting magnetic susceptibility data with the curie-weiss law. *Communications Physics*, 5(1):95, 2022.

[191] M. D. Koterlin, B. S. Morokhivskii, I. D. Shcherba, and Y. M. Kalychak. Transport and magnetic properties of the compounds YbNi$_4$In and YbNiIn$_4$ with valence-unstable Yb. *Physics of the Solid State*, 41:1759–1762, 1999.

[192] S. Abe, H. Nakazawa, T. Kaneko, H. Yoshida, and K. Kamigaki. Magnetic and electric properties of intermetallic compounds RCu$_4$Pd (R = Gd, Tb, Dy, Ho and Er). *Le Journal de Physique Colloques*, 49(C8):C8–385, 1988.

[193] T. Tayama, Y. Takayama, Y. Miura, S. Zhang, and Y. Isikawa. Low-temperature magnetization of antiferromagnet NdCu$_4$Ag. *Journal of the Physical Society of Japan*, 80(Suppl. A):SA074, 2011.

[194] A. K. Bashir, M. B. T. Tchokonté, D. Britz, B. M. Sondezi, and A. M. Strydom. Magnetic and thermodynamic properties of GdCu$_4$Au. In *Journal of Physics: Conference Series*, volume 592, page 012050. IOP Publishing, 2015.

[195] H. Nakamura, A. Uenishi, K. Ito, M. Shiga, T. Kuwai, and J. Sakurai. Transport properties of $R\mathrm{InCu}_4$ with C15b-type structure. *Journal of magnetism and magnetic materials*, 140:923–924, 1995.

[196] P. G. Pagliuso, C. Rettori, S. B. Oseroff, J. Sarrao, Z. Fisk, A. Cornelius, and M. F. Hundley. ESR of Gd^{3+} in LuInCu_4 intermetallic compound. *Solid state communications*, 104(4):223–226, 1997.

[197] J. Sakurai, Y. Kubo, T. Kondo, J. Pierre, and E. F. Bertaut. Relations between the ruderman-kittel-kasuya-yosida interaction electron concentration and crystal structure. *Journal of Physics and Chemistry of Solids*, 34(8):1305–1316, 1973.

[198] S. Abe, Y. Atsumi, T. Kaneko, and H. Yoshida. Magnetic properties of $R\mathrm{Cu}_4\mathrm{In}$ (R = Gd-Er) intermetallic compounds. *Journal of Magnetism and Magnetic Materials*, 104:1397–1398, 1992.

[199] P. Monachesi and A. Continenza. Electronic and volumetric effects in ternary compounds of ytterbium. *Physical Review B*, 54(19):13558, 1996.

[200] T. R. McGuire, R. J. Gambino, S. J. Pickart, and H. A. Alperin. Magnetic structure and exchange interactions in cubic gadolinium compounds. *Journal of Applied Physics*, 40(3):1009–1010, 1969.

[201] D. X. Li, Y. Haga, H. Shida, T. Suzuki, Y. S. Kwon, and G. Kido. Magnetic properties of stoichiometric gd monopnictides. *Journal of Physics: Condensed Matter*, 9(48):10777, 1997.

[202] C.-G. Duan, R. F. Sabiryanov, W.-N. Mei, P. A. Dowben, S. S. Jaswal, and E. Y. Tsymbal. Magnetic ordering in gd monopnictides: Indirect exchange versus superexchange interaction. *Applied physics letters*, 88(18):182505, 2006.

[203] T. Kasuya and D. X. Li. Mechanism of strong ferromagnetism in gdn. *Journal of magnetism and magnetic materials*, 167(1-2):L1–L6, 1997.

[204] H. Anzai, S. Ishihara, H. Shiono, K. Morikawa, T. Iwazumi, H. Sato, T. Zhuang, K. T. Matsumoto, and K. Hiraoka. Mixed-valence state of the rare-earth compounds $\mathrm{Yb}X\mathrm{Cu}_4$ (X = Mg, Cd, In, and Sn): Magnetic susceptibility, x-ray diffraction, and x-ray absorption spectroscopy investigations. *Physical Review B*, 100(24):245124, 2019.

[205] P. G. Pagliuso, C. Rettori, J. L. Sarrao, A. Cornelius, M. F. Hundley, Z. Fisk, and S. B. Oseroff. Electron spin resonance of Gd^{3+} and Nd^{3+} in $\mathrm{LuIn}A_4$ (A = Cu, Ni). *Physical Review B*, 60(19):13515, 1999.

[206] E. Figueroa, J. M. Lawrence, J. L. Sarrao, Z. Fisk, M. F. Hundley, and J. D. Thompson. Hall effect in $\mathrm{Yb}X\mathrm{Cu}_4$ and the role of carrier density in the YbInCu_4 valence transition. *Solid state communications*, 106(6):347–351, 1998.

[207] N.-N. Sun and H.-Y. Wang. The J_1-J_2 model on the face-centered-cubic lattices. *Journal of Magnetism and Magnetic Materials*, 454:176–184, 2018.

[208] M. E. Lines. Antiferromagnetism in the face-centered cubic lattice. i. the random-phase green's function approximation. *Physical Review*, 139(4A):A1304, 1965.

[209] Story, T. and Karczewski, G. and Świerkowski, L. and Gałazka, R. R. Magnetism and band structure of the semimagnetic semiconductor Pb-Sn-Mn-Te. *Physical Review B*, 42(16):10477, 1990.

[210] Swagten, H. J. M. and De Jonge, W. J. M. and Gałazka, R. R. and Warmenbol, P. and Devreese, J. T. Hole density and composition dependence of ferromagnetic ordering in Pb-Sn-Mn-Te. *Physical Review B*, 37(16):9907, 1988.

[211] J. P. Remeika, G. P. Espinosa, A. S. Cooper, H. Barz, J. M. Rowell, D. B. McWhan, J. M. Vandenberg, D. E Moncton, Z. Fisk, L. D. Woolf, et al. A new family of ternary intermetallic superconducting/magnetic stannides. *Solid State Communications*, 34(12):923–926, 1980.

[212] J. L. Hodeau, J. Chenavas, M. Marezio, and J. P. Remeika. The crystal structure of $SnYb_3Rh_4Sn_{12}$, a new ternary superconducting stannide. *Solid State Communications*, 36(10):839–845, 1980.

[213] B. K. Rai, I. W. H. Oswald, J. K. Wang, G. T. McCandless, J. Y. Chan, and E. Morosan. Superconductivity in Single Crystals of $Lu_3T_4Ge_{13-x}$ (T= Co, Rh, Os) and $Y_3T_4Ge_{13-x}$ (T = Ir, Rh, Os). *Chemistry of Materials*, 27(7):2488–2494, 2015.

[214] M. F. Hundley, J. L. Sarrao, J. D. Thompson, R. Movshovich, M. Jaime, C. Petrovic, and Z. Fisk. Unusual Kondo behavior in the indium-rich heavy-fermion antiferromagnet $Ce_3Pt_4In_{13}$. *Physical Review B*, 65(2):024401, 2001.

[215] C. S. Lue, H. F. Liu, S-.L Hsu, M. W. Chu, H. Y. Liao, and Y. K Kuo. Observation of a possible charge-density-wave transition in cubic $Ce_3Co_4Sn_{13}$. *Physical Review B*, 85(20):205120, 2012.

[216] L. E. Klintberg, S. K Goh, P. L. Alireza, P. J. Saines, D. A. Tompsett, P. W. Logg, J. Yang, B. Chen, K. Yoshimura, and F. M. Grosche. Pressure-and composition-induced structural quantum phase transition in the cubic superconductor (Sr, Ca)$_3$$Ir_4Sn_{13}$. *Physical Review Letters*, 109(23):237008, 2012.

[217] U. Köhler, A. P. Pikul, N. Oeschler, T. Westerkamp, A. M. Strydom, and F. Steglich. Low-temperature study of the strongly correlated compound $Ce_3Rh_4Sn_{13}$. *Journal of Physics: Condensed Matter*, 19(38):386207, 2007.

[218] R. Gumeniuk. Structural and physical properties of remeika phases. In *Handbook on the Physics and Chemistry of Rare Earths*, volume 54, pages 43–143. Elsevier, 2018.

[219] B. Eisenmann and H. Schäfer. Käfigstrukturen in intermetallischen verbindungen: zur kenntnis von $LaRuSn_3$, $CeRuSn_3$, $PrRuSn_3$ und $NdRuSn_3$. *Journal of the Less Common Metals*, 123(1-2):89–94, 1986.

[220] M. Schreyer and T. F. Fässler. $Ca_7Co_8Sn_{25}$–$Ca_3Co_4Sn_{13}$ revised. *Solid State Sciences*, 8(7):793–797, 2006.

[221] Y. V. Galadzhun and R. Pöttgen. Platinum-Indium Polyanions in the Structures of $LaPtIn_4$ and $Ln$$PtIn_3$ (Ln = La, Ce, Pr, Nd, Sm) and Structure Refinement of Ce_2Pt_2In. *Zeitschrift für anorganische und allgemeine Chemie*, 625(3):481–487, 1999.

[222] K. Ghosh, S. Ramakrishnan, S. K. Dhar, S. K. Malik, G. Chandra, V. K. Pecharsky, K. A. Gschneidner Jr, Z. Hu, and W. B. Yelon. Crystal structures and low-temperature behaviors of the heavy-fermion compounds $CeRuGe_3$ and $Ce_3Ru_4Ge_{13}$ containing both trivalent and tetravalent cerium. *Physical Review B*, 52(10):7267, 1995.

[223] V. K. Anand, D. T. Adroja, A. D. Hillier, W. Kockelmann, A. Fraile, and A. M. Strydom. Complex magnetic behavior in the novel Kondo lattice compound $CeRhSn_3$. *Journal of Physics: Condensed Matter*, 23(27):276001, 2011.

[224] K. Suyama, K. Iwasa, Y. Otomo, K. Tomiyasu, H. Sagayama, R. Sagayama, H. Nakao, R. Kumai, Y. Kitajima, F. Damay, et al. Chiral-crystal-structure transformations and magnetic states of $R_3Rh_4Sn_{13}$ (R = La and Ce). *Physical Review B*, 97(23):235138, 2018.

[225] M. Gamża, W. Schnelle, A. Ślebarski, U. Burkhardt, R. Gumeniuk, and H. Rosner. Electronic structure and thermodynamic properties of $Ce_3Rh_4Sn_{13}$ and La3Rh4Sn_{13}. *Journal of Physics: Condensed Matter*, 20(39):395208, 2008.

[226] A. Ślebarski, B. D. White, M. Fijałkowski, J. Goraus, J. J. Hamlin, and M. B. Maple. Electronic, magnetic, and electric transport properties of $Ce_3Rh_4Sn_{13}$ and $Ce_3Co_4Sn_{13}$: A comparative study. *Physical Review B*, 86(20):205113, 2012.

[227] A. Ślebarski, M. Fijałkowski, J. Goraus, L. Kalinowski, and P. Witas. Crystal electric field and the ground state properties of heavy fermion $Ce_3Ru_4Sn_{13}$. *Journal of Alloys and Compounds*, 615:921–928, 2014.

[228] T. Fukuhara, I. Sakamoto, H. Sato, S. Takayanagi, and N. Wada. Electronic and magnetic properties of a new heavy-fermion compound, $CeRuSn_3$. *Journal of Physics: Condensed Matter*, 1(40):7487, 1989.

[229] S. Takayanagi, T. Fukuhara, H. Sato, N. Wada, and Y. Yamada. Heavy fermion behaviour in $CeRuSn_3$ compound. *Physica B: Condensed Matter*, 165:447–448, 1990.

[230] V. K. Anand, D. T. Adroja, A. Bhattacharyya, A. D. Hillier, D. Britz, A. M. Strydom, J. W. Taylor, A. Fraile, and W. Kockelman. Neutron scattering and μSR studies on a Kondo lattice heavy fermion $CeRuSn_3$. 592(1):012008, 2015.

[231] V. K. Anand, D. T. Adroja, D. Britz, A. M. Strydom, J. W. Taylor, and W. Kockelmann. Crystal-field states of Kondo lattice heavy fermions $CeRuSn_3$ and $CeRhSn_3$. *Physical Review B*, 94(1):014440, 2016.

[232] Rodríguez-Carvajal, J. Recent advances in magnetic structure determination by neutron powder diffraction. *Physica B: Condensed Matter*, 192(1-2):55–69, 1993.

[233] C. L. Yang, X. Wang, X. Zhang, D. S. Wu, M. Liu, P. Zheng, J. Y. Yao, Z. Z. Li, Y.-F. Yang, Y. G. Shi, et al. Kondo effect in the quasiskutterudite $Yb_3Os_4Ge_13$. *Physical Review B*, 91(7):075120, 2015.

[234] T. Mishra, C. Schwickert, T. Langer, R. Pöttgen, et al. Ternary Stannides $RE_3Ru_4Sn_{13}$ (RE = La, Ce, Pr, Nd)–Structure, Magnetic Properties, and 119Sn Mössbauer Spectroscopy. *Zeitschrift für Naturforschung B*, 66(7):664–670, 2011.

[235] G. P. Espinosa, A. S. Cooper, H. Barz, and J. P. Remeika. Crystal chemistry, growth and reentrant behavior of additional superconducting/magnetic stannides. *Materials Research Bulletin*, 15(11):1635–1641, 1980.

[236] A. Ślebarski and J. Goraus. Electronic structure and crystallographic properties of skutterudite-related $Ce_3M_4Sn_{13}$ and $La_3M_4Sn_{13}$ (M = Co, Ru, and Rh). *Physical Review B*, 88(15):155122, 2013.

[237] T. Fukuhara, S. Iwakawa, and H. Sato. Transport and magnetic properties of a new valence fluctuating compound $SmRuSn_3$. *Journal of Magnetism and Magnetic Materials*, 104:667–668, 1992.

[238] T. Fukuhara, I. Sakamoto, and H. Sato. Transport and magnetic properties of rerusn$_3$ (re= la, ce, pr, nd, sm): a heavy fermion compound cerusn$_3$ and a new valence fluctuating compound smrusn$_3$. *Journal of Physics: Condensed Matter*, 3(45):8917, 1991.

[239] T. Fukuhara, I. Sakamoto, and H. Sato. Critical magnetic behaviors in CeRuSnx ($2.85 \leq x \leq 3.15$). *Physica B: Condensed Matter*, 165:443–444, 1990.

[240] O. Prakash, A. Thamizhavel, and S. Ramakrishnan. Ferromagnetic ordering of minority Ce^{3+} spins in a quasi-skutterudite $Ce_3Os_4Ge_{13}$ single crystal. *Physical Review B*, 93(6):064427, 2016.

[241] A. M. Hallas, C. L. Huang, B. K. Rai, A. Weiland, G. T McCandless, J. Y. Chan, J. Beare, G. M. Luke, and E. Morosan. Complex transport and magnetism in inhomogeneous mixed valence $Ce_3Ir_4Ge_{13}$. *Physical Review Materials*, 3(11):114407, 2019.

[242] H. Ishii, T. Hanyu, T. Fukuhara, I. Sakamoto, H. Sato, and S. Yamaguchi. Valence States of Rare-Earth Ions in RERuSn$_3$ (RE = La, Ce, Pr, Nd, Sm) and Related Compounds Studied by Core-Level Photoemission Spectroscopy. *Journal of the Physical Society of Japan*, 62(2):811–817, 1993.

[243] V. T. Rajan. Magnetic susceptibility and specific heat of the Coqblin-Schrieffer model. *Physical Review Letters*, 51(4):308, 1983.

[244] C. Rossel, K. N. Yang, M. B. Maple, Z. Fisk, E. Zirngiebl, and J. D. Thompson. Strong electronic correlations in a new class of Yb-based compounds: YbXCu$_4$ (X = Ag, Au, Pd). *Physical Review B*, 35(4):1914, 1987.

[245] N. O. Moreno, A. Lobos, A. A. Aligia, E. D. Bauer, S. Bobev, V. Fritsch, J. L. Sarrao, P. G. Pagliuso, J. D. Thompson, C. D. Batista, et al. Crystal-field effects in the mixed-valence compounds $Yb_2M_3Ga_9$ (M = Rh, Ir). *Physical Review B*, 71(16):165107, 2005.

[246] H. Yamamoto, M. Ishikawa, K. Hasegawa, and J. Sakurai. $CeFeGe_3$: A concentrated Kondo compound with a stable valency and high Kondo temperature. *Physical Review B*, 52(14):10136, 1995.

[247] M. Kratochvílová, J. Prokleška, K. Uhlířová, V. Tkáč, M. Dušek, V. Sechovskỳ, and J. Custers. Coexistence of antiferromagnetism and superconductivity in heavy fermion cerium compound Ce_3PdIn_{11}. *Scientific Reports*, 5(1):1–11, 2015.

[248] E. D. Mun, B. K. Lee, Y. S. Kwon, and M. H. Jung. Kondo ground state of $CeCoGe_2$ with $j = \frac{5}{2}$. *Physical Review B*, 69(8):085113, 2004.

[249] M. S. Torikachvili, S. Jia, E. D. Mun, S. T. Hannahs, R. C. Black, W. K. Neils, D. Martien, S. L. BudḰo, and P. C. Canfield. Six closely related YbT_2Zn_{20} (T = Fe, Co, Ru, Rh, Os, Ir) heavy fermion compounds with large local moment degeneracy. *Proceedings of the National Academy of Sciences*, 104(24):9960–9963, 2007.

[250] M. Deppe, S. Hartmann, M. E. Macovei, N. Oeschler, M. Nicklas, and C. Geibel. Investigation of $Yb_2Pt_6Al_{15}$ single crystals: heavy fermion system with a large local moment degeneracy. *New Journal of Physics*, 10(9):093017, 2008.

[251] P. Haen, J. Flouquet, F. Lapierre, P. Lejay, and G. Remenyi. Metamagnetic-like transition in $CeRu_2Si_2$? *Journal of low temperature physics*, 67(5):391–419, 1987.

[252] E. L. Thomas, H.-O. Lee, A. N. Bankston, S. MaQuilon, P. Klavins, M. Moldovan, D. P. Young, Z. Fisk, and J. Y. Chan. Crystal growth, transport, and magnetic properties of $Ln_3Co_4Sn_{13}$ (Ln = La, Ce) with a perovskite-like structure. *Journal of Solid State Chemistry*, 179(6):1642–1649, 2006.

[253] N. Tsujii, H. Kontani, and K. Yoshimura. Universality in heavy fermion systems with general degeneracy. *Physical Review Letters*, 94(5):057201, 2005.

[254] B. Coqblin and J. R. Schrieffer. Exchange interaction in alloys with cerium impurities. *Physical Review*, 185(2):847, 1969.

[255] K. Hanzawa, K. Ohara, and K. Yosida. Magnetization in heavy-fermion compounds. *Journal of the Physical Society of Japan*, 66(10):3001–3004, 1997.

[256] S. R. Saha, H. Sugawara, T. Namiki, Y. Aoki, and H. Sato. Effect of uniaxial pressure on the magnetic anomalies of the heavy-fermion metamagnet $CeRu_2Si_2$. *Physical Review B*, 65(21):214429, 2002.

[257] I. W. H. Oswald, B. K. Rai, G. T. McCandless, E. Morosan, and J. Y. Chan. The proof is in the powder: revealing structural peculiarities in the $Yb_3Rh_4Sn_{13}$ structure type. *CrystEngComm*, 19(25):3381–3391, 2017.

[258] C. N. Kuo, W. T. Chen, C. W. Tseng, C. J. Hsu, R. Y. Huang, F. C. Chou, Y. K. Kuo, and C. S. Lue. Evidence for a second-order phase transition around 350 K in $Ce_3Rh_4Sn_{13}$. *Physical Review B*, 97(9):094101, 2018.

[259] Y. Otomo, K. Iwasa, K. Suyama, K. Tomiyasu, H. Sagayama, R. Sagayama, H. Nakao, R. Kumai, and Y. Murakami. Chiral crystal-structure transformation of $R_3Co_4Sn_{13}$ (R= La and Ce). *Physical Review B*, 94(7):075109, 2016.